PULSE TIMING STUDIES OF X-RAY BINARIES: GX 1+4, SWIFT
J0513.4-6547, X PERSEI AND SXP 1062

A THESIS SUBMITTED TO
THE GRADUATE SCHOOL OF NATURAL AND APPLIED SCIENCES
OF
MIDDLE EAST TECHNICAL UNIVERSITY

BY

MUHAMMED MIRAÇ SERIM

IN PARTIAL FULFILLMENT OF THE REQUIREMENTS
FOR
THE DEGREE OF DOCTOR OF PHILOSOPHY
IN
PHYSICS

JANUARY 2019

Approval of the thesis:

PULSE TIMING STUDIES OF X-RAY BINARIES: GX 1+4, SWIFT J0513.4-6547, X PERSEI AND SXP 1062

submitted by **MUHAMMED MIRAÇ SERIM** in partial fulfillment of the requirements for the degree of **Doctor of Philosophy in Physics Department, Middle East Technical University** by,

Prof. Dr. Halil Kalıpçılar
Dean, Graduate School of **Natural and Applied Sciences** _____

Prof. Dr. Altuğ Özpineci
Head of Department, **Physics** _____

Prof. Dr. Altan Baykal
Supervisor, **Physics, METU** _____

Prof. Dr. Sıtkı Çağdaş İnam
Co-supervisor, **E. and E. Eng. Dept., Başkent University** _____

Examining Committee Members:

Prof. Dr. Sacit Özdemir
Astronomy and Space Sciences Dept., Ankara University _____

Prof. Dr. Altan Baykal
Physics Dept., METU _____

Assoc. Prof. Dr. Serhat Çakır
Physics Dept., METU _____

Assoc. Prof. Dr. Sinan Kaan Yerli
Physics Dept., METU _____

Assoc. Prof. Dr. Mesut Yılmaz
Astronomy and Space Sciences Dept., Ankara University _____

Date:

I hereby declare that all information in this document has been obtained and presented in accordance with academic rules and ethical conduct. I also declare that, as required by these rules and conduct, I have fully cited and referenced all material and results that are not original to this work.

Name, Surname: Muhammed Miraç Serim

Signature   :

ABSTRACT

PULSE TIMING STUDIES OF X-RAY BINARIES: GX 1+4, SWIFT J0513.4-6547, X PERSEI AND SXP 1062

Serim, Muhammed Miraç

Ph.D., Department of Physics

Supervisor : Prof. Dr. Altan Baykal

Co-Supervisor : Prof. Dr. Sıtkı Çağdaş İnam

January 2019, 140 pages

This thesis focuses on X-ray timing properties of four different X-ray binary systems, based on archival data of the X-ray missions RXTE, Swift, XMM-Newton, Chandra and Integral. One of the selected sources is a LMXB system GX 1+4 while remaining sources are BeXB systems: SWIFT J0513.4-6547, X Persei and SXP 1062. For GX 1+4, the timing analysis of RXTE-PCA observations between 2001 March 3 and 2003 January 31 are presented. The timing solutions of two different time intervals are constructed. Futhermore, within the CGRO-BATSE data between 1991 and 1999, an episodic mode-switching of correlation between X-ray flux and frequency derivative is observed. For SWIFT J0513.4-6547, the data of 2009 outburst and the re-brightening in 2014 are investigated with exquisite details. When the source is quiescent between 2009 and 2014, average spin-down rate of the source is measured to be $\sim 1.52 \times 10^{-12}$ Hz/s indicating a surface dipole magnetic field of $\sim 1.5 \times 10^{13}$ G. X Persei is examined using RXTE and Integral observations between 1998 and 2010. For X Persei, the result on the dependence of frequency derivative on X-ray flux hints that wind accretion is also possible. From the noise spectrum, a red noise component

with an index of ~ -1 is observed with an excessive noise component dominating the disc accretion flow on long time-scales. In the case of SXP 1062, the pulsar's rotation is observed to slow down with a steady rate $-4.29(7) \times 10^{-14}$ Hz/s from which the magnetic field is inferred to be $\sim 1.5 \times 10^{14}$ G. Furthermore, precise pulse timing study of the object reveals a glitch event with an amplitude of $\Delta\nu = 1.28(5) \times 10^{-6}$ Hz which is an extraordinary event for an accreting pulsar. Although the glitch events are conventionally observed in isolated pulsars, the discovery of a glitch in SXP 1062 ensures that glitch events are also possible for accreting pulsars.

ÖZ

GX 1+4, SWIFT J0513.4-6547, X PERSEİ VE SXP 1062 X-IŞINI ÇİFTLERİNİN ATIM ZAMANLAMASI ANALİZLERİ

Serim, Muhammed Miraç

Doktora, Fizik Bölümü

Tez Yöneticisi : Prof. Dr. Altan Baykal

Ortak Tez Yöneticisi : Prof. Dr. Sıtkı Çağdaş İnam

Ocak 2019 , 140 sayfa

Bu tez RXTE, Swift, XMM-Newton, Chandra ve Integral uydularının arşiv verilerine dayanarak, dört farklı X-ışını çiftinin zamanlama analizlerine odaklanmıştır. Seçilen kaynaklardan biri, GX 1+4, LMXB tipi olup, kalan üç tanesi, SWIFT J0513.4-6547, X Persei ve SXP 1062; BeXB tipi sistemleridir. GX 1+4 kaynağı için, 3 Mart 2001 ve 31 Ocak 2003 arasındaki RXTE-PCA gözlemlerinin analizleri sunulmuştur. İki farklı zaman dilimi için zamanlama çözümleri elde edilmiştir. Buna ek olarak, 1991 ve 1999 yılları arasındaki CGRO-BATSE verilerinde X-ışını akısı ve frekans türevi arasındaki bağıntının episodik olarak mod değiştirdiği görülmüştür. SWIFT J0513.4-6547 sistemi için, 2009 ve 2014 yıllarındaki parlamaları detaylı bir şekilde incelenmiştir. Elde edilen sonuçlarda, kaynağın parlamalar arasındaki sönük olduğu sürede atarcanın atım frekansının ortalama olarak $\sim 1.52 \times 10^{-12}$ Hz/s ile azaldığı görülmüş, ve yüzey manyetik alan şiddetinin $\sim 1.5 \times 10^{13}$ G olduğu çıkarımı yapılmıştır. X Persei için 1998 ile 2010 arasında yer alan RXTE and Integral uydularının gözlemleri incelenmiştir. Bu sistemde, frekans türevinin X-ışını akısına olan bağıntısında yıldız rüzgarından kütle aktarımının var olabileceğine dair emareler görülmüştür. Zaman-

lama gürültüsü tayfında, indisi ~ -1 olan kırmızı gürültü bileşeni ile beraber uzun zaman ölçeklerinde diskten yapılan kütle aktarımını baskılayan bir gürültü bileşeni gözlemlenmiştir. SXP 1062 için, atarcanın istikrarlı bir şekilde $-4.29(7) \times 10^{-14}$ Hz/s hızında yavaşladığı gözlemlenmiş, ve manyetik alan şiddetinin $\sim 1.5 \times 10^{14}$ G olduğu çıkarımı yapılmıştır. Ayrıca, bu atarca için yürütülen zamanlama analizi kütle aktarımı yapan atarcalar için sıradışı bir durum olan $\Delta \nu = 1.28(5) \times 10^{-6}$ Hz büyüklüğünde periyod kaymasını açığa çıkarmıştır. İzole olan atarcalarda periyot kaymasıyla sıklıkla karşılaşılmasına rağmen, kütle aktarımı yapan atarcalarda bu durum daha önce gözlemlenmemiştir. Bu periyot kayması keşfi kütle aktarımı yapan sistemlerde de bu olayın yaşanabileceğini gözler önüne sermiştir.

Anahtar Kelimeler: Nötron Yıldızları, Kütle Aktarımı Yapan Atarcalar, Kütle Aktarım Torkları, X-Işını Çift Yıldız Sistemleri

To my family

ACKNOWLEDGMENTS

I would like to state my sincere gratitudes to my supervisor Prof. Dr. Altan Baykal to whom I owe my scientific progress. During my graduate studies, he tirelessly encouraged and guided me with his incredible scientific perspective. I would also like to thank my co-supervisor Prof. Dr. Sıtkı Çağdaş İnam for his didactic discussions which provided significant improvements of this thesis. I appreciate the constructive comments and advices of honorable committee members, Prof. Dr. Sacit Özdemir, Assoc. Prof. Dr. Mesut Yılmaz, Assoc. Prof. Dr. Serhat Çakır and Assoc. Prof. Dr. Sinan Kaan Yerli.

I thank my fellow colleagues in our small METU Astrophysics group, especially to Dr. Şeyda Şahiner for the stimulating discussions over fundamental aspects of Astrophysics.

I want to express my gratitudes to my colleague and beloved wife Danjela Serim for her patience and motivation. She assisted me both scientifically and spiritually which fortified my motivation for conducting research and writing of this thesis. Last but not least, I would like to thank to my family: my parents Ayşe and Adnan, my brothers Malik and Mirhan and my son Mikail for supporting me spiritually throughout writing this thesis and my life in general.

TABLE OF CONTENTS

xiv

LIST OF TABLES

TABLES

LIST OF FIGURES

FIGURES

xvii

CHAPTER 1

INTRODUCTION

Stars resume their life with the balance between radially inwards and outwards forces. For a main sequence star, gravity sustains the inwards pressure and outwards pressure arises due to nuclear fusion reactions within the star. Each fusion reaction yields to the creation of heavier elements. The star gradually loses its nuclear fuel and eventually it is no longer able to support itself against the gravitational force by generating outwards pressure from nuclear fusion. This will eventually determine main sequence star's fate at the end of its evolution in cosmic timescales. The compact star formation will happen after this endpoint of the star evolution, and the initial mass of the progenitor main sequence star is the most important factor deciding the star's fate. Consuming its fuel leads to death of the main sequence star and birth of a new compact object (white dwarf, neutron star, or black hole). Even though the exact range is uncertain, the neutron stars are thought to be formed through the core collapse of progenitor star with masses in the range of $8 - 20 M_\odot$. Their cores surpass the Chandrasekhar limit of $1.4 M_\odot$, hence the electron degeneracy pressure cannot sustain enough pressure to prevent gravitational collapse as in the case of white dwarfs. Instead, the internal pressure is supported by the nuclear forces and neutron degeneracy pressure, therefore a star so-called *neutron star* is formed.

Up to today, almost half of the observed stars are found to be in binary systems. Obviously, depending on the type of the star, there will be many possible combinations to yield a binary system. Among those binary systems, this thesis will focus on the binaries with a compact star as a neutron star, and a non-degenerate (usually a main sequence) star as a companion. Understanding what is happening in these systems require information on the formation and characteristics of the given type of compact

star and formation of the binary which will eventually determine the pattern of plasma accretion from one object to another.

1.1 Basic Properties of Neutron Stars

Following the discovery of neutron [1], Baade & Zwicky [2] suggested that stars predominated by these particles, neutron stars, may exist in the universe. The confirmation of this hypothesis took place several decades later when the first radio pulsar was detected [3]. Over the years, observations indicate that neutron star masses lies in the range of $1.25 - 2.0M_\odot$ with typical radii of $10 - 15$ km . Neutron stars also possess extremely high dipolar surface magnetic fields that may reach up to 10^{15} G and they spin so rapidly up to the periods of several milliseconds. In some cases, the beamed emission they emit through their magnetic poles, which is axially tilted with respect to its spin, may swing towards Earth. This emission is observed as pulses from the Earth and therefore such objects are referred to as *pulsars* (Figure 1.1).
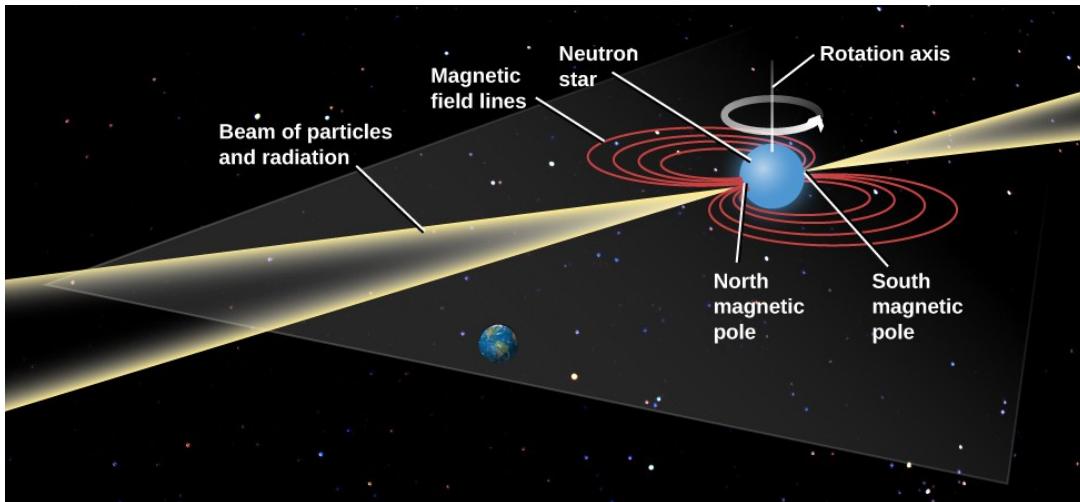
Figure 1.1: An artistic view of a pulsar. In each rotational cycle, the radiation beam sweeps an observer on the Earth, producing the observed pulsations. Picture Credit: Tony Hisgett[1]

The central density of these objects reaches up to several nuclear densities ($\rho \sim 10^{15}$

---

[1]The picture is modified version retrieved from https://courses.lumenlearning.com/astronomy/chapter/pulsars-and-the-discovery-of-neutron-stars/

g/cm^3), making them one of the densest objects in the universe. The neutron stars are thought to be the ideal laboratories for studying physics at extreme density conditions because the ultra-dense matter cannot be employed in laboratory conditions, however; its attributes can be deduced from mass-radius relations of neutron stars [4]. The state of matter inside neutron stars is generally inferred from the relation between the pressure and density, known as Equation of State (EOS). The EOSs are model dependent and each of them predicts different mass-radius relations for neutron stars.
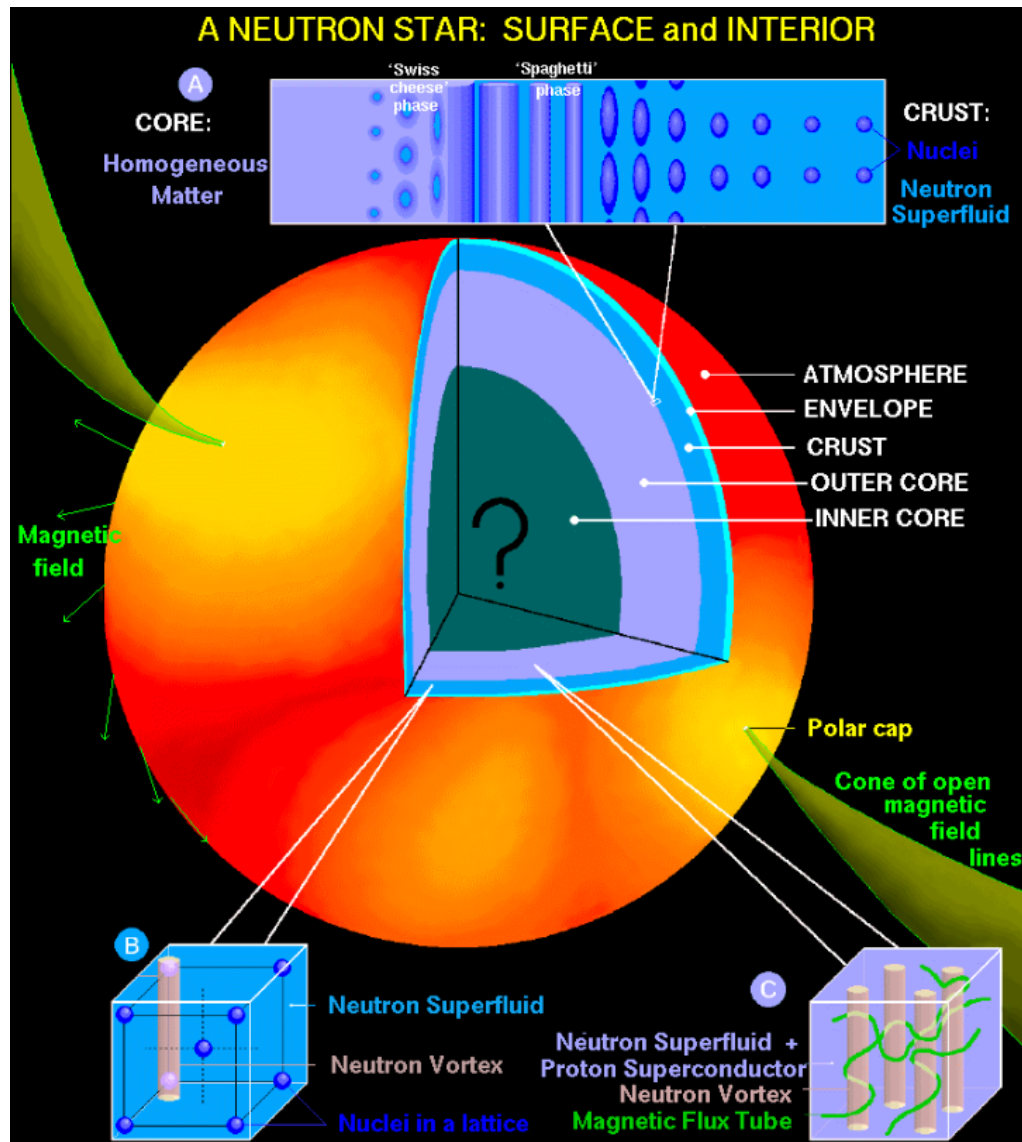
Figure 1.2: Representative diagram of neutron star interior. Picture Credit: Dany Page, Unam[2]

Despite the improvements of EOS models, the actual form and behavior of the matter inside the neutron stars are still substantially vague. But the overall picture of a neutron star is drawn and discussed over several regions; the *atmosphere*, *outer crust*, *inner crust*, *outer core* and *inner core* (see Figure 1.2). Atmospheric structure of the neutron stars is thought to suppressed by the strong gravitational force hence it is ultra thin [5]. Residing under the atmosphere, outer crust governs the heat transport from the core to the surface. The crust is approximately 1 km in thickness and consists of a crystalline lattice of ions with elastic properties. In addition, it is expected to have electrical resistivity which plays a crucial role in the evolution of the magnetic field. In this layer inverse β -decay invokes neutron-rich nuclei ($p + e^- \Rightarrow n + \nu_e$). The crust is also split into two regions; outer and inner crust. Inner crust is referred to the region beyond neutron drip density, where neutrons leak out of nuclei. Beneath the crust, there exist an outer core consisting of superfluid neutrons and superconducting protons, together with electrons and muons. In the center of the neutron star, when the density roughly exceeds 6×10^{14} g cm^{-3}, inner core region begins. The real physical structure of the inner core still is a mystery and many kinds of exotic matter (such as meson condensates, hyperons, quark matter) are proposed to exist within this region.

1.2 Isolated Neutron Stars

Over the last few decades, new surveys and detections not only significantly yielded improvements in our understanding of neutron stars but also revealed unexpected properties of these sources. Observations have shown that isolated neutron stars are found with different characteristics, therefore they are classified in several subgroups such as; *radio pulsars*, *compact central X-ray sources* in supernova remnants, *magnetars*, *transient radio sources* and the famous *magnificent seven*.

Radio pulsars, despite their emission at other wavelengths, identified through their regular pulsations at radio band and their emission is powered by rotational energy loss due to magnetic braking. Over the years, observations showed that their spin periods are widely distributed, ranging from milliseconds to several seconds. Spin-down rates of radio pulsars vary between $10^{-16} - 10^{-14}$ s/s and inferred B-field strengths extends from 10^8 to 9×10^{13} G (see [6] for a review on pulsars). The X-ray emission of

4

these pulsars are composed of two components; thermal and power-law. The thermal component is thought to be originated from residual cooling subsequent to neutron star formation while the power-law component is believed to have a magneto-spheric origin.

Central Compact Objects (CCOs) are soft X-ray emitting neutron stars. They are discovered in the center of supernova remnants (SNRs). Ages deduced from their associated SNRs indicate that CCOs are relatively young neutron stars. Out of 10 confirmed CCOs, only 3 of them have the rotational period ($P \sim 0.1 - 0.4$ s) and derivate measurements ($\dot{P} \sim 10^{-17} - 10^{-18}$ s/s). They show steady X-ray emission with luminosities in the order of $L_x \sim 10^{33}$ erg/s which implies that CCOs are not rotation powered. (see e.g. [7];[8] for a review)

Magnetars are rather slow rotators ($P \sim 2 - 12s$) with high spin-down rates ($\dot{P} \sim 10^{-13} - 10^{-11} s/s$). The inferred dipolar magnetic fields from those values exceed the quantum critical level of $B_{qed} = m_e^2 c^3 / \hbar e = 4.4 \times 10^{14}$ G with several exceptional cases (see [9] for a review). They exhibit frequent bursting behaviors with different properties; short bursts (0.1-10 s) and intermediate bursts (1-40 s) whose spectra can be modeled by thermal emission ([10]) and rare events called *Giant Flares* which are apparently particular to a subclass called *Soft Gamma Repeaters* ([9] [11] [12]).

Rotating Radio Transients (RRATs) are a new set of objects discovered through rapid radio flashes of several milliseconds [13]. Number of known RRATs has grown over the last decade and has continuously been updated by new surveys (see [3] for the catalog RRATs). Their rotational period varies between 0.125 to 7.7 s and only a small fraction of the discovered RRATs have period derivative measurements which range from 5.7×10^{-13} to 1.2×10^{-16} s/s. The emission of RRAT sources cannot be explained with current manifestations, and hence several different mechanisms are put forward to underpin its physics [14], [15], [16].

The magnificent seven, which are also known as X-ray dim isolated neutron stars (XDINs), are X-ray emitting neutron stars located within a few hundred parsecs from the Earth ([17]; [18]). They do not emit in radio wavelengths and their emission in X-ray are mostly dominated by thermal emission. Their pulsation periods lie in the

---

[3] http://astro.phys.wvu.edu/rratalog/

range $P \sim 3 - 10$s and their dipolar magnetic field strengths are in the order of 10^{13}G ([19] and references therein). These sources do not show any sign of magnetospheric activity. Therefore, the observed X-ray luminosities directly originate from the surface, making these sources ideal for studying cooling curves and atmospheric models (see [20]; [21]; [22], for reviews.)

1.3 Neutron Stars in X-ray Binaries

As well as being found isolated, the neutron stars are also profoundly observed in X-ray binary systems. These systems show different types of physical characteristics mostly depending on the mass of the companion, thus they are subdivided into two classes accordingly; the high-mass X-ray binaries (HMXBs) and the low-mass X-ray binaries (LMXBs). In the following sections will summarize the basic properties of LMXBs and HMXBs which contain a neutron star.

1.3.1 Neutron Stars in LMXBs

The low-mass X-ray binaries are rather old systems ($\sim 10^9$ yr) that harbour a compact object and a low-mass donor (typically $M < 1\,M_\odot$) [23]. Figure 1.4 represents an artistic view of such system. With the recent developments in instrumentation, the number of detected systems have rapidly grown (around 187 LMXBs are cataloged in SMC, LMC and our galaxy [24]). In X-ray binaries with low mass companions, the faint and weak stellar wind is insufficient to empower observed X-ray emissions. Thus, in such systems the principal channel relevant to mass accretion is associated with Roche Lobe Overflow (RLO). In the case of LXMBs harbouring a neutron star, the infalling matter will form an accretion disk until the magnetoshperic boundary is reached (see Section 2.2.1 about details of RLO and magnetospheric radius). The additional angular momentum provided by accretion will usher the neutron star into more rapid rotation [24]. It may become so rapid that the neutron star may revolve in milliseconds [25]. So far more than 40 of such millisecond binary systems are discovered in the Galactic Disk [26].

ZAMS	●	•		1500 days	0.0 Myr
	15.0	1.6			
Roche-lobe overflow				1930 days	13.9 Myr
	13.0		1.6		
common envelope + spiral-in					
	4.86				
helium star				0.75 days	13.9 Myr
	4.86	1.6			
supernova				1.00 days	15.0 Myr
	3.99	1.6			
neutron star	○	●		2.08 days ecc=0.24	15.0 Myr
	1.3	1.6			
LMXB				1.41 days	2.24 Gyr
	1.3	1.59			
millisecond pulsar	○ 1.50	○ 0.26 (PSR 1855+09)	white dwarf	12.3 days	2.64 Gyr
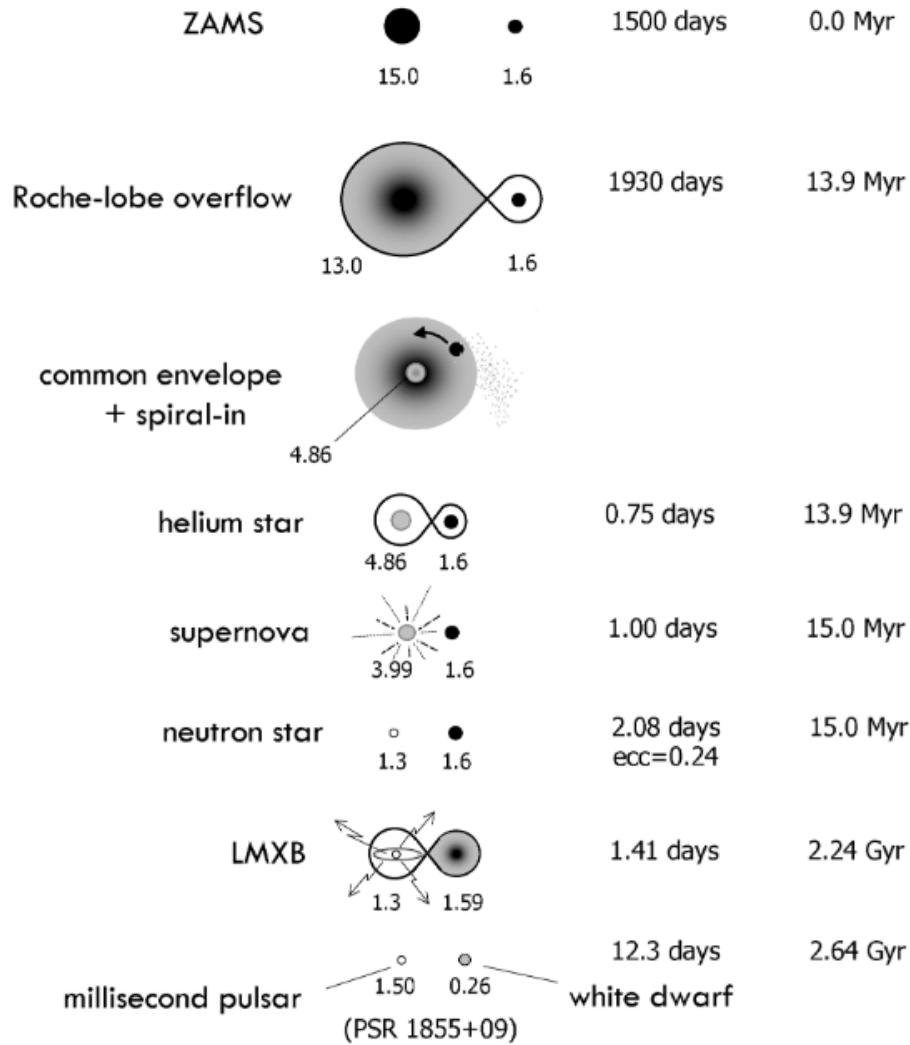
Figure 1.3: A representative illustration of evolution of a binary system which yields to a LMXB. The formation scenario is adjusted for the parameters of the particular millisecond binary system PSR 1855+09. [26]

LMXBs are thought to be the descendants of a zero-age main sequence star (ZAMS) binary systems with excessive mass ratios [26]. In the binary, the higher-mass ZAMS evolves more rapidly in astrophysical timescales ($\sim 10^7$ yr). Hence it quickly reaches core-collapse supernova stage and forms a neutron star (NS). At this timescale, low-mass companion is not yet evolved. It takes rather longer time for low-mass companion to evolve and to fill the Roche Lobe ($\sim 10^9$ yr). In addition, the orbital separation shrinks over time which results in lower Roche Lobe radii. LMXBs are observed to have close orbits (generally less than few days of orbital periods) which supports the

orbital shrinkage scenario. After the Roche Lobe is exceeded, the neutron star commences accretion which leads to an observable LMXB system (see Figure 1.3 for an example scenario by [26]).
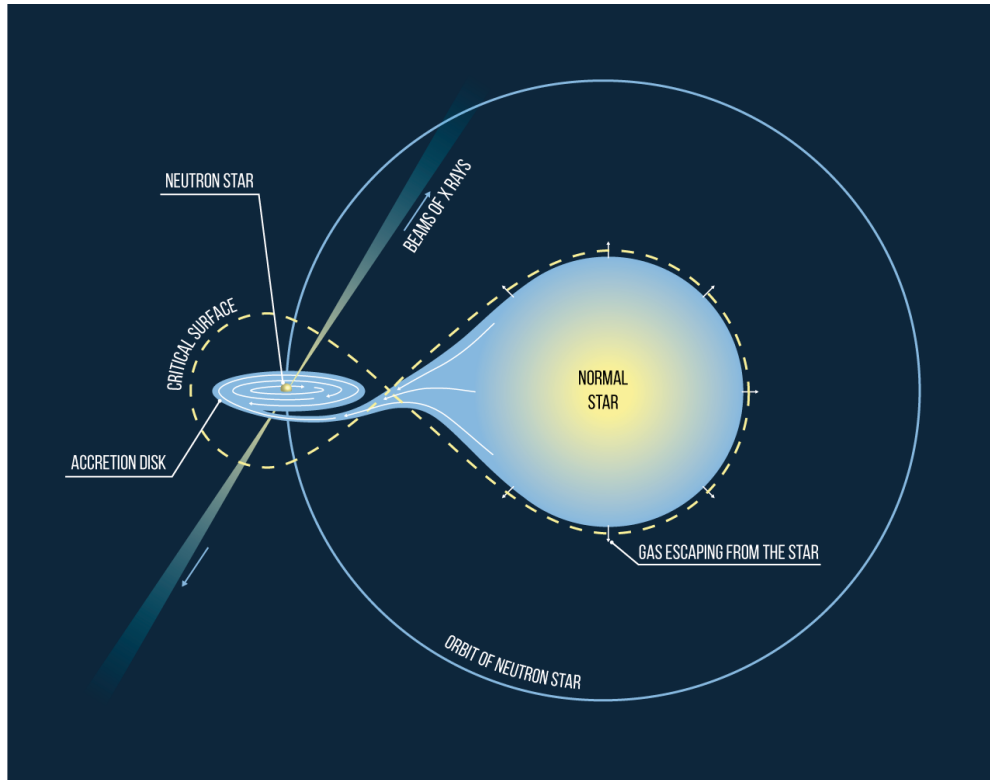
Figure 1.4: Artistic image of accretion of an LMXB. Picture Credit: MIPT[4]

From evolutionary perspective, those neutron stars should have a weak field (generically in the order of $B \approx 10^7 - 10^9$) as it decays gradually ([27]; [28]; [29]). Moreover, the weakness of the B-field also give accretion disk an opportunity to circulate at closer distances to the NS [30]. With the mass arriving at the NS's surface, X-ray emission is generated. Due to viscous dissipation, the disk will is heated up to $\sim 10^7$ K at inner regions. Thus, radiation at the inner parts of the disk will also correspond to X-ray band. At outer radii, the disk mostly emits in optical band by reprocessing the high-energy radiation generated at smaller radii. X-ray emission at smaller radii may also irradiate the companion. Observing the X-ray emission both from the NS surface and the disk provides a unique probe to measure NS parameters [31].

---

[4]retrieved from https://mipt.ru/english/news/x_ray_pulsars_fade_as_propeller_effect_sets_in

Many of the LMXBs exhibit rather sharp increase in X-ray luminosity (~ 1 order of magnitude) within several seconds [32]. These frequently occuring events (every hours to days) are referred to as *Type-I X-ray bursts*. Lasting for $\sim 10 - 100$ s, the burst releases an energy in the order of $\sim 10^{39}$ erg [33]. Posterior studies have revealed that flux enhancements during *Type-I X-ray bursts* are emerged from unstable nuclear burning of the accumulated matter on the NS surface ([34]; [35]; [33]). The idea of thermonuclear burst at the surface is further supported by the estimated size of the emission area deduced from spectral analysis ([36];[37]).

The current X-ray missions do not provide enough spatial resolution to distinguish the disk and NS emission, however; most of the physical properties can be deduced from X-ray spectral and timing analysis of their data. For example, sub-millisecond timing accuracies of these missions enabled the discovery of rapid *burst oscillations* ($300 - 600$ Hz). These oscillations firstly identified within high resolution power spectra of the source 4U 1728–34 [38]. Later on, it is realized that amplitude of the burst oscillations are in anti-correlation with the X-flux during the rise episode of the burst [39]. This anti-correlation indicates that spin modulation of an initially localized thermonuclear burning region is spread all over the neutron star within a second.

1.3.2 Neutron Stars in HMXBs

High mass X-ray binaries (HMXBs) are rather young ($\sim 10^7$ yr) hard X-ray emitting > 15 keV sources [26]. In a generic system, a compact object receives mass from an evolved massive companion (typically $> 10 M_{\odot}$). Figure 1.5 exemplifies a picture of a conventional HMXB together with a LMXB (retrieved from [26]). The number of cataloged sources of this type reached to ~ 114 in our Galaxy [40]. In these systems, primary course of accretion is the intense wind provided by the companion, however; RLO is also possible. The course of accretion depends on the environment stipulated by the companion and these systems are further split to sub-classes accordingly. Details of both of the accretion types are reviewed in Section 2.2. If the companion is of Be or Oe type star and produce a *decretion disk* around itself, the compact object mainly interacts with the disk on the cycles of orbital passages and the system is referred to as *BeXBs*. On the other hand, if the companion is of supergiant (Sg) type

and decretion disk is absent, then the compact object will gather mass either via the stellar wind or Roche-Lobe overfilling companion, which are referred to as *Wind-Fed SgHMXBs* and *Disk-Fed SgHMXBs*, respectively.
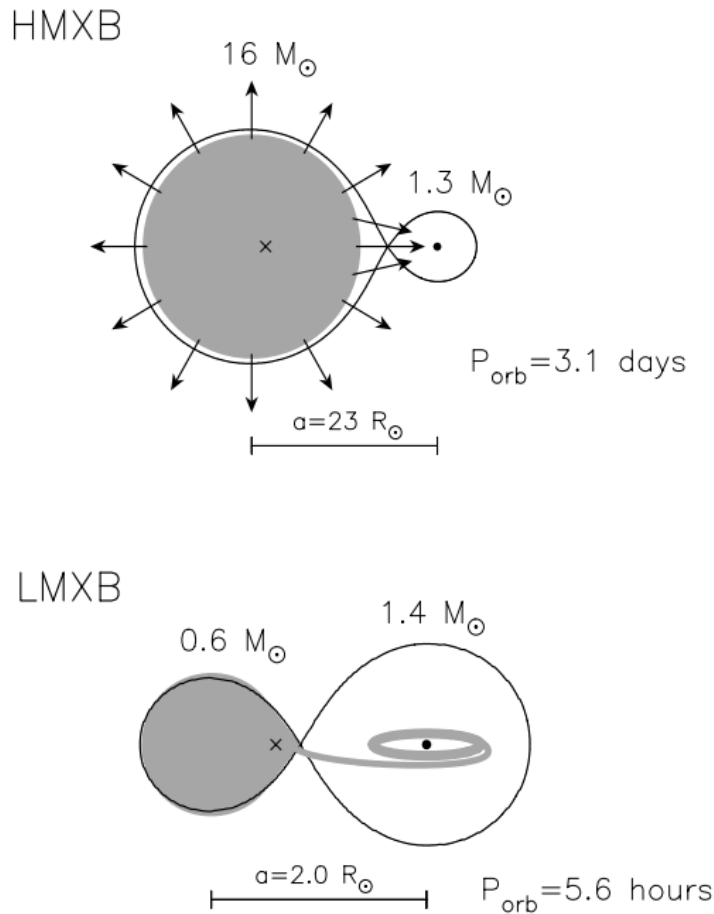
Figure 1.5: An example illustration of a HMXB (upper panel) and a LMXB (lower panel). [26]

HMXBs are considered as the descendants of two massive ZAMS (with $M > 12M_\odot$) [26]. These systems promptly evolve in cosmic timescales ($\sim 10^7$ yr), hence they are relatively younger systems when compared to LMXBs. The quicker evolving more-massive ZAMS in the systems undergoes a supernova and leaves a compact object (in our case a neutron star) behind. The companion enters to a giant phase in which it feeds the NS either with the wind or with RLO. Eventually leaving the stage for an observable HMXB (see Figure 1.6 which is retrieved from [26]).

In the following section, the physical properties and accretion mechanisms of the
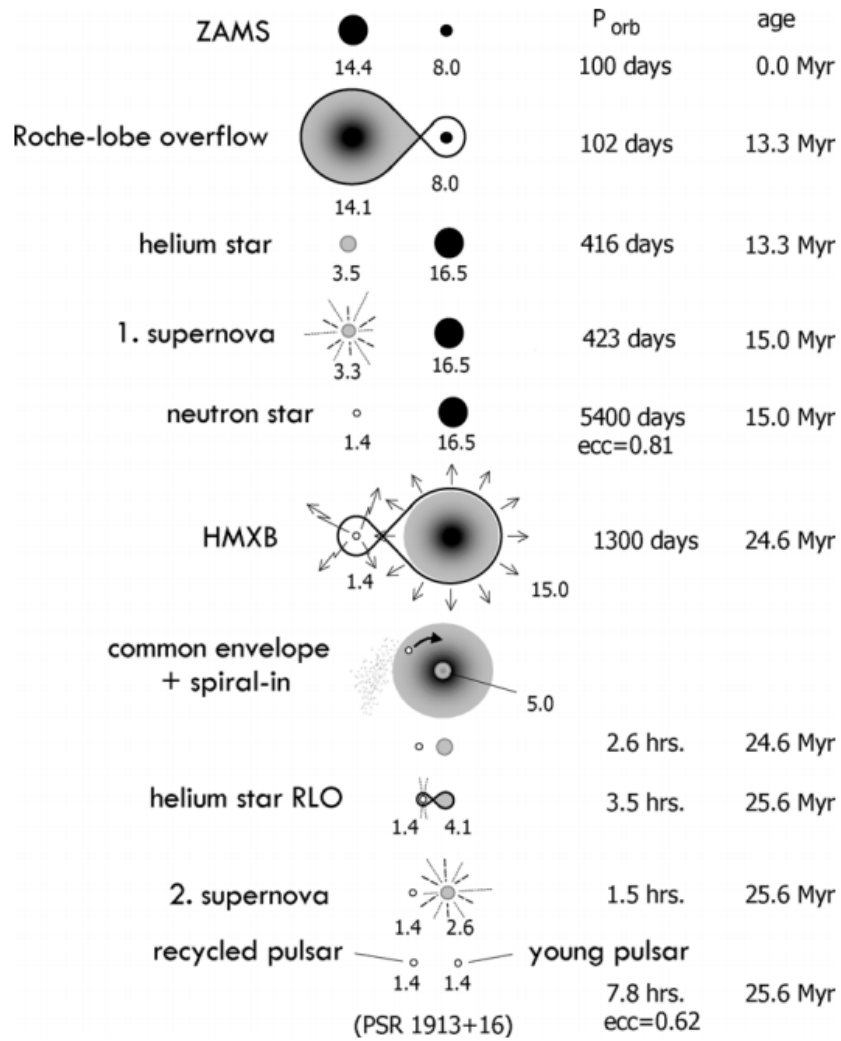
Figure 1.6: A representative illustration of evolution of a binary system which yields to a HMXB. The formation scenario is adjusted for the parameters of the particular double neutron star binary system PSR 1913+16. [26]

HMXB subclasses; Disk-fed SgHMXBs, Wind-fed SgHMXBs and BeXBs will be described.

1.3.2.1   Disk-fed SgHMXBs

Disk-fed SgHMXBs constitutes a rare subclass of HMXBs where RLO mechanism is possible. In these systems, the matter exceeding the RL proceed on a path towards the NS which passes through inner Lagrangian Point (L_1). Then, the mass begin to follow

a spiral trajectory and eventually shape an accretion disk. Section 2.2.2 reviews the details of accretion by virtue of RLO. With the stable accretion rates sustained by the disk, disk-fed SgHMXBs are able to radiate in X-rays with luminosities in the order of $L_x \sim 10^{37} - 10^{38}$ erg/s. The neutron stars in disk-fed SgHMXBs have both short spin periods ($P_{spin} \sim 0.7 - 14$ s) and orbital periods ($P_{orb} \lesssim 4$ days). Primary studies reveal that these binaries an in anti-correlation in P_{orb} vs P_{spin} phase space ([41]; [42]) which confirms their disk-fed nature (Figure 1.8). Unfortunately, this subclass have a very few members (RX J0648.1–4419, LMC X–4, SMC X–1 and Cen X–3), thus the overall picture of the nature of these systems is not yet conclusive.

1.3.2.2   Wind-fed SgHMXBs

Wind-fed SgHMXBs host a donor of OB spectral type which feeds the accompanying NS through its stellar wind. This steady wind is captivated by the NS and the accretion scenario is established over Bondi accretion process described in Section 2.2.3. The inhomogeneous plasma clumps within the wind trigger notable short-timescale fluctuations in their luminosities which are varying in $L_x \sim 10^{35} - 10^{36}$ erg/s level. Systems of this subclass generally have short orbital periods ($\lesssim 15$ d) with minor traces of eccentricities ([43] and references therein). But still, orbital separations are relatively broad when disk-fed types are compared. The inefficient wind accretion do not feed enough angular momentum to the NS in the system to reach short spin periods, thus their spins typically reside in the range of $\sim 10^2 - 10^3$ s. A further dichotomy of this class is introduced to distinguish the intrinsic properties of individual systems.

The first type is the *Obscured SgHMXBs* which are identified through strong absorption features in the X-ray spectra (typically $n_h \gtrsim 10^{23}\, cm^{-2}$). They are in a tight orbit (with $P_{orb} < 10$ d) where NS accretion is maintained with slow winds [44]. Hosting an O8-B1 type companion, Obscured SgHMXBs possibly enter to phases of common envelope as inferred by the studies in the optical band [43]. These systems are also reckoned as *transitional* stages through RLO systems [44].

The second type is the *Super Fast X-ray Transients* (SFXTs) which are recognized with occasionally recurrent fast and transient bursts [45]. During bursting episodes,

quiescent X-ray luminosities ($\sim 10^{32} - 10^{34}$ erg/s) are enhanced by approximately 4 orders in magnitude within tens of minutes and thrust out to $\sim 10^{35} - 10^{37}$ erg/s at the peak [43]. For most of the sources of this type, the bursting events seem to be unconnected with a definite orbit-phase [43]. On the other hand, several sources seem to share joint traits with BeXBs. These systems harbour a NS with pulsations ranging from several secons to ~ 1000 seconds and B-field of $\sim 10^{11-12}$ G [43]. The origin of peculiar bursting behavior in SFXTs are not yet reached to a conclusive consensus and there is an ongoing-debate on the possibilities of clumpy winds [46], anisotropic equatorial winds ([47]; [48]) and propeller stage [49].

1.3.2.3 BeXBs

BeXBs are binary systems including a neutron star and non-supergiant Oe or Be-type star as donor. These sources constitute more than 60% of HMXB population. The donor star is very massive ($10 - 20 M_\odot$) and of III-V luminosity class (see e.g., [50]; [42] for reviews). The Be donor stars exhibit both excess infrared emission [42] and
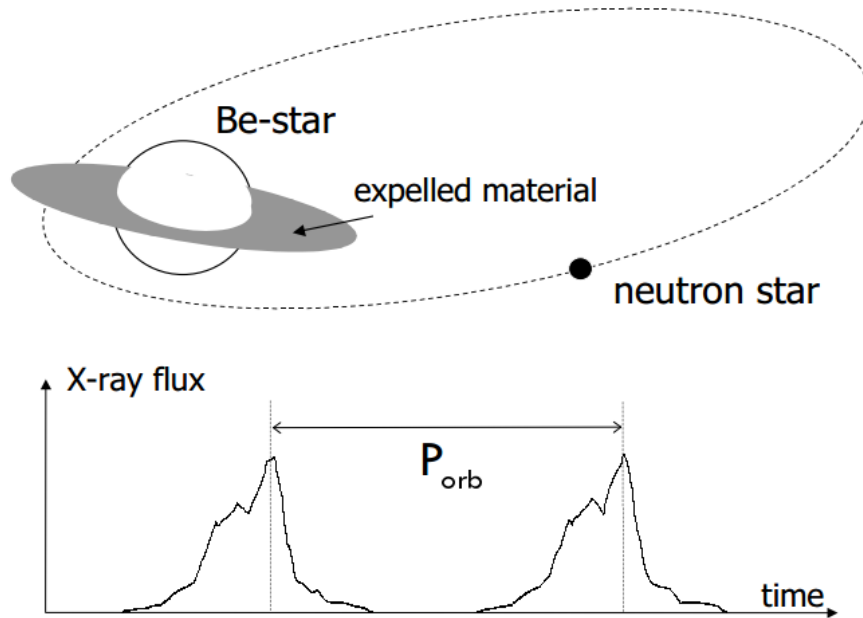
Figure 1.7: A simple schematic of recurrent disk-pulsar interaction and associated X-ray flux variations. [26]

Balmer and Paschen series hydrogen emission lines which are regarded as an indicator of the existence of a circumstellar disk around the donor star. Thus, these binary systems have a transient nature because of the donor star's disk and neutron star interaction during passages through the disk (See Figure 1.7) although there exist several exceptional cases where the binary is found to have persistent emission (e.g. X-Per; [51]). The disk is formed at the equatorial plane ([52]; [53]) and sporadically expands (till 6-20 R_{Be}) up to enclosing whole binary [54]. In general, transient BeXBs revolve at wide ($P_{orb} > 20$ days) and eccentric $e \geq 0.3$ orbit trajectories [42]. Due to these orbital trajectories, the neutron star only interacts with the disk during its passage at the closest distance to the donor [55]. During this interaction, amount of inflowing (accreted) matter rapidly increases and X-ray flux is enhanced ($L_x \sim 10^{35} - 10^{37}$ erg/s) by high mass accretion rate (e.g., [56], [57]). As a consequence, the system enters the outburst state lasting around a week, called Type-I outbursts.
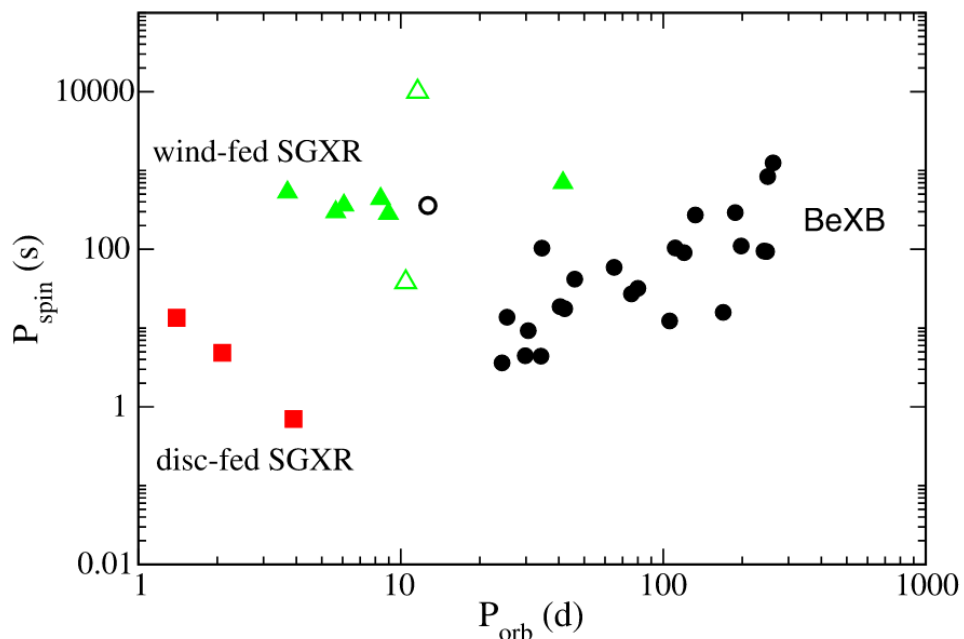
Figure 1.8: Corbet diagram of accreting pulsars. Green triangles: wind-fed SGXRBs, Red squares: disk-fed SGXRBs, Black dot: BeXRBs. [42]

Apart from these periodic events, NS spends most of its time at large distances from the companion due to wide orbital separation [55]. At this time interval, mass accretion almost ceases [58]. Therefore, transient systems are observed at rather low

($L_x < 10^{33}$ erg/s) quiescent luminosities (e.g., [59]). However, sometimes an orbital-phase-independent (Type-II) outbursts are observed. During Type-II outburst, X-ray luminosity rises up to Eddington limit ($L_x \sim 10^{38}$ erg/s) which decays over longer period of time (weeks to months) compared with Type-I outbursts. Even though the origin of these outbursts are not yet clear, increased companion activities are considered as a source of empowering such bursts ([50]; [60]). On the other hand, persistent BeXBs posses a slowly rotating neutron star ($P_{spin} \geq 200$ s) revolving at a wide orbit ($P_{orb} \gtrsim 200$ d). The persistent systems are less variable in X-rays and have luminosities in the order of $L_x \lesssim 10^{36}$ erg/s [42].

Corbet (1986) investigated the distribution of these pulsars in P_{spin} vs P_{orb} phase space and demonstrated that these sources have a positive correlation. Thus, the distribution of accreting pulsars in P_{spin} vs P_{orb} phase space is later referred to as *Corbet Diagram* (see Figure 1.8). The trends within the Corbet Diagram implies different accretion mechanisms. The positive correlation of BeXBs signifies that pulsars spin slower in wider orbits. It indicates that pulsars at wider orbits interact with outer regions of the disk, thus the pulsar accretes from less dense regions. Therefore, being exposed to less torque, neutron stars in wider orbits have longer equilibrium spin periods. Moreover, it is also regarded as an indicator of the formation of a transient disk [61].

1.4 Thesis Organization

This thesis is devoted to examine the physical properties of pulsars which are validated through timing analysis. All the sources of interest are pulsars that are residing in a binary system and accreting the mass catered by its companion. Namely, these sources are SWIFT J0513.4–6547, SXP 1062, GX 1+4, and X Per. This work utilizes the data gathered by various X-ray missions; Rossi X-ray Timing Explorer (RXTE), SWIFT, X-ray Multi-Mirror Mission (XMM-Newton), Chandra and International Gamma-Ray Astrophysics Laboratory (INTEGRAL). The upon usage, the properties and data reduction procedure of each mission is mentioned in relevant sections.

In Chapter 2, the fundamental theories are reviewed regarding emission of both isolated and accreting pulsars. For isolated pulsars, the chapter covers the particular case of X-ray radiation due to magnetic braking. For the accreting sources, the fundamental physics of the accretion mechanisms is presented with an aim of building an essential comprehension. The accretion theories are described for both wind and disk and brought into contact with different models.

Chapter 3 focuses on the analysis methods that the thesis is build upon. Section 3.1 lays the foundation of timing techniques used in this thesis, covering both pulse timing methodology and epoch folding. Then, in Section 3.2 the technique of timing noise investigation and relevant analysis procedures are demonstrated.

Chapters 4 through 7 represent the results of timing analysis of each X-ray binary. In each of these chapters, a brief information about the observation sequence and reduction methodology is reported. Later sections describe the relevant analysis procedures and discuss the physical interpretations of findings of each study. Finally, Chapter 8 summarizes the results of this thesis.

CHAPTER 2

ROTATION AND ACCRETION POWER

2.1   Rotation Power

This section focuses on X-ray emission from isolated neutron stars. For isolated NSs, X-ray radiation is thought to be powered by internal heat reservoir or the rotation of NSs. Radiation due to heat reservoir is generally deduced from soft X-ray emission of young NSs. On the other hand, rotational power loss may invoke pulsed emissions and pulsar wind nebulae (PWN).

For rotation-powered pulsars, the rotational energy loss is associated with magnetic dipole braking. Assuming that a pulsar purely radiates in magnetic dipole form, Larmor radiation of a magnetic dipole can be expressed as;

$$P_{dipole} = \frac{2}{3} \frac{\ddot{\mu}_\perp^2}{c^3}. \tag{2.1}$$

The $\mu_\perp$ is the component of the magnetic dipole projected along the spin axis which is tilted with an angle α (see figure 2.1). The magnitude of the magnetic dipole is proportional to its magnetic field B and radius R as $\mu \propto BR^3$. If the pulsar rotates with an angular frequency ω, then the magnetic dipole can be expressed as; $\mu_\perp = |\mu_\perp|e^{-i\omega t} = \mu \, sin\alpha \, e^{-i\omega t}$. Hence, the dipole radiation of such an oblique rotator is expressed as;

$$P_{dipole} = \frac{2}{3} \frac{\ddot{\mu}_\perp^2}{c^3} = \frac{2}{3c^3} (\omega^2 BR^3 sin\alpha)^2 \tag{2.2}$$

As stated earlier, The spin luminosity of the pulsar is specified by rotational energy loss as $\dot{E} = I\omega\dot{\omega}$ where I is the moment of inertia of the NS. By matching those two equations, pulsar's dipolar magnetic field can be approximated in terms of two
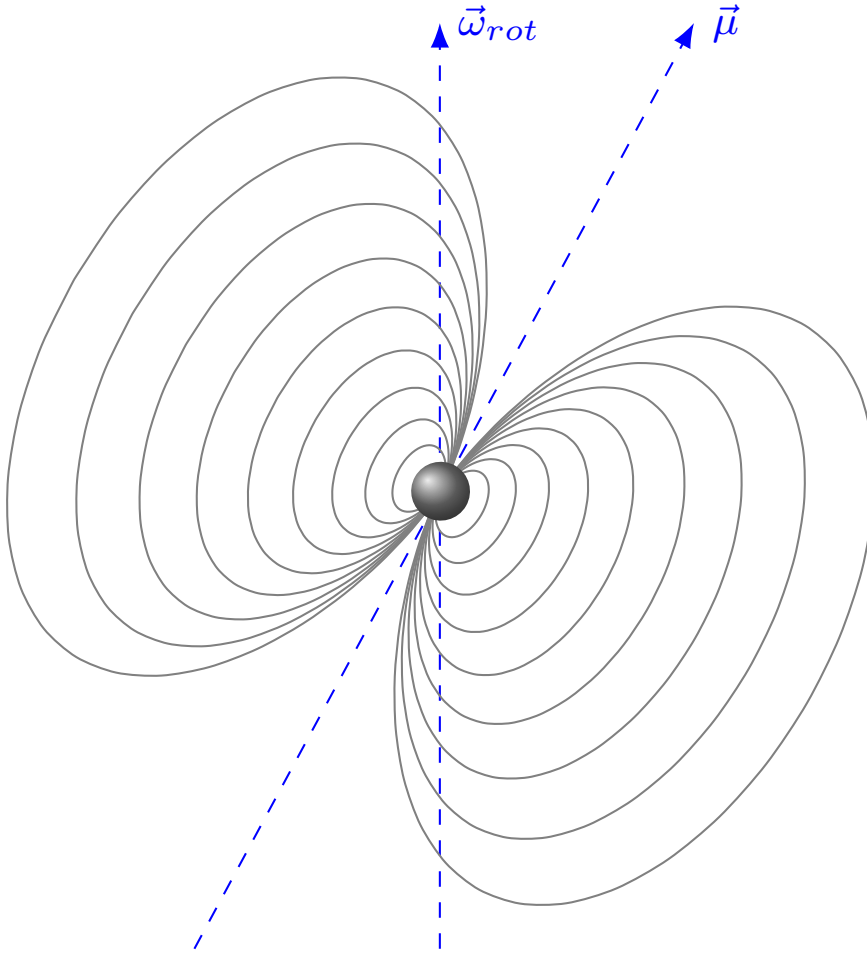
Figure 2.1: Schematic illustration of an oblique rotator pulsar

observable quantities; rotation period P and slow down rate $\dot{P}$ of the NS as;

$$B \simeq \left(\frac{3}{2} \frac{Ic^3}{R^6 sin^2\alpha} \right)^{1/2} \sqrt{P\dot{P}}. \tag{2.3}$$

Using the canonical values of NS moment of inertia $I \sim 10^{45}$ g cm^2 and the radius $R \sim 10^6$ cm, the minimum value of the magnetic field at the surface can be approximated as;

$$B \simeq 3.2 \times 10^{19} \sqrt{P\dot{P}} \quad \text{Gauss} \tag{2.4}$$

The equation 2.4 connects the B-field with two simple observables P and $\dot{P}$ and it is commonly used for approximating dipolar field strengths of isolated pulsars. This approximation actually delivers an order-of-magnitude estimation of the field

strength. Estimated B-fields from equation 2.4 of pulsars show distinct varieties. For example, in radio pulsars 10^8 to 9×10^{13} G is observed [6] while in the case of magnetars, it can be as high as $\sim 10^{15}$ G [9] exceeding the B_{qed} level. Moreover, for a NS born with initial rotation period P_0, the age of the pulsar, τ, can be estimated via;

$$\int_{P_o}^{P} P dP = \int_{0}^{\tau} [P\dot{P}] \, dt \tag{2.5}$$

The term inside the integral on the right side is related with the magnetic field as derived above (i.e. $[P\dot{P}] \propto B^2$). Assuming that the perpendicular component of the magnetic field does not significantly decay over time, this term can be regarded as constant and can be taken out of integral. Thus, the result of the integral can be obtained easily as $\frac{1}{2}(P^2 - P_0^2) = P\dot{P}\tau$. If the pulsar's current rotation period is much larger than its initial spin period $P \gg P_0$, then the pulsar's age can be approximated as;

$$\tau \equiv \frac{P}{2\dot{P}}. \tag{2.6}$$

This calculated age is referred to as *characteristic age* of the pulsar. It is not the actual age of the pulsar but it provides a rough estimate of it. For example, Crab Pulsar, which is known to be born in a supernova explosion observed by Chinese astronomers in A.D 1054, has an actual age of 964 years [62]. Accurate measurements of its timing parameters have shown that its spin frequency is 29.946923(1) Hz which is slowing down at a rate of $-3.77535(2) \times 10^{-10}$ Hz/s [63] The characteristic age deduced from these parameters is around 1257 years. Although τ values seem to deviate from the actual age, precise measurements of pulsar spin parameters offer an estimation of physical parameters such as B, τ and $\dot{E}$ at least up to an order of magnitude, even with such a simple approach. More accurate and realistic calculations require to consider magnetic field decay and inclination angle α variations. There are several studies trying to remedy this problem (e.g. [64];[65]) but the exact picture is not yet conclusive.

Rotational period measurements can also be used to understand pulsar population through P - $\dot{P}$ diagram (figure 2.2). Using the equations derived above, one can draw certain lines to indicate different levels of magnetic field B and characteristic age τ on the P - $\dot{P}$ phase space. Considering the lines, P - $\dot{P}$ diagram can be used to distinguish pulsar subclasses. Younger pulsars not only rotate more rapidly but
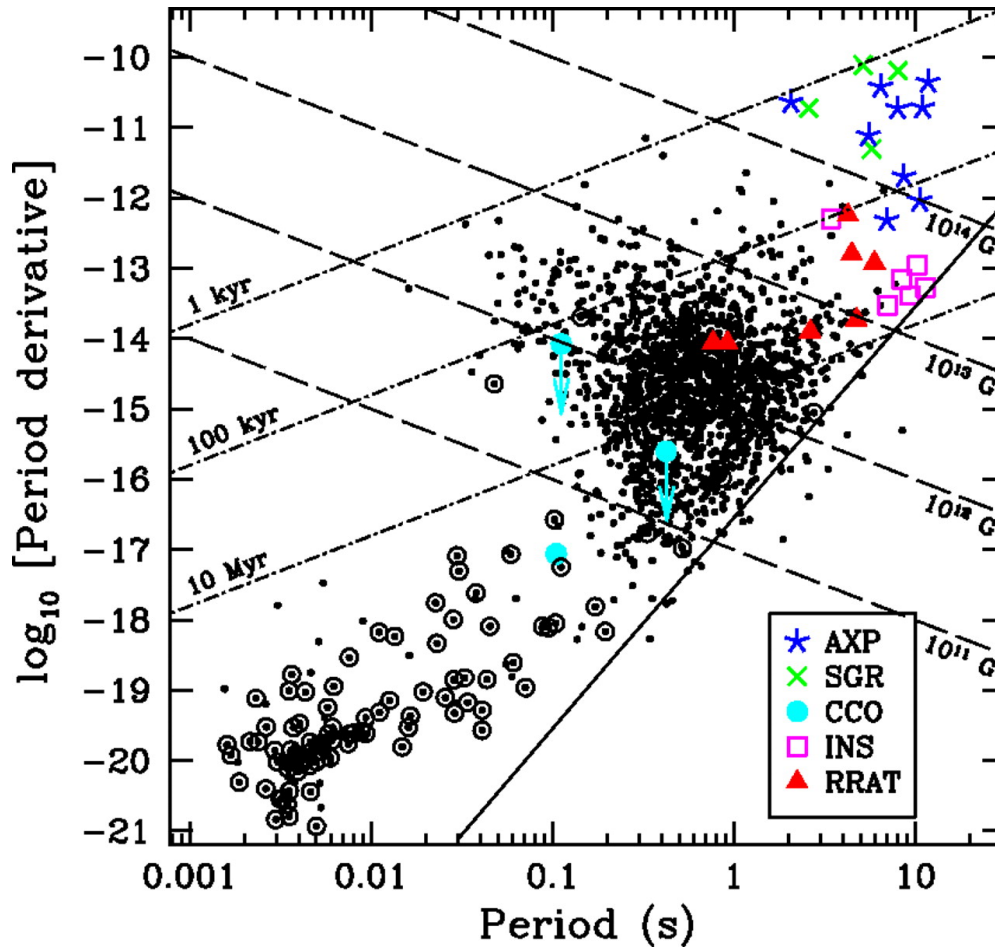
Figure 2.2: P - $\dot{P}$ diagram of pulsars. Small black dots: RPPs, blue and green crosses: AXPs and SGRs, cyan circles: CCOs, mageneta squares: INS, red triangles: RRATs, open circles: binary systems. [6]

also slow down at high rates, therefore they are mostly located at the top left area. The magnetars (AXPs and SGRs), with their immense magnetic fields and high spin down rates, are positioned at the top right. The radio pulsars, on the other hand, are distributed in the central region. Binary systems (mostly consisting of millisecond pulsars) reside at the bottom left corner.

2.2 Accretion Power

Mass transfer and accretion in binary systems were initially proposed as possible mechanisms that act as an energy source for X-ray sources and quasars ([66]; [67]).

Following the discovery of HMXBs in the 1970s [68], accretion mechanisms became an active area of research.

Pulse frequency variations of accreting neutron stars a reveal variety of timing behavior. First of all, observed pulse frequencies include *Doppler Delays* associated with their orbital motion. Furthermore, the rotational motion of many sources are observed to accelerate (spin-up) or decelerate (spin-down) while most of the sources show both acceleration and deceleration episodes. Finally, they show timing irregularities associated with either interior structure or torque fluctuations at the boundary. Both spin-up/down trends and timing irregularities of these sources are mainly governed by the torques exerted during accretion. Thus, in the following sections, the fundamental physics behind the different accretion processes will be described.

2.2.1 Fundamentals

Roche Lobe

The concept of equipotential surfaces lays the foundation of the accretion process because mass transfer begins when a material is able to exceed the critical equipotential surface called *Roche Lobe* and reaches to the region where gravitational force of the compact object is more dominant. Obviously, an isolated star forms nearly spherical equipotential surfaces around itself but in the presence of a binary system, geometry of equipotentials will become more complex. In binary systems, *Roche Lobe* turns out to be more tear-drop shaped. To describe these surfaces, one needs to examine the trajectory of a test particle in the presence of two stars (with masses M_1, M_2, and positions r_1, r_2 in a synchronized rotation with angular velocity ω) which are revolving around common center of mass. In such a case, effective potential of the system is described as;

$$\Phi_{eff} = -\frac{GM_1}{|r - r_1|} - \frac{GM_2}{|r - r_2|} - \frac{1}{2}(\omega \times r)^2 \qquad (2.7)$$

where r is the position of the test particle. The above equation can be understood as follows; the first two terms are gravitational potentials of each star and the last term corresponds to centrifugal potential.

21
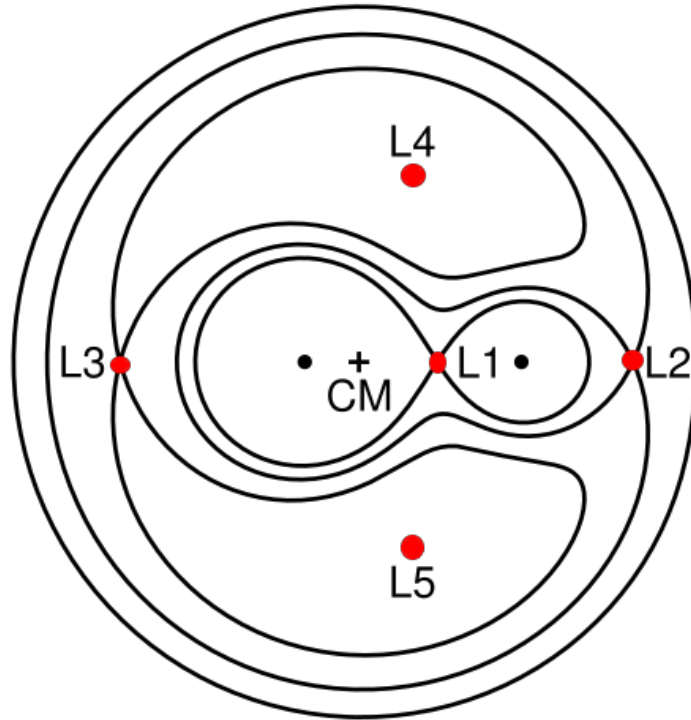
Figure 2.3: The equipotential surface solutions for mass ratio $M_1/M_2 = 3$. The solid lines indicate the 2D geometry of equipotential surfaces. Black dots; positions of the stars, Plus sign; position of the center of mass, Red dots; Lagrangian Points. Picture Credit: Wikimedia[1]

The stationary points of the potential can be obtained by examining the extrema of the effective potential (i.e. $\nabla\Phi_{eff} = 0$). These solutions yield five different points which are called *Lagrangian Points*. The equipotentials generated by solving the equation 2.7 are represented in figure 2.3 (for a mass ratio of $M_1/M_2 = 3$). The first point L_1 is called *inner Lagrangian Point*. The equipotentials of both stars coincide at this point and therefore net force on a test particle is zero. During the late stages of stellar evolution, donor star expands and may exceed its Roche Lobe[2]. As a consequence, exceeding mass is no longer attached to the donor star and it starts to flow through the compact object via L_1 point. This process is referred to as *Roche Lobe Overflow*. Details of different types of accretion mechanisms, including Roche Lobe Overflow, will be discussed in following sections.

---

[1]https://commons.wikimedia.org/wiki/File:Roche_potential_contours_q%3D3.svg
[2] Roche Lobe can also be exceeded with orbital shrinkage

The Roche geometry described in section 2.2.1 is built on three main assumptions. The first one is that the gravitational potential fields of both compact object and donor star are generated by point masses. This assumption is not that irrational, regarding the fact that even a star is about to fill its Roche Lobe, most of the mass still reside in the center and have an almost spherically symmetrical geometry. Secondly, the orbit of the binary system assumed to be circular. Lastly, it is assumed that the rotation of the stars and the orbit are synchronized, because the Roche geometry described in section 2.2.1 is valid if matter co-rotates with the orbit. The second and third assumptions require reconsideration regarding binary evolution. A detailed description of different accretion schemes under distinctive physical conditions will be presented in the following sections.

Eddington Limit

In the most basic picture, there will be a mass transfer from donor to the compact object and during the accretion process, the gravitational potential energy of in-falling material can be converted to radiation. The luminosity generated during this process, *accretion luminosity*, can be described as;

$$L_{acc} = \frac{GM\dot{m}}{R} \tag{2.8}$$

where G is the gravitational constant, $\dot{m}$ is the mass accretion rate, M and R are the mass and radius of the compact object, respectively. The equation indicates that L_{acc} scales with increasing $\dot{m}$. However, L_{acc} is limited due to the fact that beyond a certain point radiation pressure will overcome gravity. This upper limit for L_{acc} is referred as *Eddington Luminosity*. In most of the cases, companion star is a main sequence type star, hence it can be assumed that the in-falling material is mostly composed of ionized hydrogen. Assuming that in-falling plasma is fully ionized, the gravitational force on the electron-proton pair will be

$$F_{gr} = \frac{GM(m_p + m_e)}{r^2} \approx \frac{GM(m_p)}{r^2}. \tag{2.9}$$

where the term due to electrons are neglected since $m_p >> m_e$. On the other hand, the electrons in the plasma feel the radiation force and each photon will add a momentum of $p = h\nu/c$ in each collision. The neutrality of the accreted plasma is sustained by electrostatic forces assuming that particles are not split more than *Debye length* $\lambda_D = r_e/\omega_p$ where ω_p is the angular frequency of the plasma and r_e is

23

the thermal speed of electrons. Then radiation force on an electron will be the sum of total momentum received per second, $F_r = \sigma_T f_v p$, where $\sigma_T = 6.6 \times 10^{-25} \frac{1}{cm^2}$ is the *Thompson cross-section* and f_v is the photon flux. In terms of luminosity, the photon flux can be represented as $f_v = \frac{L}{4\pi r^2}$. By inserting f_v, the radiation force will be equivalent to:

$$F_r = \frac{\sigma_T}{c} \frac{L}{4\pi r^2}. \tag{2.10}$$

The Eddington Luminosity, L_{edd} can be calculated at the point at which these two forces are at balance (i.e. $F_r = F_{gr}$);

$$L_{edd} = \frac{4\pi G M c m_p}{\sigma_T}. \tag{2.11}$$

Re-arranging the known constants of the equation 2.11, L_{edd} will become;

$$L_{edd} \approx 1.26 \times 10^{38} \left(\frac{M}{M_\odot} \right) erg/s \tag{2.12}$$

where $M_\odot$ is the mass of the sun. It should be noted that L_{edd} derived above presume spherical symmetry and stable accretion. The equation 2.11 will be invalid otherwise. For example, if the radiation is beamed to a direction, the spherical symmetry will be broken and equation 2.11 will no longer be of use.

Alfven Radius

As mentioned in chapter 1, neutron stars possess strong magnetic fields which play a crucial role during mass transfer processes. Accretion flow is interrupted by the dipolar component of the magnetic field since it is the most dominant term at large distances. The interruption occurs at the magnetospheric boundary and the trajectory of the plasma either changes towards the polar caps or repelled to infinity ([68]). The radius of the magnetospheric boundary is obtained at the distance where the ram pressure of the infalling plasma matches the magnetic pressure of the NS. The plasma simply have a free fall motion with a speed of $v = \sqrt{\frac{2GM_{ns}}{r}}$, during which it exerts a *ram pressure* upon the magnetic field as;

$$p_{ram} = \rho v^2 = \frac{\dot{m} v}{4\pi r^2} = \left(\frac{GM_{ns}}{8\pi^2} \right)^{1/2} \frac{\dot{m}}{r^{5/2}}. \tag{2.13}$$

In the above calculation, we assumed that accretion is spherically symmetric (i.e. $\dot{m} = 4\pi r^2 \rho v$). On the other hand, the dipolar B-field strength as a function of distance

$B(r)$, can be written in the form of

$$B(r) = B_0 R_{ns}^3 \frac{1}{r^3} \tag{2.14}$$

where R_{ns} is the radius of the NS and B_0 is magnetic field at the surface. Then the corresponding magnetic pressure p_{mag} can be approximated as

$$p_{mag} \approx \frac{B^2}{2\mu_0} \approx \frac{B_0^2 R_{ns}^6}{2\mu_0} \frac{1}{r^6} \tag{2.15}$$

where μ_0 is the permeability of free space. The balance between these pressures is achieved at a distance called *Alfven Radius*. Therefore, matching equations 2.13 and 2.15 will yield;

$$r_A = \left(\frac{2\pi^2 B_0^4 R_{ns}^{12}}{G\mu_0^2 M_{ns} \dot{m}^2} \right)^{1/7}. \tag{2.16}$$

Keeping in mind that dipole moment μ is proportional to $\mu \propto B_0 R^3$, the magnetospheric radius can also be expressed as ([68]; [69]);

$$r_m \approx \eta \left(\frac{\mu^4}{GM_{ns} \dot{m}^2} \right)^{1/7} \approx \eta (GM_{ns})^{-1/7} \mu^{4/7} \dot{m}^{-2/7} \tag{2.17}$$

where η is a dimensionless parameter ranging from 0.5 to 1. For $\eta \approx 0.92$ magnetospheric radius matches with *Alfven Radius*. For an ordinary pulsar with a dipolar magnetic field strength of order $B_0 \sim 10^{12}$ G, Alfven Radius is in the order of $\sim 100 R_{ns}$ for an accretion at Eddington Limit. If $\eta \approx 0.47$, it will be the magnetospheric radius of accretion from a Keplerian disk ([70]). Accretion scenario will differ depending on whether the magnetospheric radius exceeds the co-rotation radius (a radius for which the disk and neutron star rotates at same rate). If $r_m > r_{co}$, the accretion flow may be repelled by the centrifugal forces and results in *propeller effect* ([71]). If $r_m < r_{co}$, the trajectory of the plasma follows the magnetic field lines through the polar caps of NS.

Rayleigh-Taylor instability

Even though sustained with an equivalent pressure, when a more dense fluid (ρ_h) exerts a force on a lighter fluid (ρ_l), there is an instability generated on the interference, known as *The Rayleigh-Taylor instability* (RTI). The most basic example would be a cell containing water on top of air as it is in figure 2.4. The gravitational force will be the origin of the acceleration, thereby water will push the air through ground. And
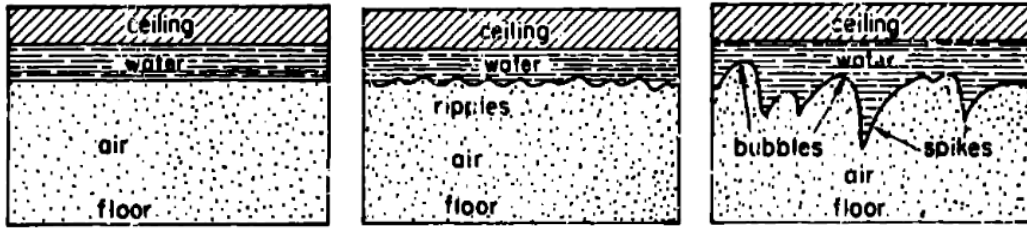
Figure 2.4: Evolution of a Rayleigh-Taylor instability on the interference of water and air combination [72].

the pressure of the air is arranged in such a way that it is equivalent or higher than the value to support the water of given column thickness.

No matter how flat is the surface between water and air is settled, there will be some fluctuations from that surface. That fluctuations will cause ripples on that surface which will initiate the instability. When the ripples start, the fractions of water lying under the average height of the plane will experience less air pressure than required, therefore these fractions will begin to fall through ground and create spike-shapes. Vice versa, the fractions of water which stands above the average level of the surface will be pushed aside because local air pressure on that fraction is higher than needed. This will result in a motion where air will penetrate through water with a shape so called bubble. As the air bubbles move upwards, and the water spikes move downwards, local variations of pressure cannot prevent the instability from growing. The initial irregularities will then increase in magnitude, exponentially at the beginning. Then, the growing instability will yield a turbulence leading to a chaotic mixing of two fluids (See [72] for a review).

In astrophysical context, the force originates from either gravitational or magnetic field of a star and the plasma accumulated at boundaries will be subjected to RTI. In binaries containing a neutron star, the accretion disk will truncate at the magnetospheric boundary. Beyond the boundary, the plasma is accreted either via *i)* funnel streams along field lines (e.g. [73]; [74]) or *ii)* plasma instabilities at the boundary (e.g., [75]; [76]). Hence, RTIs is expected to take place at this boundary since the high-density plasma encounters low-density plasma in the presence of gravity.

Development of the Rayleigh-Taylor instability can be affected by many parame-

26

ters of the accretion disk including, viscosity, compressibility, density distribution, geometry, and many others. For example, *density ratio* (ρ_h/ρ_l) or *Atwood Number* $A = \left(\frac{\rho_h - \rho_l}{\rho_h + \rho_l}\right)$ of the fluids plays a crucial role in the growth of small amplitude fluctuations or perturbations. *Viscosity* inevitably regularizes plasma flow, hence it suppresses the growth rate of the instability. *Compressibility* of the fluids affects the long wavelength perturbations. Stone & Gardiner ([77]) argued that magnitude of B-fields is also important for the instability. Therefore, presumed disk model (and the plasma properties within) also affects RTI development.
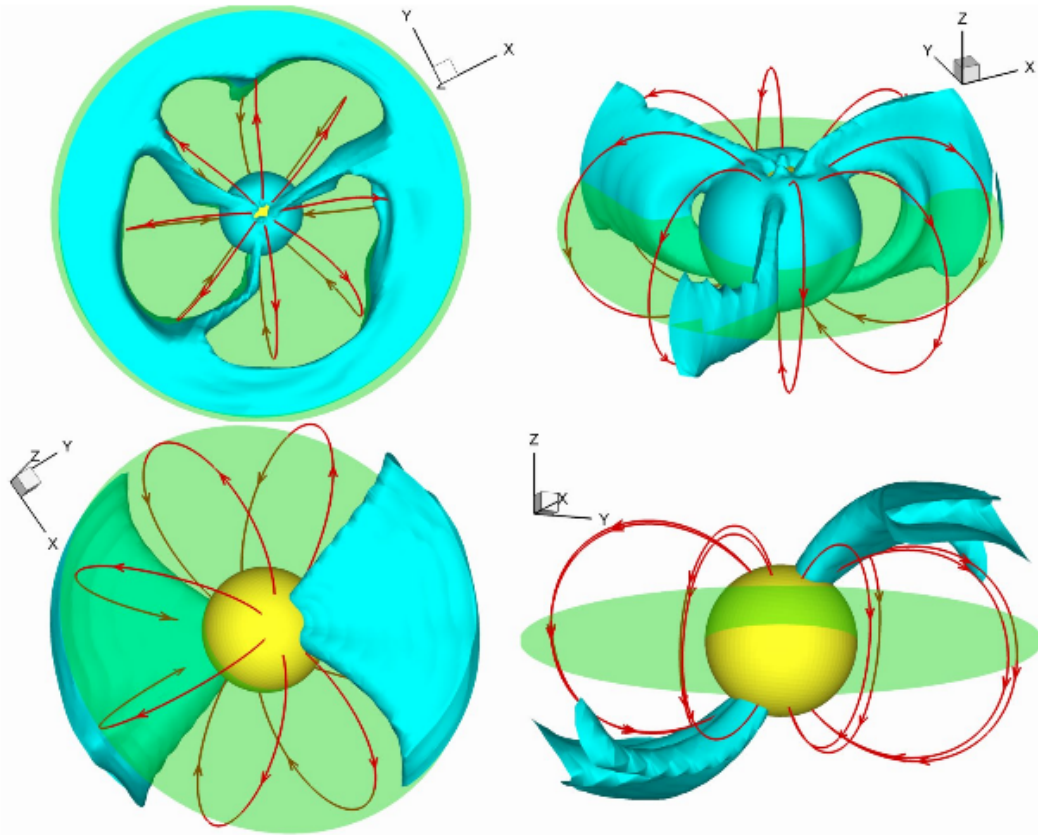
Figure 2.5: A 3D simulation of accretion around a magnetized compact object. Bottom panels represent the flow without instabilities while top panels include the effects of instabilities [78].

Throughout decades, many theoretical and numerical studies are devoted for modeling accretion flow with instabilities (e.g. [75]; [79];[74]; [80]; [77]; [78]). As an example, Kulkarni & Romanova [78] performed 3D modeling of a prototype of RTI

in accretion disks of a magnetized compact object based on α-disk model of [81]. Figure 2.5 displays an illustration of the simulations generated by [78] which distinguish accretion geometry with and without the instabilities.

2.2.2   Disk Accretion
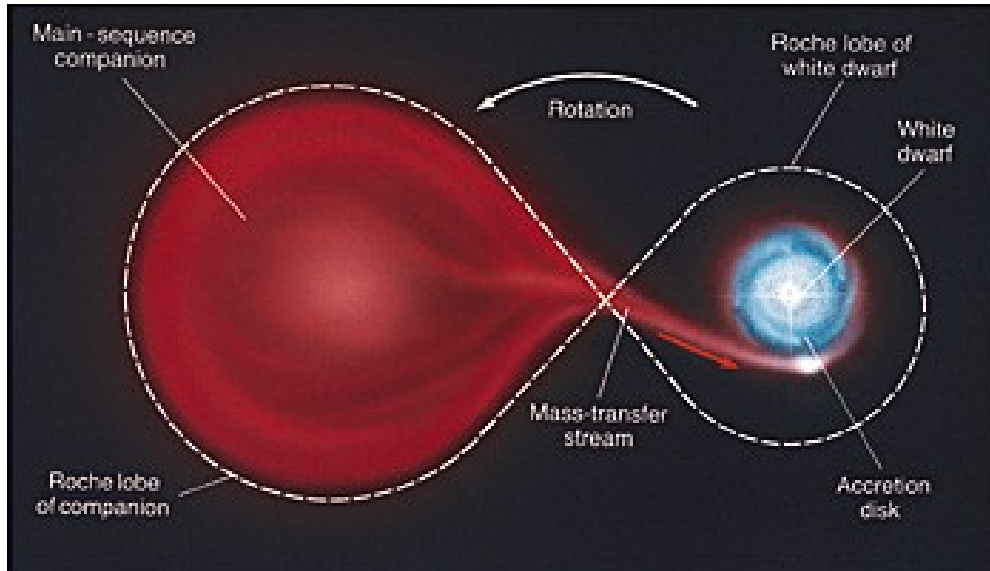
Figure 2.6: Artistic image of accretion via Roche Lobe Overflow. Picture Credit: Pearson Prentice Hall, Inc

The Roche Lobe Overflow constitutes the principal scheme of accretion in LMXBs, however; it is also observed in persistent HMXBs (e.g., [82]).In this scheme, donor star is a late type-star with a weak magnetic field. As the donor star evolves, its radius extends so much that the radius exceeds the Roche Lobe of the donor star. Excess matter in out layers feels the dominance of the gravitational field of the neutron star. Then excess matter flows through the neutron star transpassing the inner Lagrangian point L_1. Since the matter possesses angular momentum, the mass flow will be in spiral form. Eventually, a disk formation occurs if circularization radius ($R_{cir} = \frac{J^2}{GM_{ns}}$, where J is the angular momentum per unit mass) is larger than r_m [83]. The circularization radius marks the distance where disk formation starts. Within the accretion disk, dissipative forces (e.g shock, viscosity) leads to angular momentum loss which results in smaller circularization radii. As it gets closer to the accreting object, the matter revolves at smaller and smaller circularization radii, eventually forming an ac-

28

cretion disk. At the magnetospheric boundary described above, accreted matter feels the dominance of magnetic pressure at radius;

$$r_m \approx \eta \left(\frac{\mu^4}{GM_{ns}\dot{m}^2} \right)^{1/7} \approx \eta(GM_{ns})^{-1/7}\mu^{4/7}\dot{m}^{-2/7} \quad (2.18)$$

It is more convenient to express the equation 2.18 in terms of observable quantity L_x in the form [84];

$$r_m \approx 2.9 \times 10^8 m_x^{1/7} R_6^{-2/7} L_{37}^{-2/7} \mu_{30}^{4/7} cm \quad (2.19)$$

where the converted units are $m_x = M_{ns}/M_\odot$, $R_6 = R_{ns}/(10^6\, cm)$, and $L_{37} = L_x/(10^{37}\, erg/s)$ and $\mu_{30} = \mu/(10^{30} G cm^3)$. Within this boundary, the accretion disk is expected to be truncated since the matter is funneled along the field lines with the dominance of the magnetic strength of the neutron star. When the matter reaches the surface of the neutron star, it will radiate in X-ray energies.
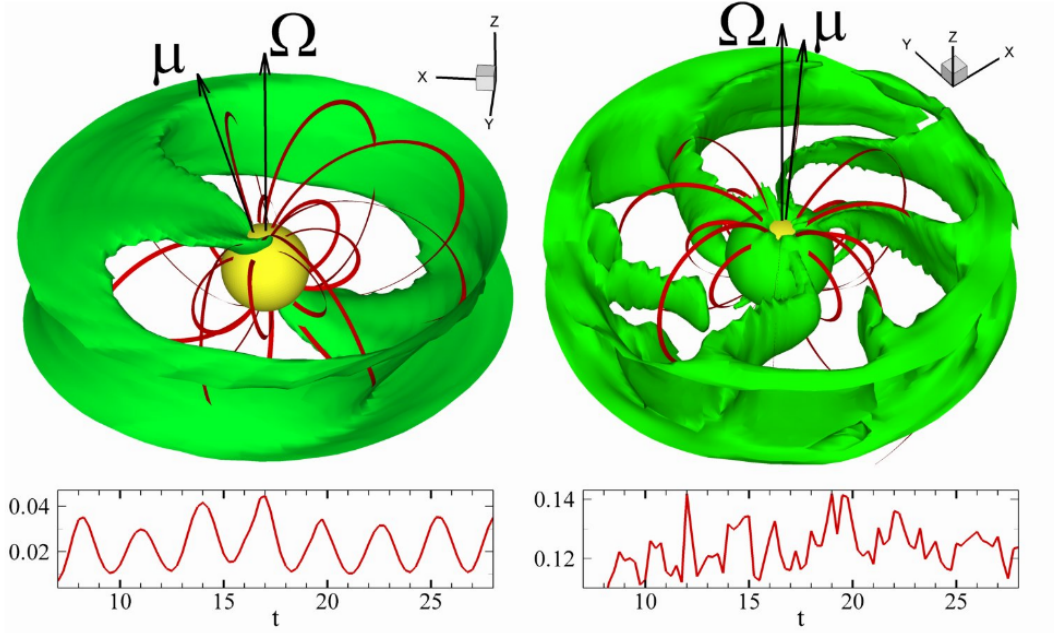
Figure 2.7: Simulation of accretion flow in the case of an oblique rotating neutron star (left) without instabilities and (right) with instabilities. Bottom panels illustrate the corresponding lightcurves from simulations [78].

Now, let us concentrate more on mass accretion onto NS in the presence of a disk. The presence of a disk invokes more complicated problems due to the interaction between the rotating neutron star's magnetosphere and the plasma within the disk.

Moreover, it should also be noted that a NS is an oblique rotator and the angle between the magnetic axis and the disk plane is also crucial (See Figure 2.7). As an example of this situation, magnetic pressure may be modified as [85]

$$p_{mag} = \frac{B^2}{2\mu_0} \approx \frac{\mu^2}{r^6}[1 + 3(sin\alpha\, sin\phi)] \quad (2.20)$$

where α is the angle between magnetic and spin axes. With similar calculations, it can be shown that the resultant magnetic radius will change as a function of azimuthal angle ϕ as ([85]; [86]):

$$r_m(\phi) = 3.2 \times 10^8 \mu_{30}^{4/7} m_x^{-1/7} M_{17}^{-2/7}[1 + 3(sin\alpha\, sin\phi)]^{2/7} cm \quad (2.21)$$

which indicates that the boundary structure is asymmetrical. Throughout the years, many attempts have been made to understand disk and magnetosphere interaction (e.g., [74]; [87]; [88]; [89];[90]; [91]; [92]; [86];[93]). However, due to the strong radial dependence (r^{-6}) of p_{mag}, estimations of r_m stay within the order of Alfven Radius R_A.

The difficulties arise while endeavoring to derive a torque expression at r_m, which includes azimuthal dependence of the B-field, because the field lines at r_m deformed from standard dipole geometry and the plasma instabilities at the boundary should also be taken into account. The torque expression is rather important in the sense that the evolution of the rotational motion of an accreting neutron star is governed with the torque exerted at the magnetospheric boundary.

To achieve a steady accretion at the boundary, the Keplerian velocity of the disk ω_k (at $r = r_m$) must be higher than the angular velocity of the NS (ω_{ns}). Conventionally, this condition is expressed via *fastness parameter* (ω_s) as ([74]);

$$\omega_s = \frac{\omega_{ns}}{\omega_k} < 1. \quad (2.22)$$

The dominance of magnetic field ensures that accreted plasma have a trajectory towards the polar caps. Without taking plasma instabilities into account, the "illuminated" fraction the polar cap to the total area of the NS can be estimated as ([84]);

$$f_{disc} \sim \frac{R_{ns}sin^2\alpha}{4r_m} \quad (2.23)$$

The subscript $disc$ is inserted to emphasize the fact that calculations are held in disc accretion case. Obviously, the equation 2.23 implies that the fraction is less than 1 in

any case. Furthermore, with the r_m approximation in equation 2.19, it can be understood that the polar cap fraction varies for different B-field strength and luminosities, typically ranging within $10^{-1} - 10^{-4}$ ([94]). In the quasi-spherical accretion case, the fraction f_{sh} of polar caps are estimated to be around half of f_{disc}.

In accreting systems, regular long-term angular acceleration episodes are thought be linked with steady state. With plausible values of r_m and the observed pulse frequencies, it is reasonable to regard these sources as slow rotators since the fastness parameter will be far less than 1 ($\omega_s << 1$). Using this approach for a prograde disk, the rate of angular momentum delivered at the boundary r_m can be estimated as;

$$
\begin{aligned}
\dot{L} &\approx \dot{m} r_m^2 \omega_k(r_m) \\
&\approx \dot{m} \left(G M_{ns} r_m \right)^{1/2} \\
&\approx \dot{m} \left(G M_{ns} \right)^{1/2} [\eta(GM_{ns})^{-1/7} \mu^{4/7} \dot{m}^{-2/7}]^{1/2} \\
&\approx \eta^{1/2}(GM_{ns})^{3/7} \mu^{2/7} \dot{m}^{6/7} \\
&\approx \eta^{1/2}(GM_{ns})^{3/7} \mu^{2/7} \left[\frac{R_{ns} L_{acc}}{GM_{ns}} \right]^{6/7} \\
&\approx \eta^{1/2}(GM_{ns})^{-3/7} \mu^{2/7} R_{ns}^{6/7} L_{acc}^{6/7}
\end{aligned}
\tag{2.24}
$$

where the mass accretion rate $\dot{m}$ is converted to the luminosity via equation 2.8 and the Keplerian frequency is simply $\omega_k = \sqrt{\frac{GM}{r_m^3}}$. In addition, we used equation 2.18 to describe the magnetospheric radius. Then the rotational acceleration can be rearranged in terms of normalized parameters as;

$$
\dot{\nu} \simeq 2.7 \times 10^{-12} m_x^{-3/7} R_6^{6/7} L_{37}^{6/7} \mu_{30}^{2/7} I_{45}^{-1} \ Hz/s
\tag{2.25}
$$

where I_{45} is the moment of inertia of NS in units of 10^{45} g cm^2. Since the rest of the parameters are approximately unitary, the above equation implies that the spin-up rate and luminosity are correlated (with an exponent of 6/7). This correlation is observed for many sources, especially in the transient systems (e.g. [95]), however the exponent seems to slightly deviate from 6/7.

The more angular momentum the neutron star will receive, the quicker it will rotate. Experiencing the torque for a long time, the neutron star will rotate so rapidly that the fastness parameter will approach to unity (i.e. $\omega_s \sim 1$). Eventually, spin period advances through an equilibrium as the material at the magnetospheric radius starts

to co-rotate with the neutron star. The equilibrium state can be described as [94];

$$P_{eq} \approx 3m_x^{-3/7} R_6^{-3/7} L_{37}^{3/7} \mu_{30}^{6/7} \text{ s} \qquad (2.26)$$

Beyond that rough description of the accretion scheme above, many studies have been made to underpin the physics behind the accretion process. Throughout the years, the sophisticated models have been built which takes different physical properties of the disk into account (e.g., [74]; [87]; [88]; [89];[90]; [91]; [92]; [86];[93]). Below, some of the commonly used examples of disk models will be described.
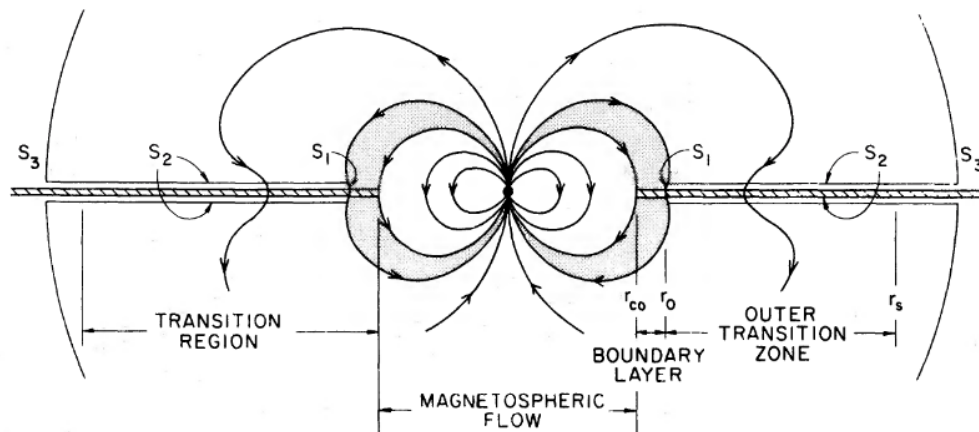
Figure 2.8: Gosh & Lamb Model [74].

In 1979, Ghosh & Lamb developed a model where the accretion disk is widely invaded by the B-field lines (See Figure 2.8). In their model, the invasion is justified by the plasma instabilities and magnetic reconnection. The B-field lines wind up by the differential rotation the accretion disk and the neutron star. The winding up of the field lines is counterbalanced with dissipation. They examined the results of the model on several sources. They showed that if the disk and the neutron star rotate at the same direction both spin-up and spin-down torques are possible. The switch between spin-up and spin-down episodes can be obtained depending on the luminosity. In order to deal with field wind up, Ghosh & Lamb model requires colossal magnetic diffusivity.

Shu et al. [87] studied accretion from an imperfectly conducting disk. In this model, the field lines are not allowed to penetrate the accretion disk except magnetospheric

boundary region. Their results indicate that a "magneto-centrifugally driven wind" may occur at this regime (See Figure 2.9). This model have exquisite applications for collimated outflows (e.g jet outflows in Active Galactic Nuclei (AGNs)).
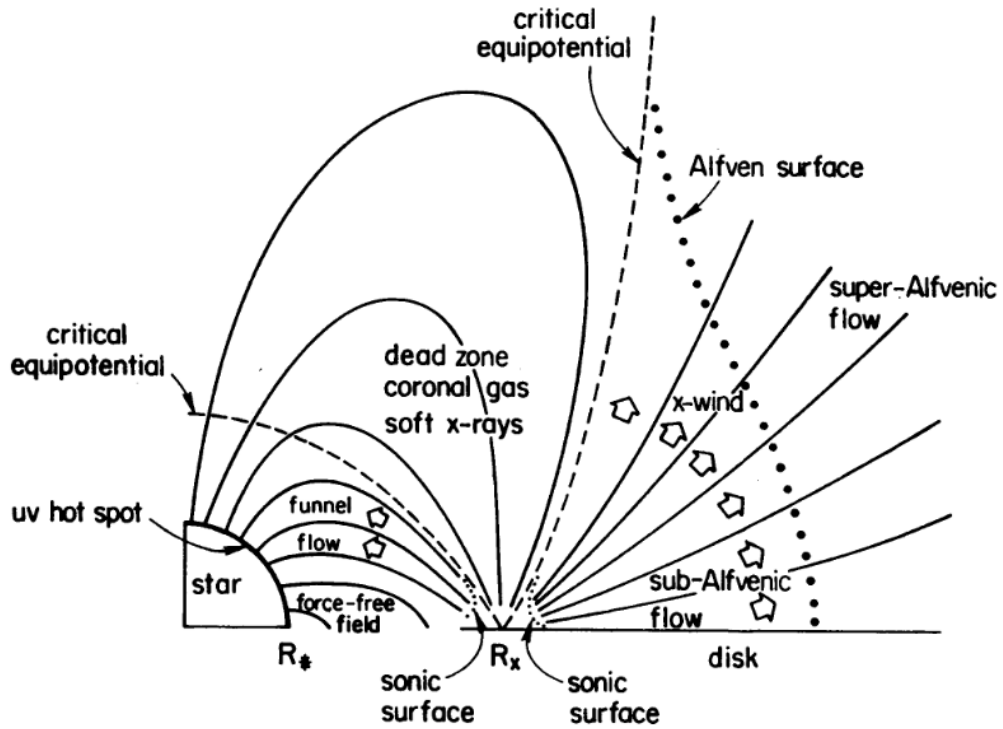
Figure 2.9: Accretion Model of Shu et al. [87].

Lovelace et al. [89] formulated the case of accretion onto a magnetized object where the disk and B-field axis coincide. They suggested that the field lines wind up for a long range of distance due to differential rotation between the NS and the disk (See Figure 2.10). They argue that open field lines around the disk regime yield to "magnetically driven outflows" and they investigated the structural changes in the disk due to the influence of the outflows. The outflows may even extend to a radius where disk rotation is maximum (defined as r_{to}). If the radius r_{to} is close to the co-rotation radius $r_{co} = \left(\frac{GM_{ns}}{\omega_{ns}}\right)^{1/3}$, the neutron star may switch between spin-up and spin-down states depending on several parameters such as variations of mass accretion rate.
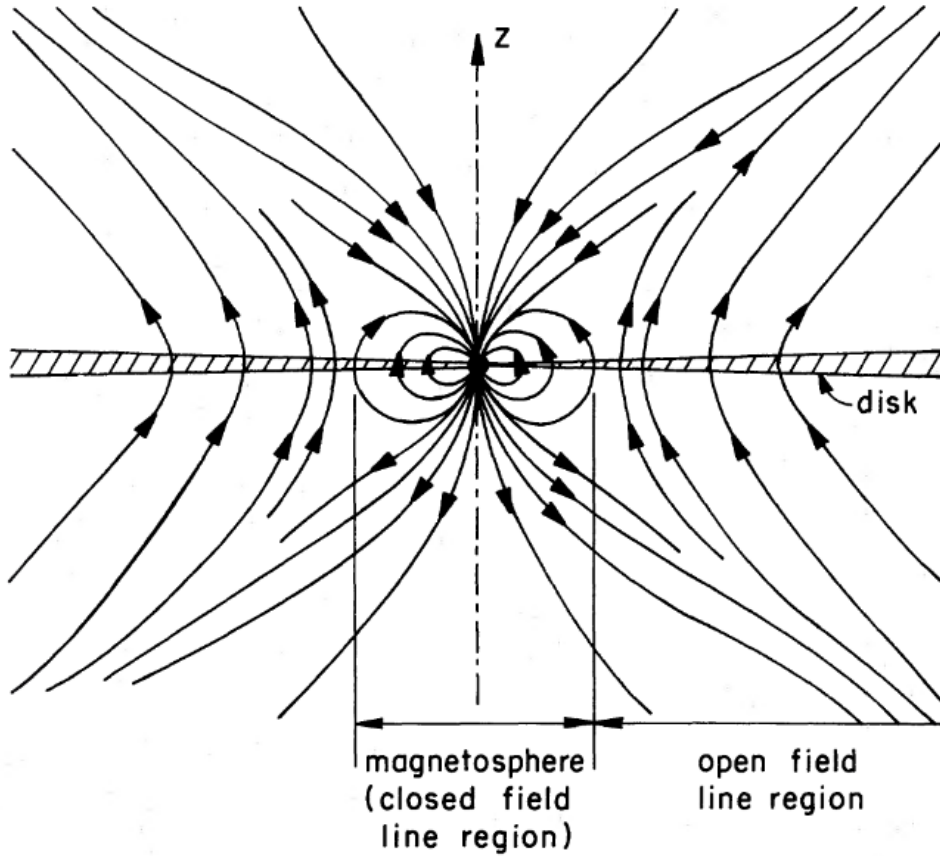
Figure 2.10: Accretion model of Lovelace et al. [89]

2.2.3 Wind Accretion

In the case of HMXBs, the donor star is very massive and commonly not in super-giant phase. Although, it is observed in several cases (e.g., [82]), Roche Lobe Over-flow is very uncommon for such systems. The less massive stars produce weak stellar winds, however in the case of massive stars wind becomes very intense. Hence, the main accretion scenario of HMXBs is initiated by the capture of stellar wind of the massive companion (see figure 2.11 credit:[96]). The wind accretion scenario was proposed prior to the discovery of X-ray binary systems by [97]. The foremost notion about wind accretion may occur as an inefficient process, however; stellar winds of massive stars supply a vast amount of matter flux[3]. The neutron star may only cap-ture a small fraction of this spherically ejected wind, but still it can empower high luminosities.

---

[3] In O-B type stars, mass loss rate due to the wind may even reach to $10^{-4} M_{\odot}$ per year.
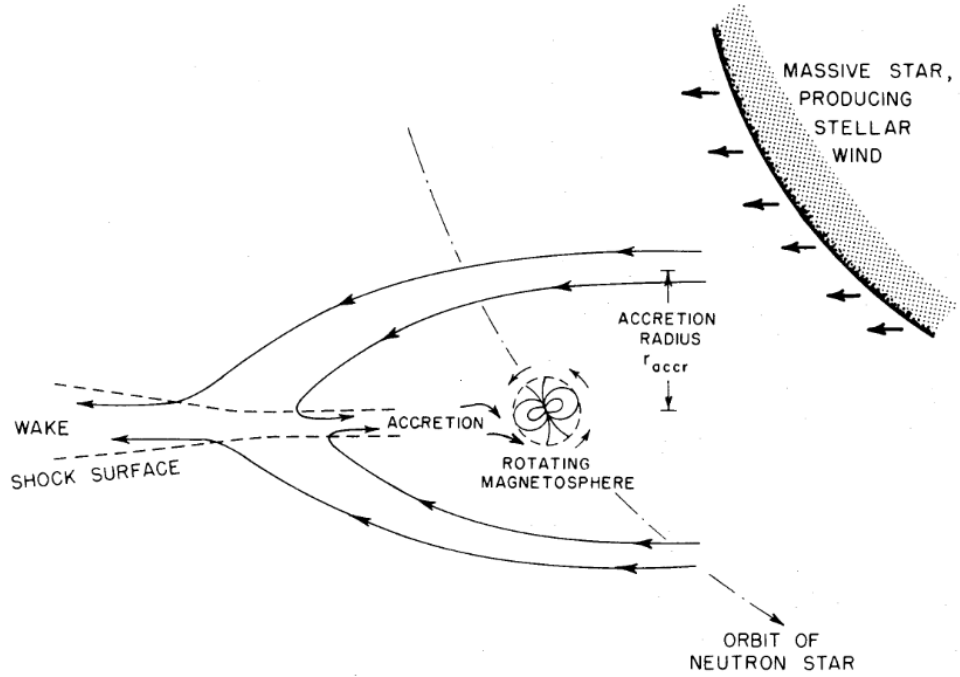
Figure 2.11: Wind accretion scheme and accretion streams towards a neutron star.

In order for this scenario to take place, the wind velocity (ν_w) must be larger than neutron star's orbital velocity (ν_{orbit}). In HMXBs, the crude values of the terminal wind velocity (ν_∞) and orbit velocities are in the order of $\nu_\infty \sim 1000$ km/s and $\nu_{orbit} \sim 100$ km/s. The escaping plasma starts with very small velocities at photosphere $\nu_0 < 1$ km/s but it is accelerated to very high radial speeds as the distance from the donor star increases and reaches to the terminal velocity at very large distances (as $r \to \infty, \nu_0 \approx \nu_\infty$). The wind velocity as a function of distance r can be approximated via $\beta - law$ [98]:

$$\nu_w = \nu_\infty \left[1 - \frac{R_0}{r} \right]^\beta \tag{2.27}$$

where $R_0 = R_s[1 - (\nu_0/\nu_\infty)^{1/\beta}]$ and R_s is the companion star's radius. Index parameter β is introduced to describe how steep the velocity changes as a function of distance. For example, Index parameters β of hot stars are found to be around 0.8, indicating that the wind achieves 80% of its terminal velocity roughly at $3R_s$ above stellar surface [98]. The massive star wind will be in spherical form but still some of the material in wind is directed towards the compact star. The compact star will

35

accrete this plasma if;

$$\frac{GMm}{r} \geq \frac{1}{2}m\left(\nu_w^2 + \nu_{orbit}^2\right) \qquad (2.28)$$

In the standard scheme [99], stellar wind moving with supersonic speeds will experience a shock when it arrives at a certain distance (arising from the equality condition of equation 2.28). Passing this boundary, the matter will freely fall towards the neutron star and will be accreted on the surface (see, e.g. [94] and references therein). The distance of the shock r_{acc} after which neutron star can effectively deflect the wind towards itself can be approximated as ([97], or see [100] for a more recent review);

$$r_{acc} \approx \frac{2GM_{ns}}{\nu_w^2 + \nu_{orbit}^2}. \qquad (2.29)$$

The radius calculated above is also referred as *Bondi radius* honoring the work of Bondi & Hoyle [97]. For a neutron star with $1.4M_\odot$ and typical wind velocities stated above, the order of magnitude of r_{acc} will be around 10^7 kilometers. In the most simple case, the wind can be assumed to have spherically symmetric form. With this assumption, the mass loss rate of the donor star $\dot{M}_w$ as a function of distance can be described as;

$$\dot{M}_w = 4\pi r^2 \nu_w \, \rho_w(r) \qquad (2.30)$$

where $\rho_w(r)$ is the density of the wind. The neutron star can only accrete the mass reaching to the cylindrical region defined by R_{acc} at a rate;

$$\dot{M}_{acc} = \pi R_{acc}^2 \, \rho_w(r) \, \nu_w \qquad (2.31)$$

The ratio of these two equations defines the fraction of the mass that can effectively be captured by the neutron star as [44];

$$\frac{\dot{M}_{acc}}{\dot{M}_w} \approx \frac{1}{4}\left[\frac{R_{acc}}{a}\right]^2 \approx 10^{-5}\left[\frac{M_{ns}}{M_\odot}\right]^2 \nu_8^{-4} a_{10}^{-2} \qquad (2.32)$$

where the distance r from the donor star to the bow-shock distance R_{acc} is approximated as the binary separation a. With this accretion rate, total X-ray luminosity L_x generated will be equal to;

$$L_x = \frac{GM_{ns}\dot{M}_{acc}}{R_{ns}}. \qquad (2.33)$$

But still, it is important to note that the accreting source is magnetized and therefore there will be the second boundary due to magnetic pressure. The relative distance of

36

this boundary to the gravitational capture radius is also substantial for the accretion process.

If the gravitational capture radius r_{acc} is larger than the magnetospheric radius r_m, the ram pressure of the incoming mass can be counterbalanced with magnetic pressure. Thus, the flow will cease when;

$$\frac{B^2(r_m)}{8\pi} = \rho(r_m)\,\nu_w(r_m) \tag{2.34}$$

where (r_m) represents the values of the given parameter at the distance r_m. Similar to the assumptions in the derivation of Alfven Radius, the density of the wind at r_m can be related by;

$$\rho(r_m) \sim \frac{\dot{M}_{acc}}{4\pi r_m^2 \nu_w(r_m)}. \tag{2.35}$$

where the velocity of the free-falling mass is $\nu_w(r_m) = (GM_{ns}/r_m)^{1/2}$. It should be noted that mass loss rate $\dot{M}_{acc}$ is related to the $\dot{M}_w$ by the equation [84];

$$\frac{\dot{M}_{acc}}{\dot{M}_w} \approx \frac{1}{4}\left[\frac{R_{acc}}{a}\right]^2 \approx 10^{-5}\left[\frac{M_{ns}}{M_\odot}\right]^2 \nu_8^{-4} a_{10}^{-2} \tag{2.36}$$

where ν_8 is the wind velocity in units of 10^8 cm/s and a is the orbital separation distance in units of 10^{10} cm. Using this information, the magnetospheric radius can be obtained as;

$$r_m = 10^{10}\left[\frac{M_{ns}}{M_\odot}\right]^{-5/7} \dot{M}_{-6}^{-2/7} \nu_8^{8/7} a_{10}^{4/7} \mu_{33}^{4/7} cm, \tag{2.37}$$

where $\dot{M}_{-6}$ is the mass loss rate in terms of $10^{-6} M_\odot$ per year, the magnetic field strength B is approximated as $B \propto \mu/r_m^3$ and $\mu_{33} = \mu/10^{33}$ G cm^3.

On the other hand, if $r_m < r_{acc}$, then gravitational force becomes unimportant. In this case (again with a spherical symmetric wind assumption), the density at the boundary can be estimated as ([101];[49]):

$$\rho(r_m) \sim \frac{\dot{M}_w}{4\pi a^2 \nu_w}. \tag{2.38}$$

Using the boundary condition described by equation 2.34 and the wind density in the form of equation 2.38, slightly altered radius r_m can be obtained as;

$$r_m = 10^{10}\dot{M}_{-6}^{-1/6} \nu_8^{-1/6} a_{10}^{1/3} \mu_{33}^{1/3} cm, \tag{2.39}$$

The classical wind accretion scheme described above is valid only for supersonic wind flow [76]. If the accreting NS sustains sufficient X-ray radiation, Comptonization will ensure the rapid cooling of the plasma. Then the wind velocity turns out to be supersonic and shock formation takes place above the magnetosphere [102]. With the condition above, the plasma penetrates the shock regime and enters to neutron star's magnetosphere via *Rayleigh-Taylor instabilities* [76], finally falls freely towards the NS. The frequency derivative of the neutron star switches sign (spin up/down) with the influence of the torque exerted by the accreted plasma.
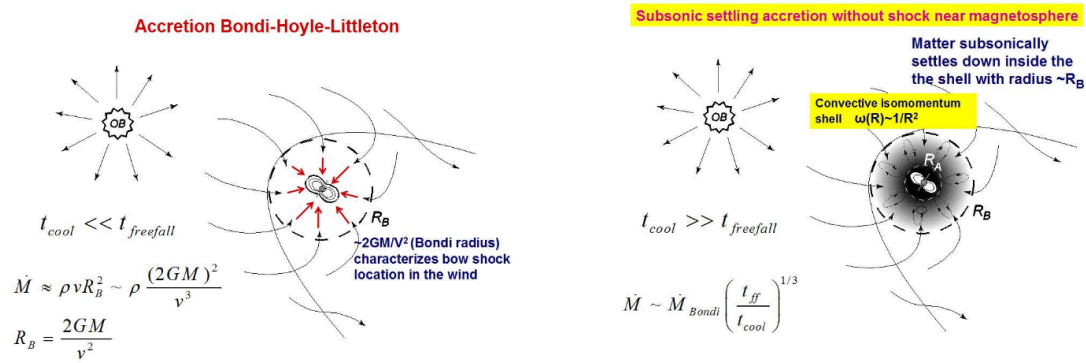
Figure 2.12: Wind accretion scheme and accretion streams towards a neutron star. Left: standard scenario, Right: Quasi-spherical accretion settling [103].

The second possibility is that, if the X-ray flux is insufficient (especially when $L_x < 10^{36}$ erg/s), the Comptonization process will not be able to effectively cool down the plasma [104]. In this case, the wind appears to have subsonic speeds and will settle around magnetosphere [104]. The hot plasma will pile up at the boundary and form an envelope, called *quasi-spherical accretion shell*, around the neutron star ([101]; [104], also see Figure 2.12). Within the shell, convective motions commence because of the super-adiabatic temperature gradient [104]. For sufficiently low wind speeds ($\nu_w < 80$ km/s), the shock vanishes and photoionization becomes significant. In such a case, accretion starts at a slightly modified Bondi radius;

$$R_B^* = \frac{2GM}{c_s^2} \tag{2.40}$$

where c_s is the speed of sound within the shell. Rotation of the neutron star is influenced by the shell-magnetosphere interaction.

Over the years, many studies revealed that *Ab inito* model presented above is oversimplified and detailed calculations should also deal with the inhomogeneous structure of stellar winds because the more dense regions, called *clumps*, within the wind yields rapid variations in the X-ray luminosities (e.g. [105]).

CHAPTER 3

DATA ANALYSIS

3.1 Timing Analysis

The timing analysis refers to methodology of searching and examining temporal structures within the data set. This analysis is one of the most fundamental approaches for deducing the frequency evolution of pulsars from which an "understanding" of physical conditions of the object is established. It should be noted that the time series of the light curve used for pulse timing analysis must be converted to solar system barycenter in order to avoid unnecessary Doppler delays caused by the motion of the observatory on which the data is taken.

In order to construct the frequency evolution of pulsating sources, the first step of the timing analysis often starts with *Epoch Folding Technique* [106]. In this technique, a light curve of time span T_{obs} is "folded" and summed over the periodicity P_0 . In other words, assuming that the initial guess P_0 is expected to split into n number of intervals (or phase bins), then the light curve will be divided into time segments of equal duration $\Delta t_i = P_0/n$, where the subscript i is introduced as the index of each phase bin (ranges from 1 to n). The count rates in the "modulus segments" are summed over to obtain the normalized count rates C_i within each bin i:

$$\begin{aligned} C_i &= \frac{1}{M}\big(C_{\Delta t_i} + C_{\Delta t_{i+n}} + C_{\Delta t_{i+2n}} + ...\big) \\ &= \frac{1}{M}\sum_{j=0}^{M-1} C_{\Delta t_{i+jn}} \end{aligned} \tag{3.1}$$

where C_{t_i} represents the total count rates in the time segment Δt_i. Obviously, the summation is limited by the fact that the maximum of $M = T_{obs}/P_s$ number of cycles can be achieved with the given data length. In order to illustrate an example
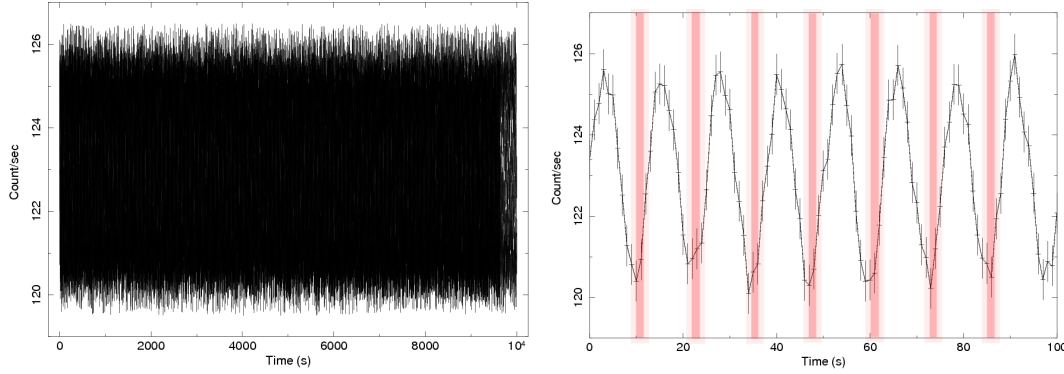
Figure 3.1: *Left Panel:* The simulated light curve. *Right Panel:* The first 100 seconds of the simulated light curve. The light curve is zoomed for a better visualization of periodic count rate modulations. The shaded regions demonstrate the modulus time segments Δt_{1+jn} in which the count rates are summed and averaged to create the phase bin C_1.

for this process, a light curve is simulated for an arbitrary period (see Figure 3.1). The simulated series have a total duration of $\approx 10000s$ and average count rate of ~ 123 counts/sec. The fabricated pulsations of the light curve is approximately ~ 12.5 s. Thus, within the light curve, $10000/12.5 = 800$ pulse cycles are present. During epoch folding, count rates within each time interval Δt_i (e.g. the shaded regions of Figure 3.1 right panel) are summed over to obtain C_i corresponding to the phase index i.

The histogram produced for C_i vs i is called *pulse profile* if the initially given spin period is correct[1]. Figure 3.3 demonstrates the pulse profile with 10 phase bins produced from the simulated light curve. Otherwise, incorrect periodicities will yield co-addition of incorrect phase bins, eventually smearing out the real pulse profile. Moreover, if the periodicity guess of P_0 remotely disagree with the actual period of pulsar P_s, it may even lead to a constant histogram. In this aspect, the level of the quality of the profile can be tested via χ^2 test;

$$\chi^2 = \sum_{i=1}^{n} \frac{(C_i - \bar{C})^2}{\sigma_i^2} \tag{3.2}$$

where $\bar{C}$ is the average count rate of the profile and σ_i is the uncertainty of the count

---

[1] Actual pulse phase should be calculated by i/n and pulse profiles must be drawn accordingly, nevertheless, profile structure stays the same
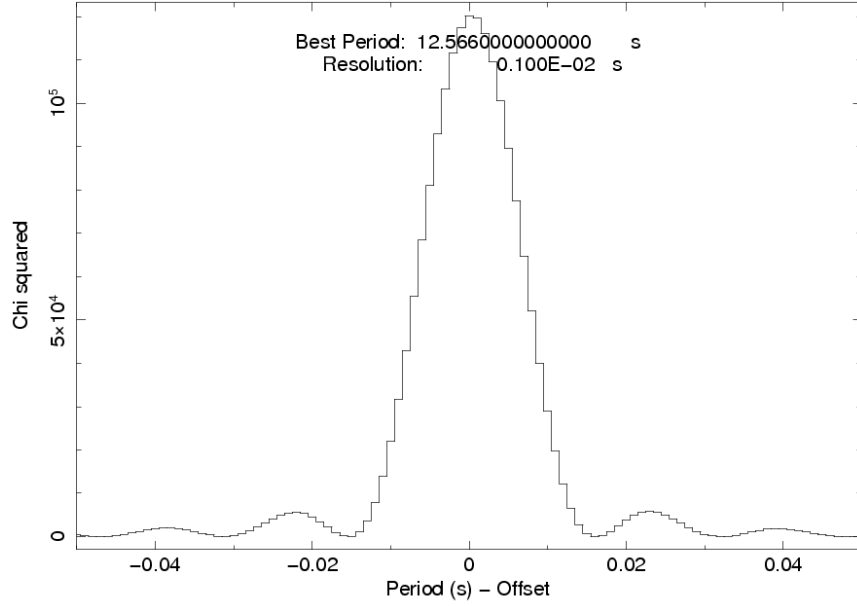
Figure 3.2: An example periodogram generated from the simulated light curve. The χ^2 distribution of the possible periodicities peaks at 12.566s.

rate in the bin C_i. Thus, provided that P_0 is not far away from the actual value P_s, the correct periodicity can be interpreted by examining a distribution of χ^2 statistics for different nearby trial periods. The χ^2 distribution of these periods is also called *periodogram*. As described above, if the trial period vastly differs from the actual value, it can create constant histogram matching with $\bar{C}$ which yields a zero χ^2 value. If the trial period is actually the correct periodicity, then resultant pulse profile will give the highest χ^2 value. The finiteness of a real data can not grant enough "smearing out" effect to completely wipe the pulse profile generated for nearby trial periods. Therefore, nearby periods will also permit χ^2 values which will decrease as the trial period deviate further from P_s. For a clear signal, the periodogram resembles to a Gaussian shape, peaking at the correct period P_s. Figure 3.2 presents an example of a periodogram generated from the simulated light curve. But as the signal to noise ratio (S/N) decreases, the periodogram generates more complicated shapes. With this method, the uncertainty in the measured period will be;

$$\Delta P \approx \frac{P^2}{T_{obs}} \tag{3.3}$$

For example, using values of a typical observational exposure around ~ 10000 seconds and pulsations of ~ 12.5 seconds, this technique can measure the period with

43
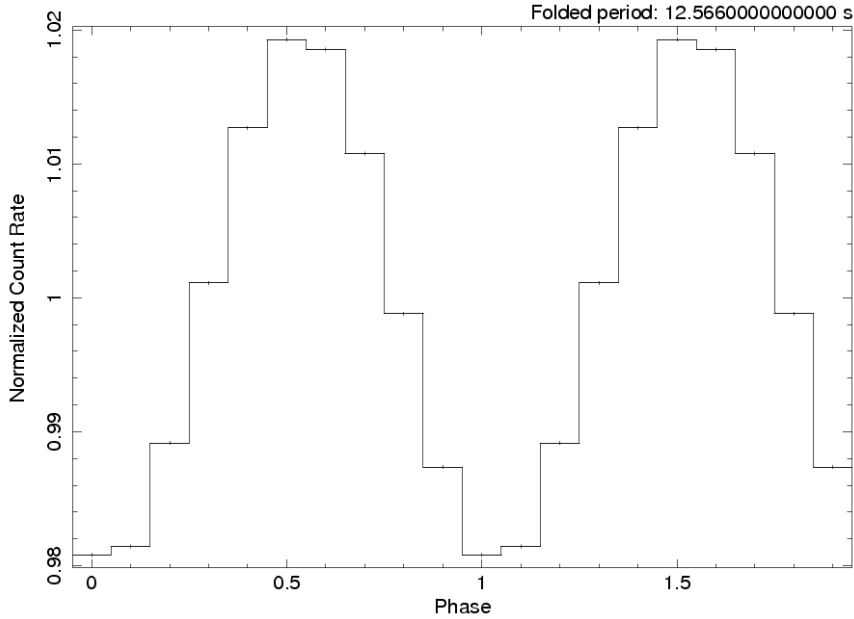
Figure 3.3: An example pulse profile with 10 phase bins generated from the simulated light curve. The light curve is folded over the best period (12.566 s) obtained from the periodogram. The shaded time intervals of the Figure 3.1 corresponds to phase bin 0.1 of this pulse profile.

a 0.125 % uncertainty. This uncertainty (of the order of $\sim 10^{-2}$) does not allow to measure the variations (both systematic and random) of pulsar's period[2].

In order to achieve a better accuracy, epoch folding of consecutive observations of the same source should also be taken into account. With this motivation, a subsequent methodology of *pulse timing* is introduced ([107]; [108]). In this method, a pulse profile is generated by epoch folding for every single observation. Among those profiles, one of them is assigned as a template profile that acts as a reference to measure how much an individual profile is shifted. The decision of determining a template profile is based on the χ^2 test: the profile with a maximum χ^2 value is designated as the template. Then it is mathematically represented with its harmonics as [109];

$$g(\phi) = G_0 + \sum_{i=1}^{n} G_i \, cosi(\phi - \phi_i). \tag{3.4}$$

where ϕ_i denotes the individual phase bin with index i. Assuming that the individual pulse profiles generated for rest of the observations are stable (i.e. pulse profile shape

---

[2] Even for the magnetars, which are the fastest spinning down sources, $\dot{P} \sim 10^{-10}$ s/s

is not changing from one observation to the other), they can be regarded as rescaled and phase-shifted versions of the template. Thus, the individual profiles are again imitated with harmonic functions as;

$$f(\phi) = F_0 + \sum_{i=1}^{n} F_i \, cosi(\phi - \phi_i + \Delta\phi_i) \tag{3.5}$$

In order to comprehend how much phase-shift occurred between the individual and template profile, their *cross-correlation* is evaluated. The cross-correlation produces (by definition) values ranging between 0.5 to -0.5 on the phase space, which becomes larger as two profiles get more aligned, reaching to a maximum when perfectly aligned. Then, the location of the maxima of the correlation function can be understood as the phase-shift $\Delta\phi$ value between the cross-correlated profiles which can be obtained via [109]:

$$\Delta\phi = \frac{\sum_{i=1}^{n} iF_iG_i \, sini\Delta\phi_i}{\sum_{i=1}^{n} i^2 F_iG_i \, cosi\Delta\phi_i} \tag{3.6}$$

In fact, using the relation above the arrival times of pulses (pulse TOAs) are retrieved since each of the individual pulse profile "arrives" at the time of the epoch-folded observation with a phase-shift $\Delta\phi$. Even though , $\Delta\phi$ has no sub-index to denote different observations, it should be understood that each pulse arrives with different phase, therefore $\Delta\phi$ values of each observation should in principle must be different. Then, calculated TOA series can be modeled with a Taylor Series expansion to resolve pulsar's rotational phase as a function time:

$$\phi(t) = \phi_0 + \nu_0(t - t_0) + \frac{1}{2}\dot{\nu}(t - t_0)^2 + .. \tag{3.7}$$

where t_0 is the start time of epoch folding, ν_0 and $\dot{\nu} = \frac{d\nu}{dt}$ are the pulsar's spin frequency and its derivative, respectively. Fitting this model to the real TOAs results in solving the timing parameters such as ν, $\dot{\nu}$ etc. The above expression is expanded upto a quadratic term which means that a pulsar's rotation is expected to regularly spin-up or spin-down. If the pulsar exhibits more complex behaviour, the equation 3.7 should be modified accordingly. For example, if the pulsar appears in a binary system, the pulse TOAs will be observed with Doppler delays due to orbital motion. Hence, a corresponding term, $\Delta\phi_{orb}(t)$, should be introduced. Furthermore, when the pulsar exhibits a glitching behaviour (i.e. a sudden jump in rotational period), then a $\delta\phi_{glitch}$ should be added. Furthermore, the expression 3.7 can be expanded for higher

order terms to deal with high-order spin-frequency changes if necessary (e.g. $\ddot{\nu}, \dddot{\nu}$, ... etc.). In this thesis, case-dependent modifications of expression 3.7 are utilized for particular sources. For example, the frequency evolution of X Per requires high-order polynomial modeling along with binary modulations. In case of SXP 1062, a further modification involves $\delta\phi_{glitch}$.

After building pulse TOA series, the pulse frequency history can be obtained by fitting a linear model $\delta\phi = \delta\nu(t - t_0)$ to the consecutive pulse TOAs. Since the frequency is actually the derivative of phase ($\nu = d\phi/dt$), the slope of the model will yield the pulse frequency estimation $\nu_0 + \delta\nu$ at the mid-time between the fitted pulse TOAs.

Pulse timing methodology offers an higher accuracy while specifying the timing parameters because it affirms a further phase-connection between separated observations. Although, there are specific softwares devoted to pulse timing (for example *TEMPO* [110]), in this thesis, all the analysis are conducted via C-based pulse timing code developed by our astrophysics group[3].

3.2 Noise Strength Analysis

Pulse timing delivers the timing characteristics of a pulsar as long as they are modeled with physically compellable pattern. In an ideal case, a model that totally accounts for the physics behind the rotational motion (and orbital motion) ought to yield zero residuals. Although pulsars are mostly stable rotators, they often exhibit timing irregularities that are randomly fluctuating over time. Therefore, besides established model for spin frequency series of a pulsar, there will still be small unmodeled fluctuations over the model which are called *timing noise*. These random fluctuations were firstly realized as "random walks" in spin frequency measurements in optical band for Crab pulsar's rotation [111]. Later studies unveiled the analysis-frequency-dependent nature of the noise processes in many pulsars, in other words, the timing noise amplitude exhibit disperse varieties on different time spans (e.g. [112]) which is referred to as *red noise*. In this context, the *analysis frequency* refers to $f = 1/T$ inverse of the noise analysis time-scale T, not to the pulsar's spin. Hence, it is often renamed as

---

[3] With the efforts of Prof. Dr. Altan Baykal, Prof.Dr. Sıtkı Çağdaş İnam, Burçin İçdem, Danjela Serim and Muhammed Mirac Serim

"analysis frequency" to avoid confusion.

The timing noise is identified as random walks not only in spin frequency but also in phase and frequency derivative which scales with analysis frequency as $f^{-\alpha}$ [112]. The exponent $\alpha = 1, 2, 3$ resolves the random walks on phase, spin frequency and spin frequency derivative, respectively. Together with the random walk phenomenon, the propagation of discrete small-amplitude jumps of the timing parameters is required ([113]; [114]). There are several distinct methodologies that define the timing noise amplitude in different ways (e.g Δ_8 parameter [115], σ_z parameter [116], rms value [113]; [114]) but all of them generates comparable outcomes. In this thesis, the measure of the timing noise strength is initiated with the mean-squared summation $< \sigma_R^2(m, T) >$ of the residuals as suggested by [113]; [114]. Clearly, there can be distinct set of residuals depending on both the physical model subtracted prior to extraction of residuals (which is a polynomial of degree m that represents pulsar rotation: see equation 3.7) and the residual extraction time scale T. Thus, the mean-squared value $< \sigma_R^2(m, T) >$ will alter accordingly. For example, removal of a second order polynomial ($m = 2$ in equation 3.7) results in inspection of residuals with constant spin-down trend removed. Associated set of residuals can also be generated from spin frequency series if $m = 1$ is used since the corresponding equation would be $\nu(t) = \nu_0 + \dot{\nu}(t - t_0)$.

It should be noted that a white noise on some timing parameter may imply a red noise in an upper set of parameters. For example, when a white noise on spin frequency derivative is observed, it will elevate an analysis frequency dependent noise on spin frequency and phase because each parameter is connected with one step further integral over time. Thus, the red noise order ($r = 1, 2, 3$) is introduced to describe the order of integration from the initial white noise producing timing parameter. Then, for a given set of residuals, time dependent noise strength S_r of order r is approximated via [117]:

$$S_r = \frac{1}{T^{2r-1}} \frac{< \sigma_R^2(m, T) >}{< \sigma_R^2(m, 1) >_u} \tag{3.8}$$

where $< \sigma_R^2(m, 1) >_u$ is introduced as a normalization coefficient for unit time span ($T = 1$). This normalization should be arranged in such a way that it should yield a unit noise strength $S_r = 1$. This can be achieved by two separate methods: i) by calculating the mean square value of a simulated white noise series that fabricates

47

unit noise strength on unit time [118] ii) by direct evaluation mathematically [117].

In order to perceive time dependent nature of the noise process, the noise strength calculations should be re-iterated for the residuals set for different time scales. For example, if the data is split to halves (T/2), then two different $S_r(t = T/2)$ values are evaluated for each segment and logarithmically rebinned to obtain a power estimate on the time scale $T/2$. In general, the residuals are divided for sub-segments of $T/2, T/4, T/8, ...$ as small as the data sampling allows and the power estimate procedure is repeated for each case. Then, a histogram of power estimates versus corresponding analysis frequency is built to investigate the time dependent nature of the noise process. This histogram is also referred to as *power density spectrum*.

The power density spectrum assists to distinguish the dominant noise processes on different analysis frequency ranges. For instance, Alpar et al. [119] argued that power estimates at the highest analysis frequencies ($T < 1$ day) are characterized by vortex pining regions and power estimates at the lowest analysis frequencies ($T > 2000$ days) depicts pure unpinning regions. Cheng [120] suggested that micro-glitches may initiate magnetoshperic variations which produce a red noise component at low analysis frequencies in return.

CHAPTER 4

SWIFT J0513.4-6547

This Chapter presents the timing properties of SWIFT J0513.4–6547 through its observations with RXTE and Swift during 2009 and 2014 outbursts. This work confirms the circular orbit trajectory of the pulsar provided by [121] and investigates the frequency evolution of the source. The magnetic field estimation is conducted assuming that the source is in propeller stage during the quiescent episode. The main article "*RXTE & Swift Observations of SWIFT J0513.4–6547*" is published in MNRAS [122]. The article provides a more complete picture of the source properties by offering further explanations to both the spectral properties and energy-dependent pulse profile variations of the source. However; in this thesis, only the timing part is covered.

4.1   Introduction

On 2009 April 2 (MJD 54923), the Swift-BAT detected a new transient X-ray source SWIFT J0513.4–6547 in the LMC [123]. An archival analysis of BAT data brought out that the source had been active since 2009 March 4 (MJD 54894) and had reached a peak brightness of ~ 40 mCrab on 2009 March 6. Monitoring observations with RXTE tracked the decline of the outburst until 2009 May 13 (MJD 54964). The detection of strong pulsations with a period around 27.28 s during the outburst and the association of the X-ray transient with the high-mass optical source[1] have led SWIFT J0513.4–6547 to be identified as a HMXB [123]; [124]).

---

[1] 2MASS 05132826–6547187

A recent study ([125];[126]) on 4.5 years of OGLE IV[2] light curve revealed regular modulation of the optical magnitude. Approximately 0.05 mag flickering in every 27.4 d confirms the binary nature of SWIFT J0513.4–6547, assuming that the optical modulation represents the binary period of the system. Coe et al. [126] refined the frequency measurements of Finger & Beklen [121] from Fermi/GBM detections and derived the orbital parameters of the system. They provided an upper limit of 0.17 to the eccentricity using a model with a fixed orbital period of 27.405 d.

Coe et al. [126] also studied the optical spectrum and identified the companion as a B1Ve star. The position of SWIFT J0513.4-6547 on the Corbet diagram [127] affirms the Be/X-ray binary nature. Generally X-ray outbursts of Be/X-ray binary systems occur in two different forms, classified as type I or type II [58]. Type I outbursts ($L_x \sim 10^{36-37}$ erg s^{-1}) are correlated with the binary orbit so that they are recurrently observed in certain orbital phases due to enhanced mass transfer. In contrast, type II outbursts ($L_x \geq 10^{37}$ erg s^{-1}) are less frequent, irregular but giant eruptions that decay along several orbital periods. 2009 outburst of SWIFT J0513.4-6547 can be identified as type II since its peak luminosity is derived as 1.3×10^{38} erg s^{-1} [126] and the outburst lasted for about two orbital cycles.

Recently, the source underwent another bursting activity in 2014. During the XMM-Newton detection on 2014 August 25 (MJD 56894), the luminosity was at the order of 10^{36} erg s^{-1} [128]. Seven follow-up Swift observations until the end of the year show that the luminosity peaked twice at the same level, September 19 (MJD 56919) and October 16 (MJD 56946). These three outbursts on August 25, September 19 and October 16 can be classified as type I since their occurrence times are just about the expected optical maxima.

The structure of this Chapter is built as follows: Section 4.2 describes the SWIFT and RXTE observations and light curve extraction procedure, Section 4.3 demonstrates the results of the pulse timing analysis of 2009 and 2014 outbursts, Section 4.4 presents the discussion.

---

[2] Optical Gravitational Lensing Experiment Phase IV

4.2 Observations

4.2.1 RXTE

18 target of opportunity observations (see Table 4.1) with RXTE-PCA [129] were carried out between 2009 April 14 (MJD 54935) and 2009 May 13 (MJD 54964). These observations witness the decline of the 2009 outburst of SWIFT J0513.4–6547. The data are subjected to standard analysis using the tools of HEASOFT V.6.15.1. Time filtering is applied with the criteria on elevation angle to be greater than $10°$, offset from the source to be less than $0°.02$ and electron contamination of PCU2 to be less than 0.1. We also exclude data within 30 min of the peak of South Atlantic Anomaly in order to increase signal-to-noise ratio (SNR). The resulting net exposure after the filtering is 24 ks.

Table 4.1: Log of RXTE-PCA observations of SWIFT J0513.4-6547

RXTE Proposal ID	Time (MJD)	Number of pointings	Exposure (ks)
94065	54935-54947	10	14.24
94421	54948-54964	8	9.73

GoodXenon events are used to generate 0.1 s binned 3-10 keV light curves for the timing analysis. Background subtraction is applied for the light curve by using EPOCH 5C background model supplied for faint sources (i.e. < 40 cts s^{-1} PCU^{-1}).

4.2.2 SWIFT

After the Swift-BAT discovery of SWIFT J0513.4–6547, three follow-up Swift-XRT [130] observations were performed on 2009 April. Moreover, when the source re-brightened on 2014 August, seven pointing observations were completed until the end of 2014. A log of Swift-XRT observations is given in Table 4.2. The total exposure of 2009 and 2014 observations are 12.67 and 7.92 ks, respectively. The observations of SWIFT J0513.4-6547 are in photon counting mode which has a time

resolution of ~ 2.5 s. XRT event files are filtered with the default screening criteria of XRTPIPELINE V.0.13.0 script of XRTDAS V.2.9.2 package. Standard grade filtering (0–12) is applied to the data. For each observation, vignetting-corrected exposure maps are generated during the pipeline processing.

Table 4.2: Log of Swift-XRT observations of SWIFT J0513.4–6547. The observations given above the horizontal dashed line are from 2009, whereas 2014 observations are below the dashed line.

SWIFT ObsID	Time (MJD)	Off-axis (arcmin)	Exposure (ks)
00031393001	54932	0.45	4.63
00031393002	54937	0.35	6.34
00031393003	54940	1.01	1.69
00031393004	56916	0.10	0.93
00031393005	56919	2.12	1.41
00031393006	56925	0.39	0.97
00031393007	56939	2.48	1.00
00031393008	56946	1.53	1.24
00033532001	56985	2.39	1.31
00033532002	56986	1.21	1.05

Throughout the 2009 observations of SWIFT J0513.4-6547, count rates were just around the pile-up limit (~ 0.5 cts s^{-1}); therefore, the events are corrected for pile-up. For these observations, an annular source region is selected in order to exclude an inner circle of radius ~ 7 arcsec, while the outer radius of the annulus is ~ 70 arcsec. In contrast, the count rates of 2014 observations were low (~ 0.1 cts s^{-1}), consequently a circular source extraction region with ~ 35 arcsec radius is chosen. The same circular source-free region with ~ 140 arcsec radius is used for background extraction for both 2009 and 2014 observations. Light curves are extracted by filtering selected regions using XSELECT V.2.4C.

4.3 Timing Analysis

For the RXTE-PCA and Swift-XRT observations in 2009 (see Tables 4.1 and 4.2), we construct background-subtracted light curves. The resulting RXTE and Swift light curves are 0.1 and 2.51 s binned, respectively. We correct the light curves with respect to the Solar system barycenter. The light curves are also corrected for the orbital binary motion using the orbital parameters given by Coe et al. [126].

The nominal pulse period is estimated, by folding RXTE-PCA barycentric light curve on statistically independent trial periods [106]. We search for periodicity using χ^2 test and use the template pulse profile giving the maximum χ^2. Then, we fold the RXTE-PCA and Swift-XRT light curves with the best period obtained from RXTE-PCA light curve. Pulse profiles are obtained with 10 and 20 phase bins from Swift-XRT and RXTE-PCA, respectively. Pulse profiles are represented by their Fourier harmonics [109]. Then, we obtain the pulse arrival times for each observation by cross-correlating the pulses with template pulse profile.

The phase-connected pulse arrival times after the binary orbital correction are shown in the top panel of Fig. 4.1, whereas the residuals after the removal of the quadratic trend are shown in the bottom panel of Fig. 4.1. From this quadratic trend, spin-up rate is found to be $1.74(6) \times 10^{-11}$ Hz s^{-1}. Reduced χ^2 of this fit is around 1.07. This suggest that the orbit of the system is circular which was also suggested by Coe et al. [126]. Coe et al. [126] also found an upper limit of 0.17 to the eccentricity within 2σ confidence level. In order to find a further constraint on eccentricity, an elliptical orbital model is fitted to the residuals as suggested by Deeter et al. [108]. This fit gives an upper limit to the eccentricity as 0.028 in 2σ level. It should also be noted that the time coverage of pulse arrival times is only 63 per cent of orbital period. Full orbital coverage of arrival times is needed to obtain a better constraint on the eccentricity.

SWIFT J0513.4-6547 was also observed seven times in 2014 within a time span of ~ 70 d (see Table 4.2). As for the 2009 observations, we construct background-subtracted 2.51 s binned lightcurves from 2014 observations. We construct pulse phase profiles for five of these observations and connect them in phase.
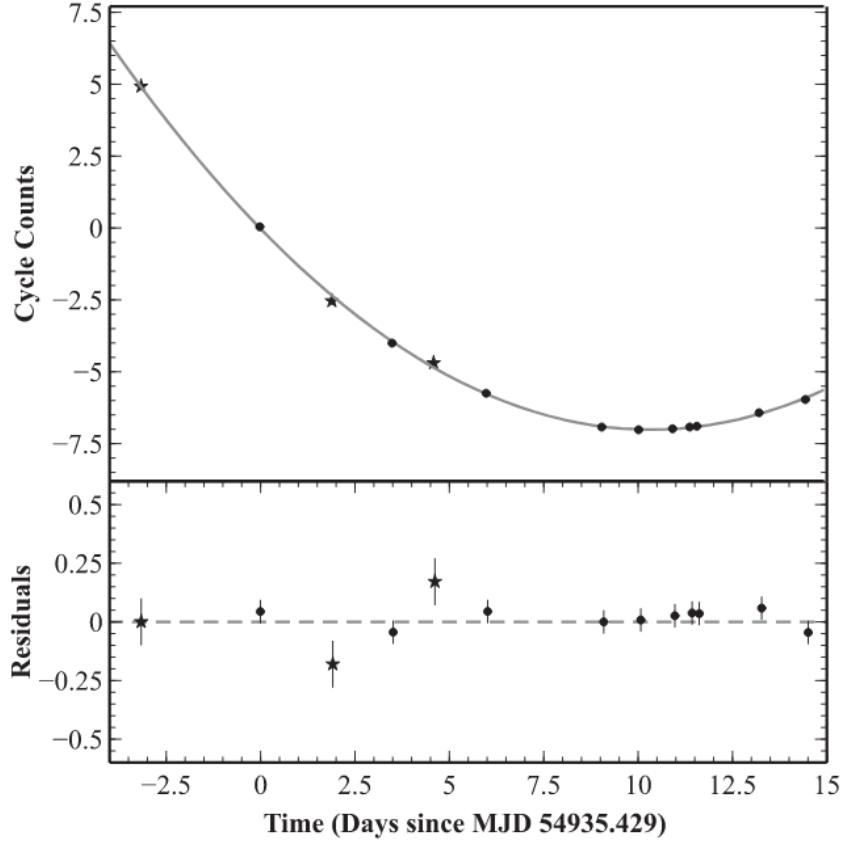
Figure 4.1: Top: arrival times obtained from RXTE-PCA and Swift-XRT observations in 2009 after binary orbital correction. Data points indicated by asterisks correspond to Swift-XRT measurements. Quadratic fit is shown as the grey line. Bottom: residuals after the quadratic trend is removed.

Table 4.3: Timing solutions of 2009 and 2014 observations.

Parameter	2009 Solution	2014 Solution
Epoch (MJD)	54935.42866	56916.89857
ν (10^{-2} Hz)	3.67020(7)	3.64432(5)
$\dot{\nu}$ (Hz s^{-1})	$1.74(6) \times 10^{11}$	$-(5.92 \pm 1.9) \times 10^{-14}$

Pulse arrival times are presented in Fig. 4.2. Among 2014 observations listed in Table 4.2, no significant pulse detection is obtained from the observation at MJD 56939, and a single pulse arrival time is measured from the observations at MJD 56985 and

54

MJD 56986. The pulse frequency measurement of the timing solution is consistent with the value reported by [128] within 1σ level. Furthermore, a spin-down rate of $(5.92 \pm 1.9) \times 10^{-14}$ Hz s^{-1} is found during this 70 d time span. Timing solutions of 2009 and 2014 are given in Table 4.3.
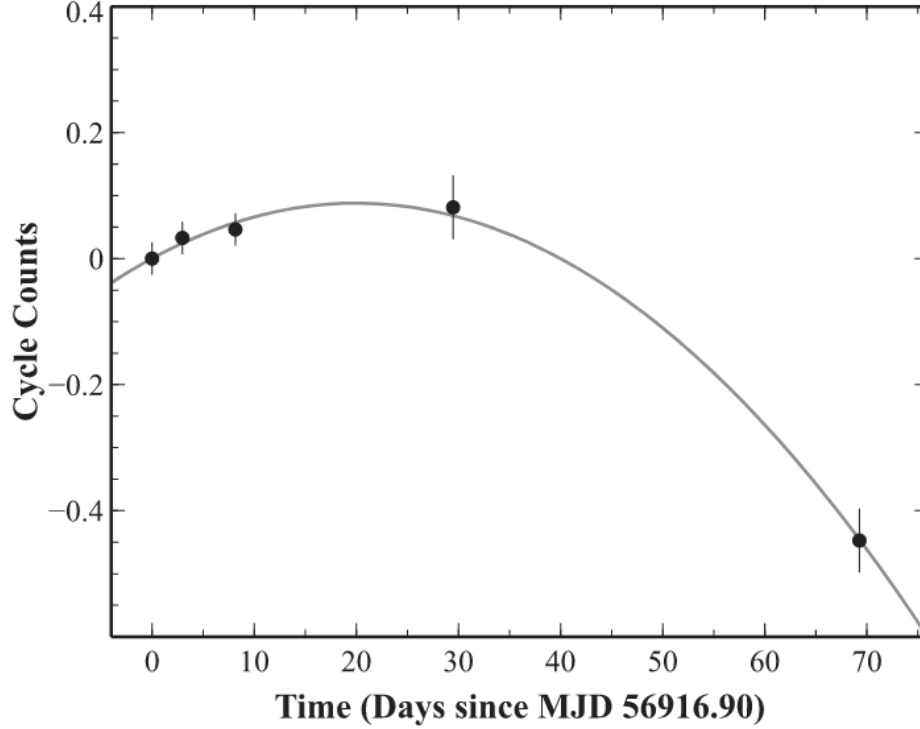
Figure 4.2: Arrival times obtained from Swift-XRT observations in 2014 after binary orbital correction. Quadratic fit is shown as the grey line.

4.4 Discussion

The X-ray luminosity of 2009 outburst was initially at its peak value of $L_x \sim 1.3 \times 10^{38}$ erg s^{-1} [126]. It was found to decrease below $\sim 10^{37}$ erg s^{-1} towards the end of the outburst. The source disappeared for ~ 2000 d and then reappeared in 2014 with $L_x \sim 10^{36}$ erg s^{-1}.

Our frequency measurement from 2009 observations which correspond to the final stage of the outburst (see Table 4.3) complies with the general spin-up trend of the initial stage of the outburst presented by [126]. Moreover, it is important to note that

the arrival times bolster Coe et al. [126] assuming that the orbital and optical periods are the same.

The source is found to be spinning up with a rate of 1.74×10^{-11} Hz s^{-1} during the final stage of the outburst of the 2009 outburst. Comparison with the values found for the initial stages of the 2009 outburst ($\sim 3.75 \times 10^{-11}$ Hz s^{-1}; [126] suggests that the spin rate of the source is correlated with the X-ray luminosity.

On the other hand, from Table 4.3, it is also found that the long-term (~ 1966 d long) average spin-down rate of the source during the quiescence between 2009 and 2014 is $\sim 1.52 \times 10^{-12}$ Hz s^{-1} which is about two orders higher than the rate measured during the re-brightening on 2014. This shows that, when the X-ray luminosity of the source increased in 2014, its spin-down rate is found to be smaller (i.e. spin rate value becomes greater).

Thus, whether the source spins up or spins down, its spin rate increases with the X-ray flux. Qualitatively, this trend suggests in general that the source spin rate is correlated with the X-ray luminosity. Observations from future outbursts of the source will be useful to better understand the spin rate – X-ray luminosity relation of the source.

It is important to note that the long-term spin-down rate of $\sim 1.52 \times 10^{-12}$ Hz s^{-1} corresponds to a state where the source is quiescent. Although this spin-down rate is comparable to the long-term spin-down rates of persistent accretion powered X-ray pulsars such as GX 1+4 [131], it is not typical within the quiescent states of the transient sources. Although some transient sources are either found to be spinning up or spinning down in their quiescent states in between outbursts (e.g. GS 0834-430, A 0535+262; see [132]), only a few of them such as SXP 7.78 ([133]) exhibits long-term (~ 1000 d long) quiescent states for which the spin-down rates have the same order of magnitude.

If we assume that the neutron star is in propeller state throughout the whole quiescent time interval, magnetic dipole ($\mu \approx BR^3$, where B is the surface dipole magnetic field and R is the radius of the neutron star) can be estimated ([134]) as

$$\mu = \frac{(I|\dot{\Omega}|GM)^{1/2}}{\Omega},$$

(4.1)

where I is the moment of inertia, $\dot{\Omega}$ is the spin rate, M is the mass and Ω is the

frequency of the neutron star. Using equation (1), for a neutron star of mass 1.4 $M_\odot$, moment of inertia of 10^{45} g cm^2 and a radius of 10^6 cm, surface dipole magnetic field is estimated to be $\sim 1.5 \times 10^{13}$ G which is in good agreement with the magnetic field estimation by [126] during the accretion phase using spin-up rate – luminosity relation.

We confirm that SWIFT J0513.4–6547 has a circular orbit by refining the upper limit for the orbital eccentricity as 0.028 in 2σ confidence level. Although many of the BeXB systems (especially the ones that have transient nature) have eccentric orbits, some of the transient BeXB systems such as KS 1947+300 ([135]), 4U 1901+03 ([136]), 2S 1553-542 ([137]) and RX J0520.5-6932 ([138]) have orbits with small eccentricities.

CHAPTER 5

SXP 1062

This Chapter presents timing analysis of the accretion-powered pulsar SXP 1062 with Swift, XMM–Newton, and Chandra observations between 2012 October 9 and 2014 November 23. First, orbital parameters of the binary system are found. In addition, a glitch event is resolved on MJD 56834.5 which is the first observational evidence that accretion powered pulsars may glitch like isolated pulsars. Furthermore, the fractional size of the glitch ensures that it is the largest glitch reported up to now. The work represented in this Chapter is based fully on the article entitled "*Discovery of a Glitch in the Accretion Powered Pulsar SXP 1062*" which is published in MNRAS journal [139].

5.1 Introduction

SXP 1062 is a Be/X-ray binary (BeXB) system discovered in the eastern wing of the SMC [140]. The detection of strong X-ray pulsations with a period of 1062 s revealed that the compact object in this system is a slowly rotating pulsar. Furthermore, SXP 1062 is associated with a supernova remnant (SNR) and its kinematic age is calculated to be as young as 10–40 kyr ([141];[140]). The theoretical contradiction between its long period and young age puts SXP 1062 at the centre of a remarkable attention.

The spectral type of the optical counterpart 2dFS 3831 is specified to be B0-0.5(III)e+ [140]. Moreover, spectroscopic observations imply that the large circumstellar disc around the counterpart has been growing in size or density [142]. I-band photometry carried on by OGLE [143] revealed periodic magnitude variations that signify that the orbital period of the binary system is likely to be 656 d [144].

The X-ray spectrum of SXP 1062 is basically described by an absorbed power law. Additionally, thermal components are used to describe a possible soft excess below 1 keV ([140]; [142]). A 3σ evidence for the Fe Kα emission line at 6.4 keV is also reported by [142]. Furthermore, a search for a proton cyclotron absorption line on the 0.2-10 keV continuum yields no significant evidence [142].

First four pulse period measurements of SXP 1062 in 2010 demonstrate a very high spin-down rate of $\dot{\nu} = -2.6 \times 10^{-12}$ Hz/s during a short observation interval of 18 d [141]. The following period is measured ~ 2.5 yr later, which implies a factor of 40 lower long-term spin-down rate [142]. In view of the fact that most BeXRBs show spin-up during their outbursts [132], SXP 1062 is atypical with its strong spin-down.

The extraordinary observational properties of SXP 1062; such as its long pulse period, strong spin-down and young age; have led several authors to implement different theoretical models in order to explain the true nature of the source [145]. First, Haberl et al. [141] suggested that the initial pulse period of the neutron star at birth might be unusually long and calculated a lower limit of 0.5 s. Another explanation given by [146] indicated that the initial magnetic field of the neutron star at birth might be as large as 10^{14}G which then experienced a field decay. On the other hand, Ikhsanov [147] proposed that the initial magnetic field could be $\sim 4 \times 10^{13}$ G once the magnetization of the accretion flow is introduced within the scope of the magnetic accretion scenario. Fu & Li [148] pointed out that SXP 1062 may currently have a magnetic field higher than 10^{14} G, although no cyclotron line is detected on the X-ray spectrum. The possibility of a high magnetic field nominates SXP 1062 as an accreting magnetar; however, Postnov et al. [149] claim that quasi-spherical accretion theory ([104]; [150]) estimates a lower limit for the magnetic field which is consistent with the standard values for neutron stars.

Chapter is outlined as follows: in Section 5.2, the observations used in the study together with their data screening options are described. Then, in Section 5.3, the timing analysis and its results are explained. Finally in Section 5.4, a discussion presented over the fact that the observed glitch should be associated with the internal structure of the neutron star.

5.2 Observations

Swift monitoring campaign of SXP 1062 begins during an X-ray outburst on 2012 October 9 and continues until 2014 November 23. Throughout a time about 2 yr, 87 pointing observations have a total Swift–XRT [130] exposure of ~ 164 ks. XRT operates in 0.2-10 keV energy range, with an effective area of 110 cm^2 at 1.5 keV. Its spatial resolution is 18 arcsec and its field of view (FOV) is 23.6 arcmin $\times$ 23.6 arcmin. This focusing instrument automatically switches between four operation modes depending on the source count rate. The operation mode of SXP 1062 observations is photon counting (PC) mode, which has a timing resolution of ~ 2.5 s. Clean event files are produced with the script XRTPIPELINE V.0.13.2 by using a default screening criteria. Light curves and spectra are extracted with XSELECT V.2.4D. Circular regions selected for source and background extraction have a radius of 35 and 141 arcsec, respectively. In order to investigate the evolution of X-ray luminosity, consecutive 8–10 observations are combined and spectral files are extracted for each group of observations. Spectra are re-binned to have at least five counts per bin and Cash statistic [151] is preferred during spectral fitting with XSPEC v.12.9.0.

The spectra is modeled with an absorbed power law and measure the X-ray flux in 0.3–10 keV energy band. Then, the flux values are converted to luminosity by using the distance to SMC that is 60 kpc [152]. X-ray luminosity evolution is plotted on the lower panel of Fig. 5.1.

OGLE [143] monitoring of SXP 1062 provides I-band photometry measurements of the optical counterpart, which are received from the X-Ray variables OGLE Monitoring System (XROM;1 [143]). Periodic optical outbursts are evident on the OGLE light curve (see the upper panel of Fig. 5.1). This periodicity of ~ 656 d is associated with the binary orbit of the system [144].

SXP 1062 is also observed with XMM–Newton and Chandra observatories. The XMM–Newton observation has a duration of ~ 86 ks on 2013 October 11. We use single and double-pixel events (PATTERN 0–4) of EPIC-PN camera [153] that is sensitive to the photons in 0.15–15 keV energy range and possesses an FOV of 30 arcmin with a spatial resolution of 6 arcsec. During this observation, EPIC-PN camera oper-
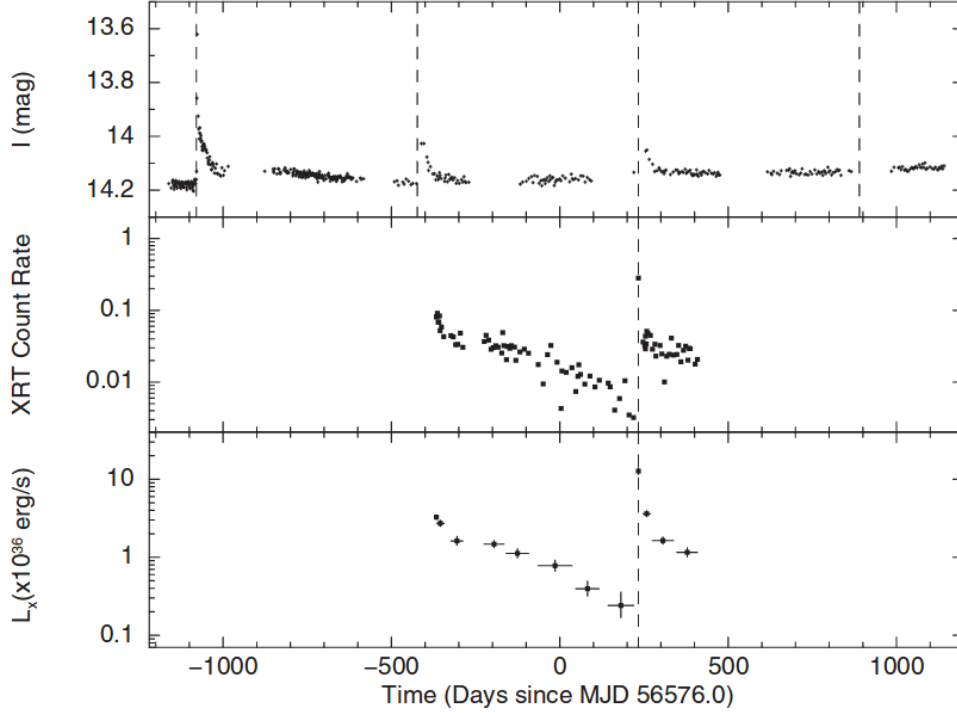
Figure 5.1: Upper panel: I-band optical light curve of the counterpart provided by OGLE. The dashed lines indicate the times of optical outbursts calculated according to ~ 656 d orbital period [144]. Middle panel: X-ray light curve of SXP 1062 from Swift-XRT observations. Each point represents an observation. The dashed line indicates the time of the X-ray outburst, that is MJD 56809.5. Lower panel: X-ray luminosity evolution in 0.3-10 keV energy band (calculated by using the distance to SMC: 60 kpc [152]). The maximum luminosity, 1.3×10^{37} erg s^{-1}, is indicated with a dashed line.

ated on the full frame mode that has a time resolution of 73 ms. The data reduction is carried out with SAS v.15.0.0 software. Filtering of high-energy background flare times yields a net exposure of ~ 47 ks. We also avoid bad pixels by rejecting events with FLAG ≥ 0. In addition, three pointing observations taken with Chandra–ACIS detectors [154] are between 2014 June 29 and July 18, with a total exposure of ~ 87 ks. ACIS detectors have 17 arcmin $\times$ 17 arcmin FOV and operates in 0.2–10 keV energy band. All observations are conducted in the imaging mode with a time resolution of ~ 0.5 s. The data is analysed with CIAO v.4.9 software [155]. Default screening criteria are applied while producing the clean events. Extracted light curves have 1 s

bin time for both XMM–Newton (in 0.2-12 keV) and Chandra (in 0.2–10 keV) and all time series are converted to Solar system barycentre. Circular source extraction regions have radii of 25 and 8 arcsec for XMM–Newton and Chandra, respectively. Background emissions are estimated from source-free circular regions on the same detector chip as the source.
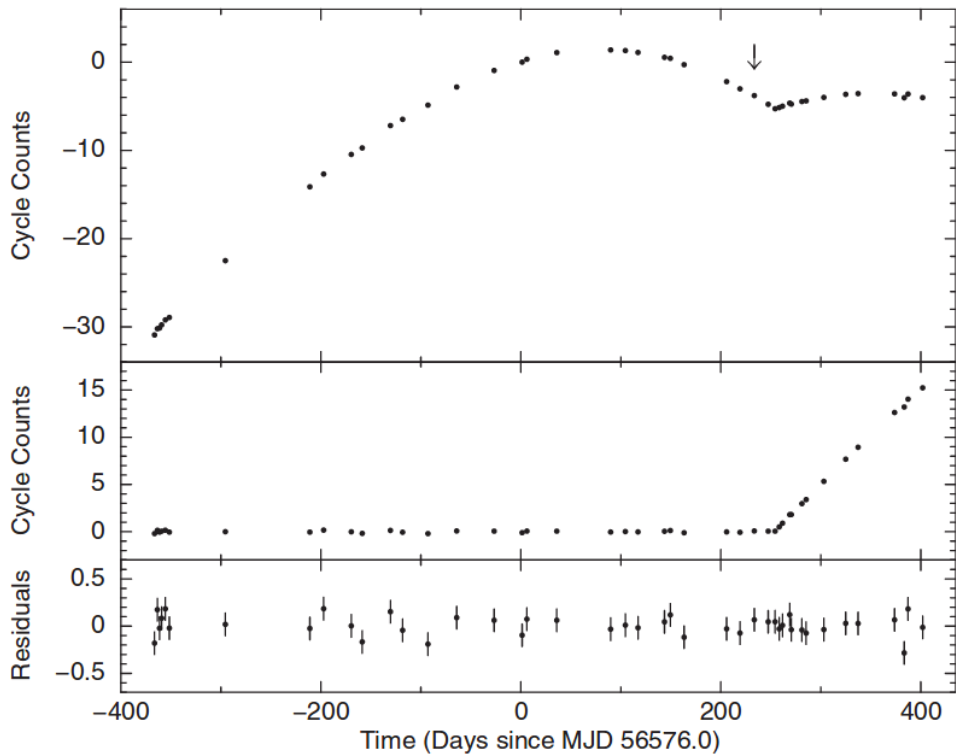
Figure 5.2: Upper panel: Cycle counts of pulse phase obtained by expanding the TOAs. The time denoted with an arrow mark corresponds to the X-ray outburst of SXP 1062, that is MJD 56809.5. Middle panel: Phase offset series after the removal of the secular spin-down trend and the orbital model given in Table 5.1. The glitch event is evident on MJD 56834.5 and it is 25 days after the X-ray outburst. Lower panel: Residuals after an additional removal of the glitch event. The final model has a reduced χ^2 of 1.0.

5.3 Timing Analysis

The barycentric light curves are generated from Swift, Chandra and XMM-Newton observations described in the previous section. First, we search for periodicity on the light curve of the XMM–Newton observation on MJD 56576.7 by folding it on trial periods [106]. The period that give the maximum χ^2 value is 1073.5 s. Then, all observations are folded with the same ephemeris and frequency. For each observation, pulse profiles with 10 phase bins are constructed. Observations that have an exposure less than the pulse period of SXP 1062 yield pulse profiles with zero count bins, therefore they are excluded during the timing analysis. The pulse profiles are described with harmonic representation as [109]

$$f(\phi) = F_0 + \sum_{k=1}^{n} F_k \, cosk(\phi - \phi_k) \qquad (5.1)$$

where n is the number of harmonics used for the representation of a pulse. Similarly, the template pulse profile is obtained from the longest observation (~ 47 ks) that is held on MJD 56576.7 with XMM–Newton. The template pulse profile is represented as

$$g(\phi) = G_0 + \sum_{k=1}^{n} G_k \, cosk(\phi - \phi_k) \qquad (5.2)$$

The time of arrival (TOA) of each pulse is estimated by searching the location of the maximum in the cross-correlation with template pulse ([109]; see also [156]),

$$\Delta\phi = \frac{\sum_{k=1}^{n} k F_k G_k \, sink\Delta\phi_k}{\sum_{k=1}^{n} k^2 F_k G_k \, cosk\Delta\phi_k} \qquad (5.3)$$

To check how pulse timing is affected by the changes in pulse profiles, TOAs are re-generated by using different number of harmonics. The obtained TOAs are consistent within 1σ level for all harmonics; therefore, pulse timing analysis is performed by using five harmonics. In order to examine the timing behaviour of SXP 1062, the first segment to focus is on pre-outburst TOAs which are described as

$$\phi(t) = \phi_0 + \nu_0(t - t_0) + \frac{1}{2}\dot{\nu}(t - t_0)^2 + .. \qquad (5.4)$$

where t_0 is the folding epoch, ν_0 is the spin frequency and $\dot{\nu}$ is the derivative of the spin frequency, respectively. TOAs are around the spin-down rate previously reported by [142] and obtain a phase coherent timing solution (see the upper panel of Fig. 5.2).

64
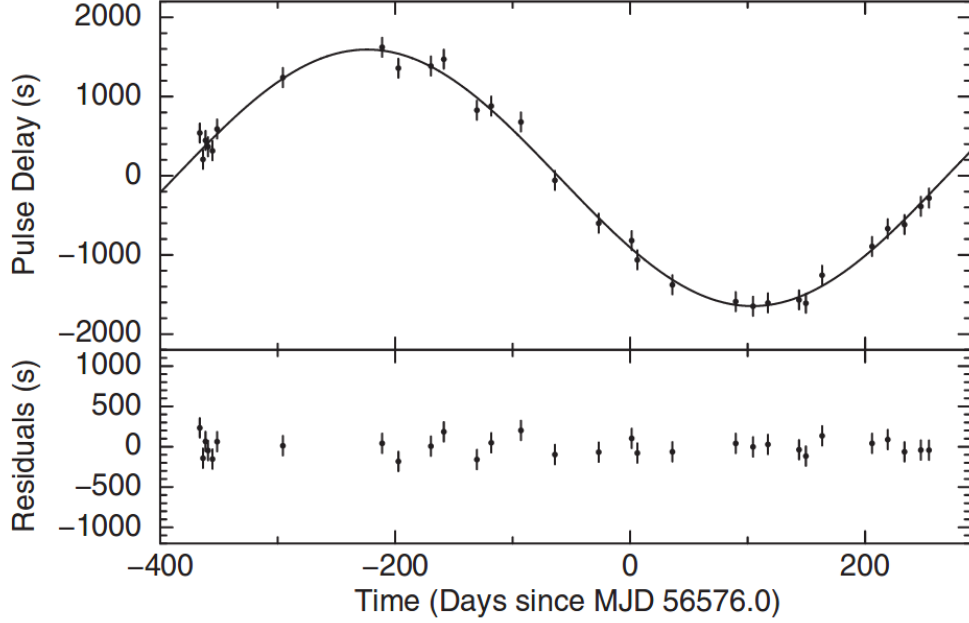
Figure 5.3: *Upper panel*: Doppler delays on the residuals after the removal of the spin-down from TOAs prior to the glitch, are fitted with a circular orbital model (solid line) with a reduced χ^2 of 1.0. The orbital parameters are given in Table 5.1. *Lower panel*: Residuals after the removal of orbital model.

The source is found to be spinning down with a rate of $\dot{\nu} = -4.29(7) \times 10^{-14}$ Hz s^{-1} between MJD 56209 and MJD 56830 (see Table 5.1).

The residuals after the removal of the spin-down trend are given in Fig. 5.3. The fluctuation on the residuals is consistent with Doppler delays due to orbital motion. In general for an eccentric orbit, it can be represented as ([108]; see also [157]; [158]; [159], for applications)

$$\delta t_{orbit} = x sin(l) - \frac{3}{2}x\, esin(w) + \frac{1}{2}xecos(w)sin(2l) - \frac{1}{2}xesin(w)cos(2l) \quad (5.5)$$

where $x = \frac{a_x}{c}sini$ is the light travel time for projected semi-major axis, i is the inclination angle between the line of sight and the orbital angular momentum vector, $l = 2\pi(t - T_{\pi/2})/P_{orb} + \frac{\pi}{2}$ is the mean orbital longitude at t, $T_{\pi/2}$ is the epoch when the mean orbital longitude is equal to $90°$, P_{orb} is the orbital period, w is the longitude of periastron and e is the eccentricity. Since the time span of fitted TOAs covers less than one orbital cycle, we fix the orbital period to $P_{orb} = 656(2)$ d as reported by [144] and seek for other orbital parameters. The best fit with a reduced χ^2 of 1.0 (see Fig. 5.3

Table 5.1: Binary orbit, timing solution and glitch parameters of SXP 1062. A number given in parentheses is the 1σ uncertainty in the least significant digit of a stated value.

Circular Orbit Model:	
Orbital Epoch (MJD)	56351(10)
P_{orb} d	656(2)
a_x/c sini (lt-s)	1636(16)
Timing Solution:	
Folding Epoch (MJD)	56576.0
Validity Range (MJD)	56209-56830
ν_0 (mHz)	0.931787(5)
$\dot{\nu}$ (Hz s^{-1})	$-4.29(7) \times 10^{-14}$
Glitch Parameters:	
t_g (MJD)	~ 56834.5
Validity Range (MJD)	56834-56978
$\Delta\nu$ (mHz)	$1.28(5) \times 10^{-6}$
$\Delta\dot{\nu}$ (Hz s^{-1})	$-1.5(9) \times 10^{-14}$
$\Delta\nu/\nu_0$	$1.37(6) \times 10^{-3}$
$\Delta\dot{\nu}/\dot{\nu}_0$	0.3(2)

and Table 5.1) yields a circular orbit with orbital parameters a $\frac{a_x}{c}sini = 1636(16)$ lt-s and $T_{\pi/2} = 56351(10)$ MJD. Furthermore, a search for eccentricity leaving all orbital fit parameters free including the orbital period gives an estimate for the upper limit to the eccentricity as 0.2 at 1.6 σ that is 90 per cent confidence level [160]. Using these results, the mass function $f(M)$ can be calculated via

$$f(M) = \frac{4\pi^2}{G} \frac{(a_x sini)^3}{P_{orb}^2} = \frac{(M_c sini)^3}{(M_x + M_c)^2},$$ (5.6)

here M_c is the mass of the counterpart and M_x is the mass of the neutron star. The mass function calculated via orbital parameters is $f(M) \simeq 10.9(3)M_\odot$. Assuming a neutron star with a mass of 1.4 $M_\odot$, the relation between the inclination angle and the donor mass is plotted in Fig. 5.4. Considering the typical evolutionary mass of the optical counterpart as $\sim 15M_\odot$ [140], the inclination angle would be $i \simeq 73(2)$.
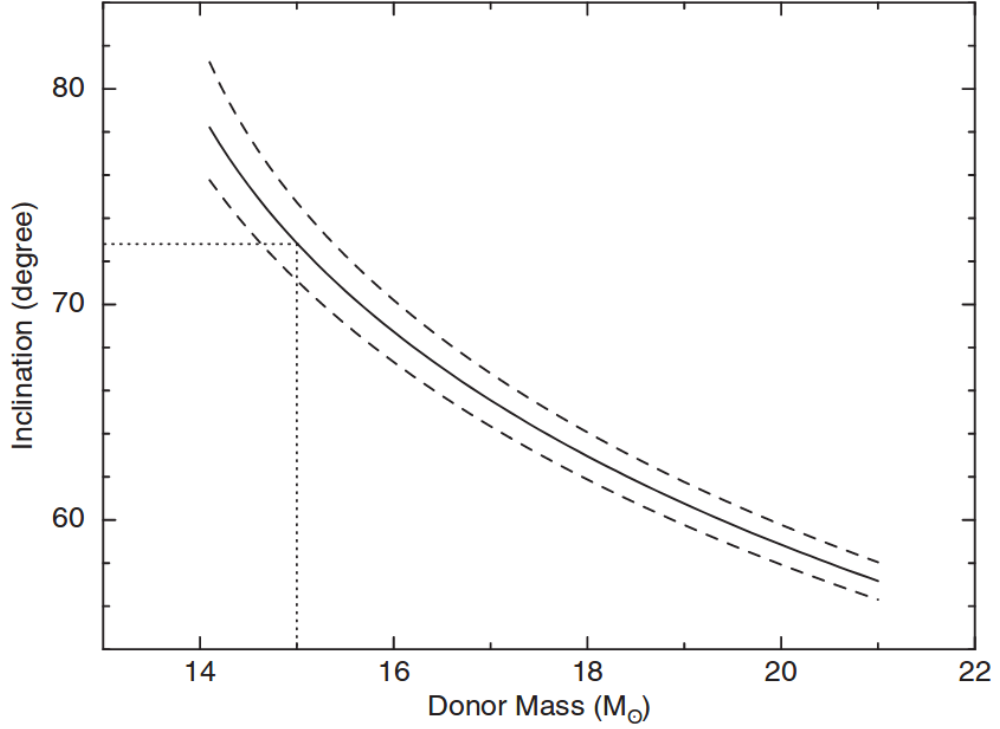
Figure 5.4: The relation between the binary system inclination angle and the donor mass in units of $M_\odot$. The solid curve is constructed by using the mass function value of $10.9 M_\odot$, whereas the dashed curves are constructed for 1σ error in the mass function ($\pm 0.3 M_\odot$). For a donor mass of $\sim 15 M_\odot$ [140], we find that the inclination angle would be $\simeq 73(2)^\circ$.

In the middle panel of Fig. 5.2, the residuals after the removal of both the spin-down trend and the orbital model from all TOAs are shown. The TOAs after MJD 56834.5 show a sudden change in slope that indicates a possible glitch event. The TOAs after the glitch are modeled with a second-order polynomial $\Delta\phi = \phi_0 + \delta\nu(t - t_g) + \delta\dot{\nu}(t - t_g)^2$, where t_g is the time of the glitch event. Thus, pulse frequencies receive a correction of $\nu_0 + \delta\nu + \delta\dot{\nu}(t - t_g)$. The glitch event occurs on MJD 56834.5 and it causes a frequency shift of $\Delta\nu = 1.28(5) \times 10^{-6}$ Hz along with a change of spin-down rate $\Delta\dot{\nu} = -1.5(9) \times 10^{-14}$Hz s^{-1} (see Table 5.1). In the lower panel of Fig. 5.2, the residuals after the glitch correction is illustrated.

5.4 Discussion

5.4.1 The Orbit

The accretion-powered pulsar SXP 1062 is in a BeXB system. In BeXBs, the neutron star accretes matter from the stellar wind of a main-sequence star, which is in the form of a circumstellar disc around the mass donor. Generally, the orbits of BeXBs are relatively wide and moderately eccentric ($P_{orb} \geq 20$ d, $e \geq 0.3$; [42]). While the neutron star passes through the edge of circumstellar disc of the Be companion, it interacts with the material and accretion takes place. The X-ray emission of most BeXBs is transient; however, persistent BeXBs with low luminosities ($L_x \sim 10^{34\check{\ }35}$ erg s^{-1}) also exist. Persistent systems are known to contain slower pulsars that have wider orbits ($P_s > 200$ s, $P_{orb} > 200$ d; [161]; [42]). Although most BeXBs have eccentric orbits, there are several systems (i.e. X Per, GS 0834–430, KS 1947+300) with low eccentricity ($e < 0.2$).

Transient BeXBs show two types of X-ray outbursts [58]. Type I outbursts ($L_x \sim 10^{36-37}$ erg/s) occur once in a while the pulsar passes from the periastron of the orbit, where accretion enhances. On the other hand, Type II outbursts are major events ($L_x \geq 10^{37}$ erg/s) that occur during mass ejection episodes of the counterpart. Transient BeXBs may have very low quiescence luminosities ($L_x \leq 10^{33}$ erg/s). The luminosity increase during a Type II outburst can be three to four orders of magnitudes, while it is only about one order of magnitude for a Type I outburst [42]. When an X-ray outburst occurs in a BeXB, the neutron star generally enters a spin-up episode due to enhanced accretion.

As the population of BeXBs has grown in the past decades, the pulse periods (P_s) of pulsars in BeXBs are still strongly correlated with the orbital periods (P_{orb}), as it is first demonstrated by [127]. Although there is a large scatter in data, a positive correlation is evident with $P_s \propto P_{orb}^2$. The large BeXB population in SMC also obeys this relation ([162]; [163]). Therefore in BeXBs, pulsars with longer pulse periods reside in binary systems with wider orbits and consequently lower accretion rates. The optical light curve of SXP 1062 (see Fig. 5.1) shows periodic variations devoted to an orbital period of ~ 656 d [144]. X-ray observations of the source reveal the

occurrence of a Type I outburst ($L_x \simeq 1.3 \times 10^{37}$ erg/s) that happen together with the optical enhancement (see Fig. 5.1). However, the long-term spin-down of SXP 1062 is not interrupted by the outburst. Prior to the X-ray outburst a minimum luminosity of 2.4×10^{35} erg/s is measured, hence the luminosity increases by a factor of ~ 50 during the outburst. The outburst of SXP 1062 is observed only during an observation with an exposure of 2.2 ks; however, the actual duration of the outburst might be longer since neighboring observations are 14 d apart. The luminosity drops to 3.6×10^{36} erg/s; therefore, the outburst finishes in the following observation. These characteristics classify SXP 1062 as a persistent BeXB. In this study, the orbital motion of SXP 1062 is resolved from its X-ray emission observed for ~ 2 yr (see Fig. 5.3). We determine the orbital epoch as 56351(10) MJD and the light travel time for projected semi-major axis as 1636(16) lt-s by considering a circular orbit with a period of 656(2) d (see Table 5.1). The results also indicate an upper limit of 0.2 to the eccentricity at 90 per cent confidence level, therefore SXP 1062 is claimed to be in a low eccentric orbit despite the fact that denser observational coverage is needed for a better assessment. The orbital and pulse periods of the system position the source on a place in line with BeXBs on the Corbet diagram, the uppermost right end of the existing correlation for BeXBs. Moreover, the mass function of the system is calculated to be $f(M) \simeq 10.9(3)$ M$_\odot$, which seems appropriate bearing in mind that the Be companion is suggested to have a mass of ~ 15 M$_\odot$ [140]. Consequently, the orbital inclination can be evaluated as $i \simeq 73(2)°$. The inclination angle as a function of the donor mass is plotted in Fig. 5.4. Using this relation, the minimum donor mass is determined to be 13.3(3) M$_\odot$ for $i = 90°$.

5.4.2 Magnetic field estimation from secular spin-down trend before the glitch

If we consider that the source is accreting via a prograde accretion disc that is formed before the glitch, standard accretion disc theory ([68]; [69]; [70]; [164]; [165]; [166]) can be used to estimate the surface magnetic field of the neutron star. For this scenario, the inner radius of the accretion disc at which the magnetosphere disrupts the Keplerian rotation depends on the accretion rate ($\dot{M}$) and the magnetic dipole moment of the neutron star ($\mu = BR^3$, where B is the surface magnetic field and R is

the radius of the neutron star) as

$$r_0 = K\mu^{4/7}(GM)^{-1/7}\dot{M}^{-2/7}, \tag{5.7}$$

where K is a dimensionless parameter of about 0.91 and M is the mass of the neutron star ([68]; [69]). The torque can then be estimated as

$$2\pi I\dot{\nu} = n(\omega_s)\dot{M}l_K, \tag{5.8}$$

where I is the moment of inertia of the neutron star, ν is the spin rate of the neutron star, $n(\omega_s)$ is the dimensionless torque that is a factor parameterizing the material torque and magnetic torque contributions to the total torque and $l_K = (GMr_0)^{1/2}$ is the angular momentum per mass added by the Keplerian disc at r_0. The dimensionless torque can be approximated as

$$n(\omega_s) \approx 1.4(1 - \omega_s/\omega_c)/(1 - \omega_s), \tag{5.9}$$

where ω_s, being equal to the ratio of the neutron star's rotational frequency to the Keplerian frequency at the inner radius of the accretion disc, is known as the fastness parameter and can be expressed as

$$\omega_s = 2\pi K^{3/2}P^{-1}(GM)^{-5/7}\mu^{6/7}\dot{M}^{-3/7} \tag{5.10}$$

where P is the pulse period of the neutron star. In equation (9), ω_c is the critical fastness parameter that has been estimated to be ~ 0.35 ([70]; [164]; [165]; [166]). For $\omega_s = \omega_c$, the total torque on the neutron star becomes zero [i.e. $n(\omega_s) = 0$] due to the negative torque contribution coming from the magnetic torque exerted outside the co-rotation radius at which the neutron star's rotational frequency equals to the Keplerian frequency.

For $\omega_s > \omega_c$, spin-down contribution coming from the outer disc outside the co-rotation radius is greater in magnitude than the total spin-up contributions coming from the material torque at the inner radius and the magnetic torque inside the co-rotation radius. This leads to a net spin-down of the neutron star [i.e. $n(\omega_s) < 0$]. On the contrary, for $\omega_s < \omega_c$, spin-up contribution coming from the material and magnetic torques is greater in magnitude than the spin-down contribution coming from the magnetic torques from the outer disc [i.e. $n(\omega_s) > 0$].

From a quadratic fit to the arrival times prior to the glitch, SXP 1062 is found to show a secular spin-down with a rate of $-4.29(7) \times 10^{-14}$ Hz/s when a maximum luminosity of $L_x \sim 3.3 \times 10^{36}$ erg/s is observed. Considering this luminosity value to be nearly the total accretion luminosity (i.e. $L = GM\dot{M}/R$)) and assuming a typical neutron star with $I = 10^{45}$ gcm^2, $M = 1.4M_\odot$ and $R = 10^6$ cm; equations 5.7–5.10 are solved numerically to obtain μ of about 1.5×10^{32} Gcm^3 leading to a magnetic field estimate of about 1.5×10^{14} G with $n(\omega_s) \approx -0.0123$ and $r_0 = 8.78 \times 10^9$ cm.

SXP 1062 can be considered to be a member of a class of accretion-powered pulsars in high-mass X-ray binaries with very slow pulsations and persistent spin-down states ([148]; [167]). Long spin periods together with the spin-down behavior of these pulsars are argued as an indication of their magnetar-like magnetic fields. Thus, this class is sometimes classified as 'accreting magnetars'. Alternatively by using a theoretical model based on quasi-spherical subsonic accretion, long spin periods of these systems have also been considered not to be necessarily related to magnetar fields [150].

Fu & Li [148] previously made use of three different theoretical approaches to obtain an estimate of the magnetic field of SXP 1062. First, they estimated the magnetic field strength by considering the time-scale for the ejector phase being comparable to the estimated age of the pulsar. Secondly, they estimated the magnetic field strength assuming the short-term spin-down rate of -2.6×10^{-12} Hz/s as being near the maximum spin-down rate in disc or spherical accretion ([168]; [169];[170]). Their final approach was to make use of the spin-down mechanism proposed by [171]. All these three approaches lead to a surface magnetic field of SXP 1062 as $\geq 10^{14}$ Gauss.

Our timing analysis shows that the source has a long-term secular steady spin-down trend at a rate of $-4.29(7) \times 10^{-14}$ Hz/s that could be a result of a steady disc accretion. Thus, using standard accretion theory, our magnetic field estimate for SXP 1062 follows consideration of accretion via prograde accretion disc with a small negative dimensionless torque. According to this theoretical framework, observed spin-down rate and luminosity of the source leads to a magnetar-like surface magnetic field estimation that is consistent with the previous estimations by [148].

5.4.3 The Glitch

A glitch in the pulse frequency is observed 25 d after the X-ray outburst of SXP 1062. The source has not shown any spin-up trend during the outburst that may be due to a very short duration of the outburst. Actually, the outburst is displayed only in one of the observations, which has an exposure of about 2.2 ks. As shown in Fig. 5.2 and Table 5.1, the glitch occurred on MJD 56834.5 with a change of pulse frequency $\Delta\nu = 1.28(5) \times 10^{-6}$ Hz and a change of pulse frequency derivative $\Delta\dot{\nu} = -1.5(9) \times 10^{-14}$ Hz/s. In Fig. 5.5, we also show the pulse frequency evolution that is constructed by measuring the slopes of the TOAs (see Fig. 5.2) for time intervals of approximately 30-70 d. Since the occurrence of the glitch does not coincide with the time of the X-ray outburst, it should be associated with the internal structure of the neutron star. SXP 1062 continues to spin-down with a constant rate after the glitch event.

A glitch is a sudden fractional change in frequency that is mostly pursued by a change of spin-down rate of a previously rather stable rotating pulsar. Almost 10 per cent of pulsars are observed to glitch and pulsars of all ages seem to have glitches [172] with fractional change of frequency $(\Delta\nu/\nu)$ ranging from 10^{-11} to 10^{-5} and fractional change of frequency derivative $(\Delta\dot{\nu}/\dot{\nu})$ varying between 10^{-4} and 10^{-1} ([173]; [174]; [175]). The core of a neutron star contains a significant amount of neutron superfluid ([176]; [177]; [178]; [179]; [180]; [181]) therefore, the moment of inertia of the star resides mainly in the core. Moreover, the inner part of the crust lattice also contains an amount of neutron superfluid that carries 10^{-2} of the star's moment of inertia. Coupling time-scales between crustal neutron superfluid and the rest of the crust is typically very long extending from months to years ([182];[183]). For radio pulsars that spin-down due to electromagnetic dipole radiation, it is possible to resolve moment of inertia of the crustal superfluid during the post-glitch ([173]; [174]). Like canonical pulsars, magnetars also exhibit glitches; however, there are some distinguishing characteristics between these two groups. While almost all pulsars are radiatively quiet i.e. they are not accompanied by any burst or pulse profile changes after the glitch ([173]; [174]; see [184]; [185]; [186] for exceptions), magnetar glitches can either be radiatively loud i.e. they can be accompanied by flares,

bursts and/or pulse profile changes; or radiatively quiet [175].

In magnetars, glitches are resolved with high fractional frequency changes of the order of $\Delta\nu/\nu \sim +10^{-5}$ and -10^{-4} [9]. Largest spin-down glitches observed are the glitch of 1E 2259+586 with $\Delta\nu/\nu \sim 10^{-6}$ [187] and the glitch of SGR 1900+14 with $\Delta\nu/\nu \sim 10^{-4}$ within 80 d after a large outburst ([188]; [189]). There are a few net spin-down glitches ([156]; [190]; [191]) together with a large number of spin-up glitches [175]. Large spin-down glitches can be explained by particle outflow from magnetic multipoles during an outburst, while this process induces vortex inflow from the crust. The density of vortex lines are proportional to the superfluid velocity therefore it is proportional to the angular momentum taken from the crust ([189]; [192]). The spin-up glitches can be caused by sudden fractures of the crust and consequently vortex outflow in the crust superfluid [189]. For both cases of spin-down and spin-up glitches, vortex unpinning from the crust occurs and then the vortices creep and re-pin to the crustal nuclei, therefore the post-glitch relaxation should be observed in both cases [193].

Due to the presence of dominant external torque noise, it is not easy to detect these types of glitches for accretion-powered pulsars in X-ray binaries [194]. However, for KS 1947+300 Galloway et al. [195] have discovered a spin-up glitch. KS 1947+300 was spinning up during this glitch, therefore the influence of the external torques is not clear yet; whether the glitch event is associated with internal or external torques. Recently, Ducci et al. [196] have suggested that both glitches and antiglitches are possible for accretion-powered X-ray pulsars, furthermore glitches of binary pulsars should have longer rise and recovery time-scales compared to isolated pulsars since they have pulse periods longer than those of isolated ones.

SXP 1062 is found to be spinning down secularly until MJD 56834 that is 25 d subsequent to the X-ray outburst. Then, the source showed a spin-up glitch with a fractional frequency change of $\Delta\nu/\nu \sim 1.37(6) \times 10^{-3}$ and a fractional change of frequency derivative $\Delta\dot{\nu}/\dot{\nu} \sim 0.3(2)$.

During the secular spin-down of SXP 1062, the spin-down rate is measured to be $-4.29(7) \times 10^{-14}$ Hz/s. If we consider that the observed glitch is due to a torque reversal (i.e. consider it as a frequency jump due to accretion torque) with a similar
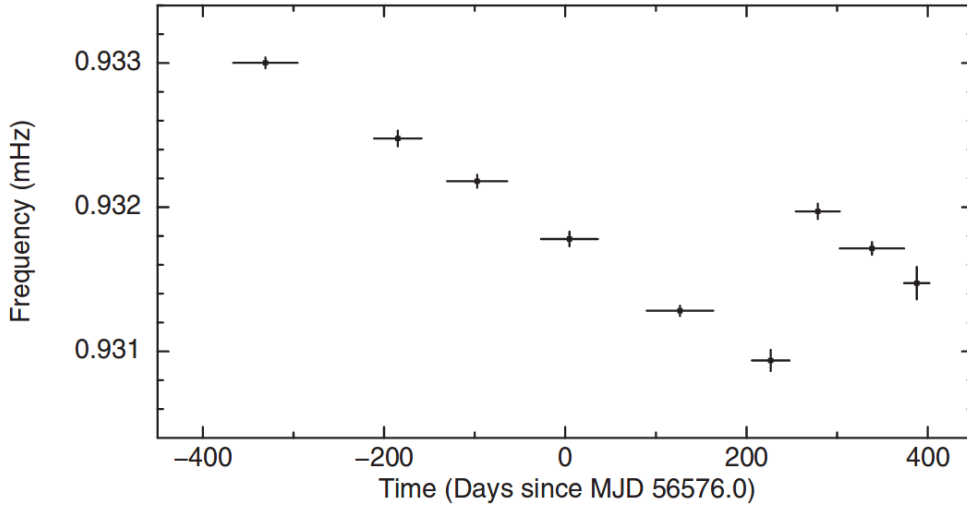
Figure 5.5: Pulse frequency evolution of SXP 1062. Frequencies are calculated from the slopes of linear fits to the TOAs shown in Fig. 5.2. The time intervals of linear fits are represented as x-axis error bars. The frequency jump on MJD 56834.5 is identified as a spin-up glitch event with $\Delta\nu = 1.28(5) \times 10^{-6}$ Hz. The source continues to spin-down after the glitch with a change of frequency derivative $\Delta\dot{\nu} = 1.5(9) \times 10^{-14}$ Hz s^{-1}

magnitude of spin-up rate, upper limit for $\Delta\nu/\nu$ can be estimated to be about $\sim 1.5 \times 10^{-5}$ for a maximum of $\Delta t \sim 4$ d (the time interval between two neighboring observations around the frequency jump) that is two orders of magnitude smaller than the observed $\Delta\nu/\nu$ of the glitch. So, it is unlikely that the glitch is a result of the accretion torques. Furthermore, the ratio of the core superfluid moment of inertia to the crust moment of inertia (I_s/I_c) should be of the order of 10^2 ([197]; [194]). Therefore, the glitch event in SXP 1062 should be associated with the internal structure of the neutron star.

Recently, Ducci et al. [196] discussed observability of glitches in accretion-powered pulsars by using the 'snowplow' model of [198]. In the two-component neutron star model [199], a neutron star consists of two components: the normal component where charged particles (protons and electrons) corotate with the neutron star's magnetic field with moment of inertia I_c and the neutron superfluid with moment of inertia I_s. The rotating superfluid (both in the core and inner crust) is considered to be an array

of vortices that are pinned to the crustal lattice of ions. When the neutron star slows down, a rotational lag is developed between the vortices and the normal component. Eventually, vortices are unpinned and suddenly move out after a certain critical value of rotational lag, leading to a glitch. The time required to build a glitch is inversely proportional to the spin-down rate; therefore, pulsars with higher spin-down rates are expected to glitch more often. Moreover, the coupling time-scales between the crust and core are proportional to the pulse period as $\tau = 10 - 100\, P_s$ ([200]; [201]; [202]). Since SXP 1062 has a long pulse period along with a strong spin-down rate, it is a good candidate for observing such glitches. In accretion-powered pulsars, the time-scales for both glitch rise and decay are suggested to be long; therefore, a glitch would appear as a single jump in frequency leaving the spin- down rate almost unchanged [196]. The jump in pulse frequency can be estimated via [196]

$$\Delta\nu \simeq 2 \times 10^{-5} \frac{Q_{0.95} R_6^2 f_{15}}{M_{1.4}[1 - Q_{0.95}(1 - Y_{0.05})]} \tag{5.11}$$

where $Q[= I_s/(I_c + I_s)]$ is the fraction of superfluid in the neutron star ($Q_{0.95}$ in units of 0.95), Y is the fraction of vortices coupled to normal crust ($Y_{0.05}$ in units of 0.05) and f is the pinning force (f_{15} in units of 10^{15} dyn/cm). The parameter Y represents short time dynamics and approaches 1 for long time-scales (steady state). Assuming a neutron star with a mass of 1.4 $M_\odot$, a radius of 10 km, $f_{15} \simeq 1$ dyn/cm and by using the $\Delta\nu$ value observed for SXP 1062; we find that for a superfluid fraction around 95 per cent the fraction of coupled vortices is around 78 per cent.

Both glitch rise and decay times for SXP 1062 should be of the order of a day or less ($\tau = 10 \check{} 100 P_s \simeq 10^4 - 10^5$ s); however, the sampling of TOAs around the glitch is about 3–4 d. Therefore, we observe neither the rise nor the decay of the glitch, since the glitch rise and decay should have already finished within the observational gaps. Thus for SXP 1062, the observed step-like change in pulse frequency and its magnitude can be qualitatively explained by the model of [196].

SXP 1062 has a strong and steady spin-down rate among accretion-powered X-ray pulsars. Moreover, SXP 1062 is associated with a young SNR with an age of 10-40 kyr ([141]; [140]); therefore, it is a young pulsar spinning down very fast in the remnant. The detection rate of glitches are observed to be higher for younger pulsars [173] and long intervals of steady spin rates are expected to increase glitch possibility

[196]. Therefore, these unique properties of SXP 1062 allows the vortices to creep and pin to the crustal nuclei ([200];[203]). Sudden unpinning of vortices may cause a large glitch event, which is observed in this case with $\Delta\nu/\nu \sim \times 10^{-3}$ being the largest value of fractional frequency jump reported as far. The fractional size of the glitch suggests that I_s/I_c is around 10^2 that corresponds to soft equation of state ([180]; [204]). It is possible to observe a glitch in this source again. In addition, the long pulse period of SXP 1062 makes it possible to reveal glitch rise and crust core coupling time if future observations are sampled closely [205]. Future monitoring of this source with LOFT and NICER can reveal more information about the interior of the neutron star.

CHAPTER 6

GX 1+4

In this Chapter, the timing analysis of GX 1+4 is presented which is based on 90 pointing RXTE-PCA observations of GX 1+4 between 2001 March 3 and 2003 January 31 with a total exposure of 276 ks. A search for for episodic correlations and anti-correlations between the torque and X-ray luminosity is conducted using the CGRO-BATSE X-ray flux and frequency derivative time series between 1991 and 1999. This Chapter only includes the timing analysis part of the original work [206] which is published under the title of "*Comprehensive timing and X-ray spectral analysis of GX 1+4*" in MNRAS journal. The main article also explores variations of spectral parameters both in time and in phase.

6.1   Introduction

Accretion-powered pulsar GX 1+4 was discovered in 1970 with the pulsations of about two-minute period [207]. It showed a strong spin-up during the 1970s [208]. Subsequent to an undetectable low-luminosity state era during the early 1980s, the source was re-detected after it had undergone a torque reversal [209]. After this torque reversal event, GX 1+4 has been usually observed to be spinning down [131]. GX 1+4 is in a low-mass X-ray binary system and its optical counterpart is an M6III-type red giant star V2116 Oph which underfills its Roche lobe ([210]; [211]; [212]). Distance to this system was estimated to be about 4.3 kpc [212]. GX 1+4 is the first example of an accretion-powered pulsar residing in a symbiotic X-ray binary system in which the compact object accretes mass via the dense wind of the M-type giant companion [213]. The presence of a long-term accretion disc around the pulsar was suggested

and standard accretion disc theory ([70]; [164]) was used to explain the pulse period evolution, torque reversal and transition to faint state ([214]; [215]).

The magnetic field strength of GX 1+4 was inferred from two methods: implementing standard accretion disc theory and using marginal evidence of cyclotron resonance scattering feature. With the standard accretion disc theory, the surface magnetic field strength of the pulsar was estimated to be quite high, $\sim 10^{13} - 10^{14}$ G ([214]; [215]). On the other hand, using the relation between the magnetic field and cyclotron line energy, the magnetic field strength was calculated to be rather ordinary amongst accretion-powered pulsars, $\sim 10^{12}$ G ([216]; [217]).

Although the optical companion of GX 1+4 is known, orbital parameters of the system have not been conclusively determined yet. From X-ray measurements of the spin period variations during both spin-up and spin-down era (between 1991 and 1998), an orbital period of 304 d has been suggested ([218]; [219]; [220]). On the other hand, infrared observations of the source have indicated a 1161 d period without any sign of 304 d periodicity [212]. Recently, the 1161 d period has been supported by suggesting a potential neutron star eclipse from the variability of hard (> 17 keV) X-ray emission [221].

Table 6.1: Observation log of GX 1+4

Proposal ID	Number of observations	Total exposure (ks)	Time Range (MJD)
60060	40	120.9	519 74–523 20
70064	40	124.6	523 38–525 93
70065	8	28.9	523 90–525 85
70425	2	1.5	526 62–526 70
Total	90	276.0	519 74–526 70

This Chapter will continue as follows: in Section 6.2, the observations and their data reduction procedure is introduced. In Section 6.3.1, the pulse timing analysis of RXTE-PCA observations and the resulting measurements of pulse frequencies are presented. In Section 6.3.2, the power spectrum of the pulse frequency derivative

fluctuations is shown. In Section 6.3.3, the results of analysis of CGRO-BATSE data for episodic torque luminosity correlations and anti-correlations are demonstrated. In Section 6.4, a discussion over the results of the study is depicted.

6.2 Observations

6.2.1 RXTE Observations

The RXTE was an X-ray satellite that had been launched into low-Earth orbit on 1995 December 30 and operated until 2012 January 5. It had Proportional Counter Array (PCA) composed of proportional counter units (PCUs), each of which had an effective area of 1300 cm^2. The PCA was sensitive to the photons within the 2-60 keV energy range. GX 1+4 was monitored with RXTE-PCA between 2001 March 3 and 2003 January 31. During this time interval, 90 pointing observations were carried out. The total exposure of these observations is around 276 ks while the exposure for each observation varies between 0.5 and 18 ks (see Table 6.1 for details). The data reduction is carried out with the HEASOFT v6.19 software. The data selection is carried out considering the electron contamination to be less than 0.1, offset angle to be less than 0.02° and elevation angle to be greater than 10°. The light curves are extracted from *GoodXenon* mode events with 1s bin time. Then, barycentric correction is applied to the photon arrival times in the light curve. As the active number of PCUs in each observation varies, the count rates are re-corrected with CORRECTLC command as if all five PCUs were operating at the same time.

6.2.2 CGRO-BATSE Observations

Burst and Transient Source Experiment (BATSE) onboard Compton Gamma Ray Observatory (CGRO) consisted of eight detector modules located at the corners of CGRO. These detectors enabled continuous all-sky monitoring of both pulsed and unpulsed sources above 20 keV between 1991 and 2000. BATSE not only continuously monitored daily pulse frequency and X-ray flux changes of persistent and previously known transient accretion-powered pulsars, but also discovered and monitored new

79
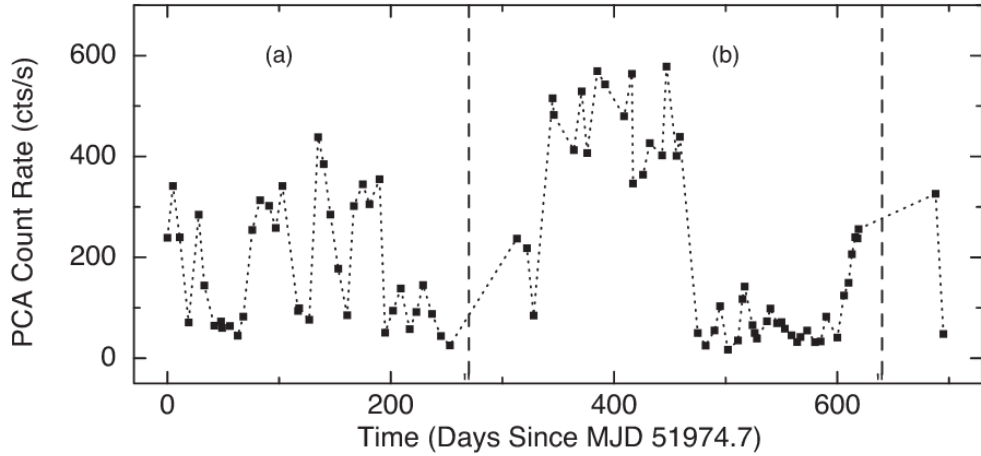
Figure 6.1: 1 d rebinned RXTE-PCA light curve of GX 1+4. Dashed lines indicate two different timing ephemeris: interval 'a' and interval 'b'.

transients [132]. This study makes use of the BATSE 20-60 keV band X-ray flux and pulse frequency derivative time series of GX 1+4 obtained from the ftp site 'gammaray.nsstc.nasa.gov/batse/pulsar/'. These time series cover the time span between 1991 and 1999.

6.3   Timing Analysis

6.3.1   Pulse Timing And Pulse Frequency History

For the timing analysis, we follow the phase coherent timing approach and use barycentric RXTE-PCA light curve between MJD 519 74 and 525 93. In order to search for periodicity in the data, we fold the light curve over trial periods [106]. Using the χ^2 test, we obtain the template pulse profile that gives the maximum χ^2. We create the pulse profiles with 20 phase bins for each observation and represent them in terms of Fourier harmonics [109].

Then, by cross-correlating each pulse with the template pulse profile, we calculate the arrival times of pulses (TOAs). In order to avoid cycle count ambiguity, we construct TOAs within each 50 d and measure the best period of that time span. Then, using the

80

Table 6.2: Timing parameters of GX 1+4 for intervals 'a' and 'b'.

Parameter	Interval a	Interval b
MJD Range	519 74.7-522 27.9	522 88.2–525 93.7
Time span (d)	253.2	305.5
Epoch (MJD)	519 74.0	523 90.0
Frequency (mHz)	7.335 369(8)	7.257 1253(8)
Period (s)	136.3257(2)	137.795(6)
$\dot{\nu}$ (10^{-12} Hz s^{-1})	-2.022(2)	-1.9892(2)
$\ddot{\nu}$ (10^{-19} Hz s^{-2})	0.033(2)	1.240(4)

overlapping time intervals, we align the slopes of TOAs in consecutive time spans. And phase-connected pulse arrival times are fitted by

$$\phi(t) = \phi_0 + \nu_0(t - t_0) + \frac{1}{2}\dot{\nu}(t - t_0)^2 + \frac{1}{6}\ddot{\nu}(t - t_0)^3 + ... \qquad (6.1)$$

where t_0 is the start time of epoch folding; ν, $\dot{\nu}$ and $\ddot{\nu}$ are the spin frequency, its first derivative and second derivative, respectively. Since there is a gap of 60 d within the data between MJD 522 28 and 522 88, we phase connected the pulse arrival times of the source in two different time intervals 'a' ($\simeq 250$ d) and 'b' ($\simeq 300$ d) (as illustrated in Fig. 6.1). We are able to obtain a "representative" timing solution for each interval since it is generated not by fitting all TOAs at once but re-aligning 50d segments (parameters are listed in Table 6.2). We find that the source is spinning down with a rate of $\dot{\nu} \approx -2 \times 10^{-12}$ Hz/s. We present the pulse arrival times and their residuals after the removal of cubic trend for the intervals 'a' and 'b' in Fig. 6.2.

We construct the pulse frequency history (see Fig. 6.3) of the source by using the slopes of linear fits to each of the three consecutive TOAs (approximately 20–30 d). We calculate the error bars of frequency measurements from the uncertainties of the slopes. The pulse frequency measurements of GX 1+4 were previously conducted by [215] for the time span corresponding to interval 'b'. Our measurements are presented together with the measurements by [215] in the lower panel of Fig. 6.3.
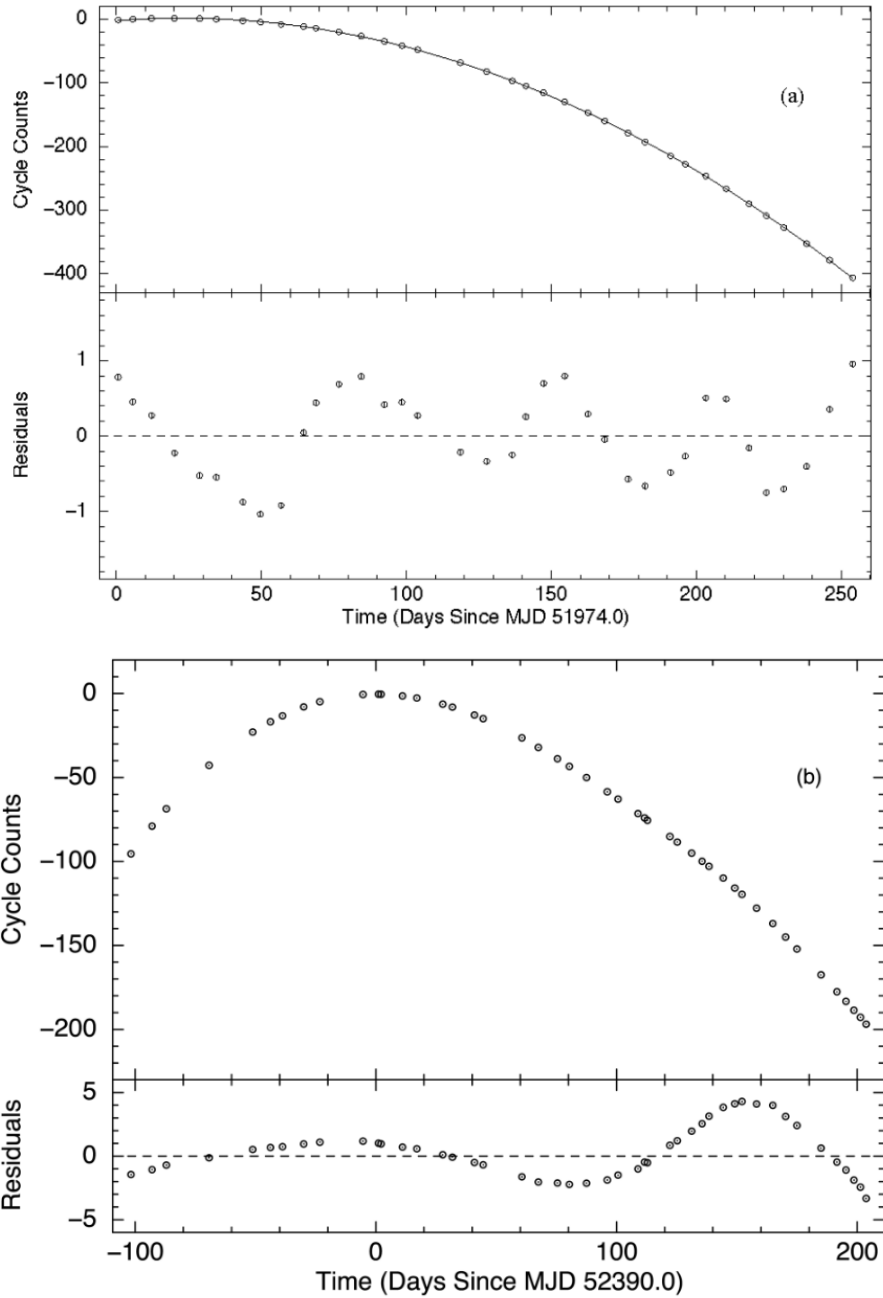
Figure 6.2: Pulse arrival times of GX 1+4. (a) Pulse arrival times of interval 'a' and its residuals after the removal of the third-order polynomial. (b) Pulse arrival times of interval 'b' and its residuals after the removal of the third-order polynomial.

6.3.2 Power spectrum of the pulse frequency derivative fluctuations

In order to investigate torque noise characteristics of GX 1+4, we construct the power spectrum of the pulse frequency derivative fluctuations by employing the root-mean-
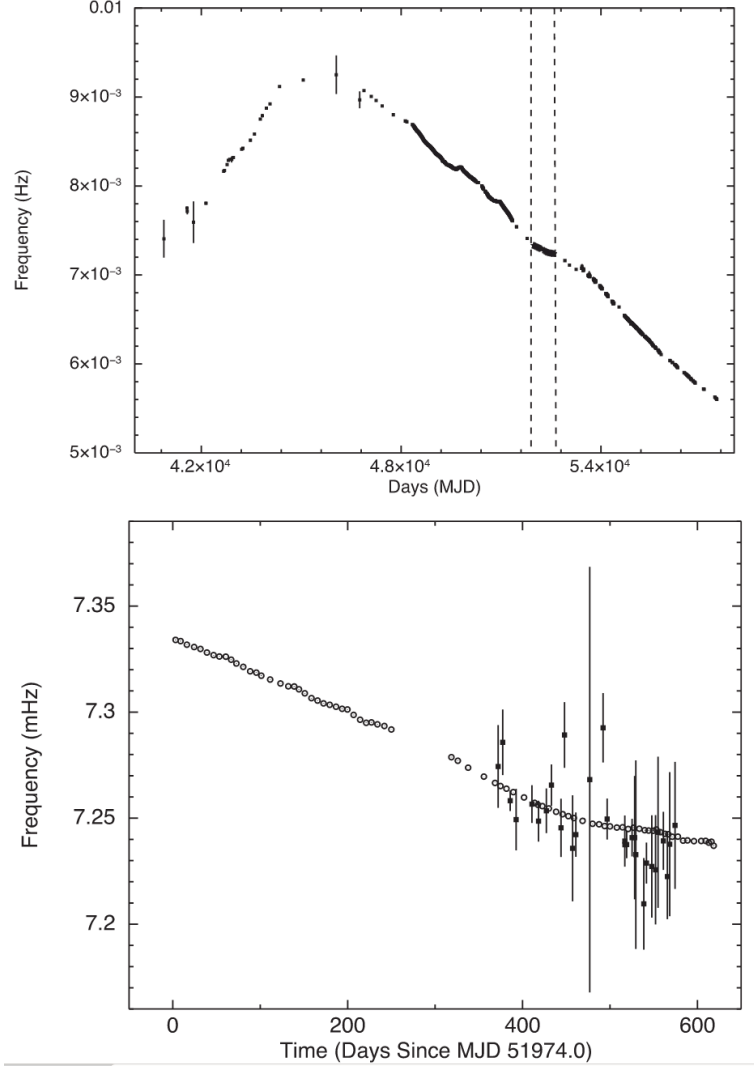
Figure 6.3: Upper panel shows the complete frequency history of GX 1+4 (see [131], and references therein). The frequencies measured in this work are located between the dashed lines. A closer view of this time range is given in the lower panel. Our measurements and the measurements of [215] are represented by empty circles and filled squares, respectively

square (rms) residual technique developed by [114] and [117]. In this technique, mean square residual for the data spanning an interval of length T can be expressed as $S_r T^{2r-1}$, where S_r corresponds to the rth-order red noise strength. The mean square residuals, after removing a polynomial of degree m over a time span T, can be given by

$$< \sigma_R^2(m,T) >= S_r T^{2r-1} < \sigma_R^2(m,1) >_u \qquad (6.2)$$

where $< \sigma_R^2(m, 1) >_u$ s the normalization (proportionality factor) that can be estimated by measuring the variance of residuals by removing the degree of polynomial m for the unit noise strength $S(r = 1)$.
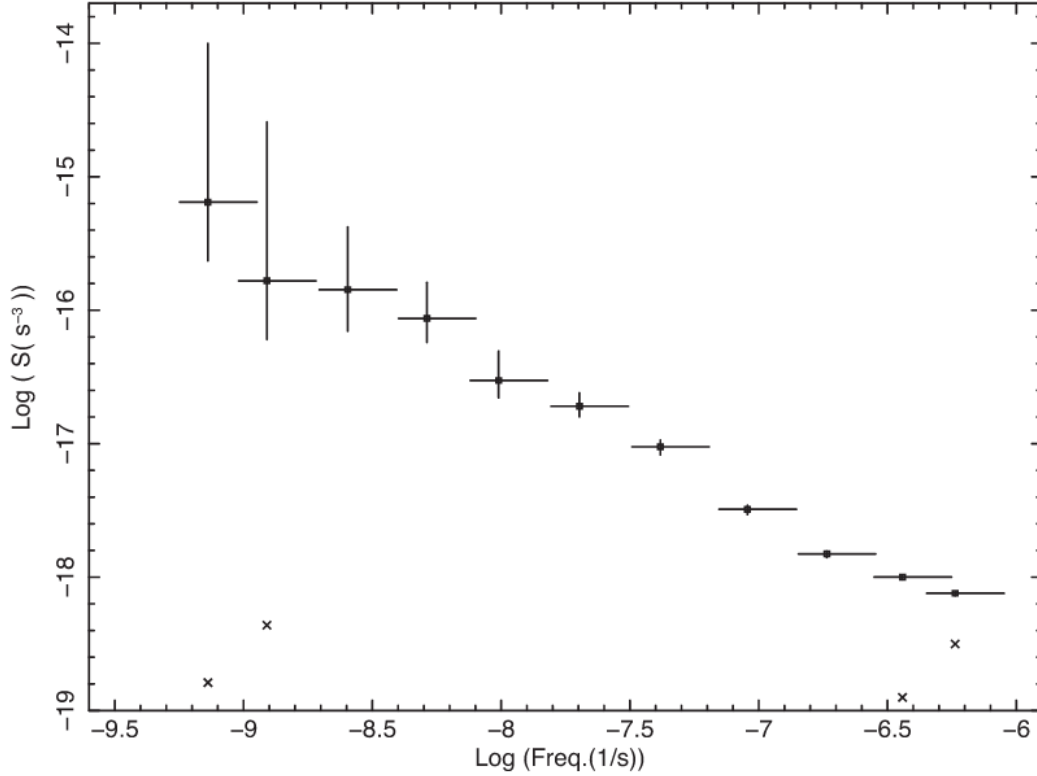
Figure 6.4: Power spectrum of the pulse frequency derivatives of GX 1+4. Crosses indicate the measuremental noise level.

The power spectrum of pulse frequencies was constructed before from BATSE data by [132] It was shown that noise strengths corresponding to pulse frequency derivatives obey the f^{-1} law. Therefore, we simulate time series of GX 1+4 for f^{-1} noise (see [118]). We estimate the normalization of the simulated series by removing quadratic polynomial of degree $m = 2$. After determining the normalization, we estimate noise strengths for different time spans (T, $T/2$, $T/4$, ...). Then, we construct power spectrum of the pulse frequency derivatives by taking the logarithmic average of the noise estimates for each time span and we present the inverse of time spans as frequency in Fig. 6.4.

Our power spectrum of the pulse frequency derivatives is constructed by using all

pulse frequency measurements since 1972, whereas Bildsten et al. [132] used only the measurements between 1991 and 1999. It is evident that the power-law index and noise strengths still agree with the power spectrum estimate presented by [132]. As shown in Fig. 6.4, the power spectrum estimate obeys f^{-1} (or flicker noise) for the frequency interval from 1/44 yr^{-1} to 1/31 d^{-1}. The time-scale of this power spectrum is the longest ever measured for accretion-powered X-ray pulsars. The noise strength level changes between $S = 6.5 \times 10^{-16}$ Hz s^{-2} and $S = 1.0 \times 10^{-18}$Hz s^{-2}.

6.3.3 Episodic torque-luminosity correlations and anticorrelations

Torque–luminosity correlations of GX 1+4 are examined by using the CGRO-BATSE 20-60 keV band X-ray flux and pulse frequency derivative time series. These time series cover a time span of $\sim$ 3000 d lying within the era of long-term spin-down trend of the source.

We systematically search for the X-ray flux and pulse frequency derivative correlations and anti-correlations in $\sim$ 100 − 200 d long intervals. Assuming that the bolometric luminosity is correlated with the pulsed X-ray flux, finding such correlations or anticorrelations will be a direct indication of episodic torque–luminosity correlations and anticorrelations.

We find that the source occasionally enters $\sim$ 100 − 200 d long intervals that show either correlation (Pearson correlation coefficient (PCC)> 0.6) or anti-correlation (PCC $<$ −0.6) between the X-ray lux and pulse frequency derivative. Outside these episodes, there is no significant correlation or anticorrelation between the X-ray flux and pulse frequency derivative (−0.6 < PCC < 0.6). In Fig. 6.5, we present the variation of the Pearson correlation coefficient as a function of time for CGRO-BATSE observations of the source.

In Figure 6.6, frequency derivatives of the source are plotted as a function of the 20-60 keV BATSE pulsed flux for two sample ($\sim$ 180 d long) intervals with mid MJDs of 497 00 and 512 50. These samples are the ones that show the strongest correlation and anticorrelation between the frequency derivative and X-ray flux, respectively. PCC for the plots on the left-hand and right-hand panels of Fig. 6.6 are 0.89 and -0.75
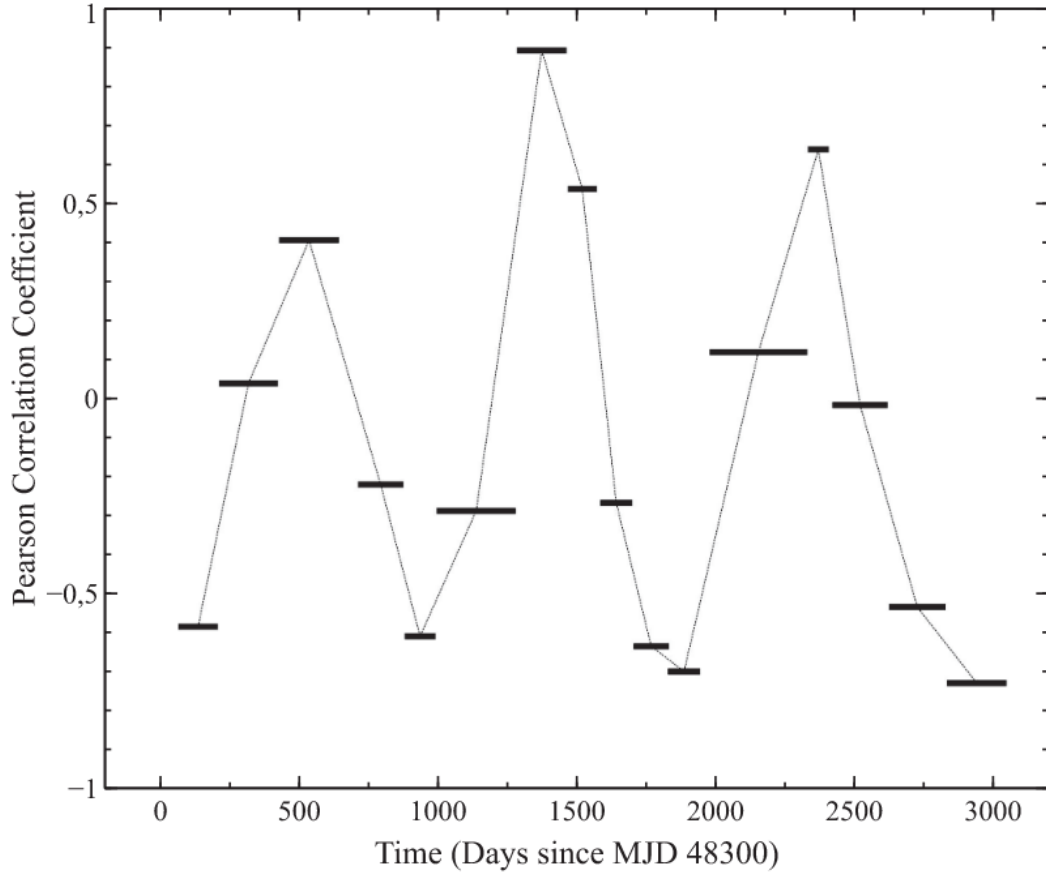
Figure 6.5: Time variation of the Pearson correlation coefficient (PCC) between the frequency derivative and pulsed flux. Correlation analysis is performed for $\sim 100 -$ 200 d long intervals of CGRO-BATSE observations of GX 1+4.

with the corresponding null hypothesis probabilities calculated from the student's t-distribution (two-tailed) of 1.0×10^{-16} and 4.1×10^{-11} respectively.

6.4 Discussion

6.4.1 Timing Solution And Frequency History

GX 1+4 is a persistent accretion-powered X-ray pulsar and a peculiar source residing in a symbiotic X-ray binary. The long-term spin rate evolution of the source has been monitored continuously since it was discovered in the 1970s (see [131], and references therein). From the pulse timing analysis of RXTE-PCA observations, we are
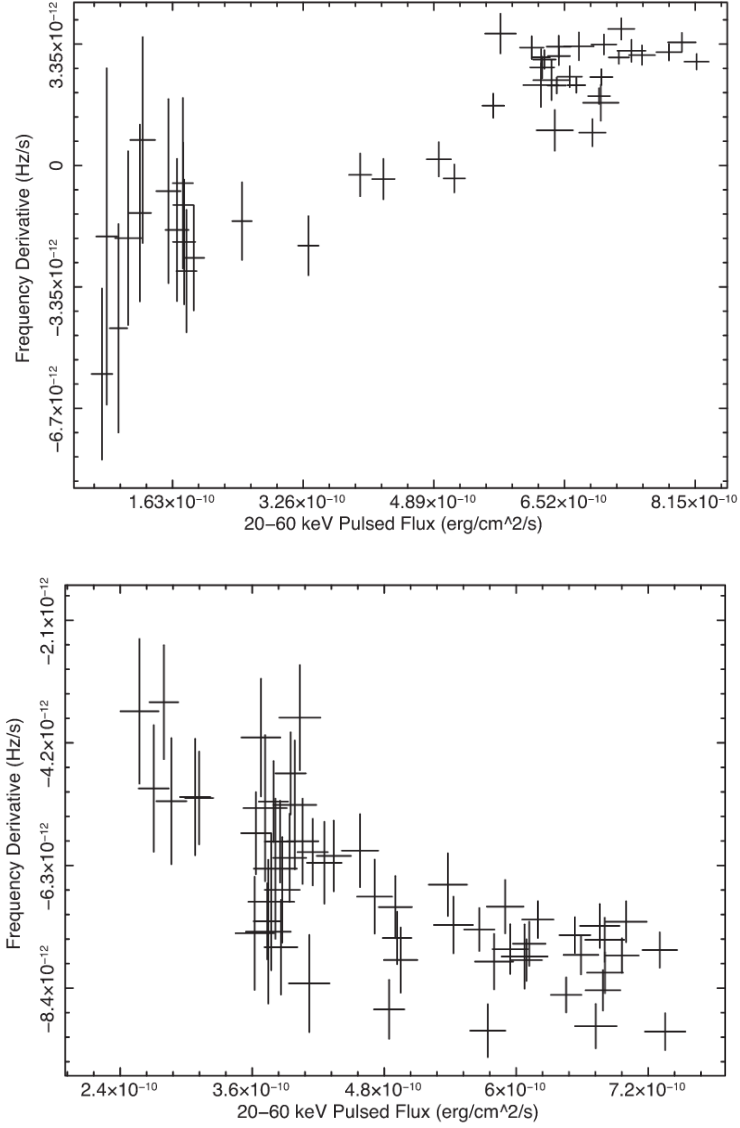
Figure 6.6: Frequency derivative as a function of the 20–60 keV BATSE-pulsed flux for two data sets of ~ 180 days long episodes that show correlation (PCC=0.89, left-hand panel) and anti-correlation (PCC=-0.75, right-hand panel), respectively

able to phase connect the pulse arrival times of the source within two different time intervals of ~ 250 and ~ 300 d long by re-aligning of 50d segments (shown in Fig. 6.2). Therefore, we obtain timing solutions corresponding to these two intervals (see Table 6.2 including interval-wise measurements of the first and second derivatives of pulse frequency). Moreover, using these pulse arrival times, we contributed to long-term pulse frequency history of the source with our new pulse frequency measurements (see Fig. 6.3).

GX 1+4 was a spinning-up source in the 1970s before it underwent a torque reversal in the 1980s. The source was found to show correlation between the spin-up rate and X-ray flux before the torque reversal, which was interpreted as an indication of a persistent prograde accretion disc (see [70] and [164]).

After the source underwent torque reversal, the prograde accretion disc scenario was found to be inconsistent with the spin rate and X-ray flux behaviour of the source. By using CGRO-BATSE data, Chakrabarty et al. [222] found that there is a general anti-correlation trend between the spin rate and pulsed flux (or in other words correlation between the negative of the spin rate and pulsed flux) during the continuous spin-down interval between 1991 and 1995, which is the opposite of expected in the presence of a prograde accretion disc. However, they also reported that the anticorrelation state of GX 1+4 is not perpetual and there is a marginal evidence of a positive correlation between the X-ray flux and spin rate for a prolonged spin-up ($\sim$ 200 d long) interval. A similar spin rate and X-ray flux anticorrelation was also found from the analysis of $\sim$ 600 d long Fermi/GBM and Swift/BAT data [131]. In order to investigate the correlation state from RXTE-PCA observations, we measure spin-down rates for three different time intervals with different flux levels (see Table 3). The measurements indicate that the spin-down rate is scaling up with the flux level; therefore, a general anticorrelation state can be inferred during RXTE observations.

6.4.2 Torque Noise Strength

Torque noise fluctuations and noise strengths of pulse frequency fluctuations have been studied for several accretion-powered X-ray pulsars ([223]; [132]). Red noise (random walk) in pulse frequency fluctuations or white noise in the pulse frequency derivatives are reasonable models for wind accreting X-ray binaries such as Vela X-1, 4U 1538-52 and GX 301-2 [132]. These sources have power spectra with white noise strengths in the range 10^{-20} to 10^{-18} Hz s^{-2}. The persistent long-term spinning-down source 4U 1907+09 ([224]; [225]) also shows random walk in the pulse frequency history [226] with a noise strength of 1.27×10^{-21} Hz s^{-2} for a frequency interval between 1/1300 d^{-1} and 1/75 d^{-1}. For this source, the formation of an episodic transient accretion disc around the neutron star was suggested to explain the random

walk model in the pulse frequency [226].

Accretion-powered pulsars in low-mass X-ray binaries such as Her X-1 and 4U 1626-67 accrete via persistent accretion discs and their pulse frequency time series are also consistent with the random walk model. Their pulse frequency derivatives have white noise strengths in the range 10^{-21} to 10^{-18} Hz s^{-2}. Since the power spectra of these sources lie in a narrow range, the possibility of red noise in the pulse frequency derivative cannot be excluded [132].

Cen X-3 accretes via disc and the noise strength varies from low to high frequencies as 10^{-16}, 10^{-18} Hz s^{-2} [132]. The power-law index of the power spectrum in this system is ~ -1, which implies that disc accretion dominates at short time-scales.

OAO 1657-415 has a power-law index of $\simeq 0$ with a noise strength of 10^{-17} Hz s^{-2} [194]. This source also shows marginal correlation with the spin-down rate and X-ray luminosity [227].

X Per has the lowest noise strength amongst accretion-powered pulsars in high-mass X-ray binaries with 10^{-21} to 10^{-23} Hz s^{-2} for frequencies between 1 yr^{-1} and 1/35 yr^{-1} [228]. The steep power-law index in the pulse frequency derivative indicates that it could have a transient accretion disc.

SAX J2103.5+4545 has the steepest power-law index with 2.13 amongst high-mass X-ray binaries [229]. The steep power-law index suggests that accretion via accretion disc at shorter time-scales possesses low timing noise and therefore power density spectrum becomes steeper compared to the other persistent high- mass X-ray binaries.

In GX 1+4, we observe flickering noise (f^{-1}) that agrees with the power spectrum estimate of Bildsten et al. [132]. It is important to note that we extend the estimate for a time-scale ranging from 31 d to 44 yr. Thus, we describe a noise process for the longest time-scale amongst accretion-powered X-ray pulsars. We find that the noise strength level of the source changes between $S = 6.5 \times 10^{-16}$ Hz s^{-2} and $S = 1.0 \times 10^{-18}$ Hz s^{-2}.

The torque noise power spectrum of GX 1+4 has a unique trend amongst accretion-powered pulsars, showing an f^{-1} power law trend in the longest time span. In other

words, timing noise increases with time. Recently, Ilkiewicz et al. [221] supported the orbital period of 1162 d using hard (> 17 keV) X-ray observations. This orbital period was originally suggested by [212] using radial velocity measurements from infrared observations. Hinkle et al. [212] found the projected semi-major axis of the orbit as $a/c\,sini \sim 773$ lt s. The effect of Doppler shifts due to the orbital modulation on pulse frequency time series is thus $\delta\nu \sim \frac{2\pi}{P_{orb}}\frac{1}{P_{spin}}\frac{a}{c}sini \sim 3.7 \times 10^{-7}$ Hz. Using the torque noise spectrum (see Fig. 6.4), the noise strength at the frequency corresponding to the orbital period $(1/(1162 \times 86400) = 0.9 \times 10^{-9}$ Hz) is $S \sim 3 \times 10^{-17}$Hz s^{-2}; we estimate the deviation on frequencies due to the noise process as $\sqrt{\Delta\nu^2} = \sqrt{ST} = 5.5 \times 10^{-5}$, which is two orders of magnitude greater than Doppler shifts expected due to orbital modulation. Therefore, it is not possible to resolve DOPPLER shift modulations in pulse frequency time series since the noise process dominates. Moreover, ~ 700 d observation time of RXTE is short compared to the suggested orbital period. Continuous monitoring of the source using future observatories such as LOFT [230] might be useful to resolve Doppler shift modulations from pulse arrival data and obtain orbital parameters of the system from X-ray observations.

6.4.3 Episodic correlations and anticorrelations between the X-ray flux and spin rate

In contrast to previous studies that concentrate on searching for 'general' correlation or anticorrelation states between the X-ray flux and spin rate ([222]; [231]; [131]), we search for episodic correlations and anticorrelations on shorter time-scales ($\sim 100 - 200$ d long) by using CGRO-BATSE measurements. We find that the correlation state of GX 1+4 seems to change on $\sim 100 - 200$ d long intervals (see Fig. 6.5). Furthermore, the correlation and anticorrelation intervals do not show significant X-ray flux changes compared to uncorrelated intervals. Still we might argue that the correlation and anticorrelation intervals might be indications of transient accretion disc formation (either prograde or retrograde) and episodic variation of accretion geometry without significant X-ray flux variations. From Fig. 6.5, we also note that the variation of the Pearson correlation coefficient has a period of about 1000 d. The Flicker-type noise process suggests that the torque events are correlated or at least

Table 6.3: RXTE-PCA spin rate measurements for the intervals with different flux levels.

	Interval 1	Interval 2	Interval 3
MJD Range	51974.7-52227.9	52288.2-52343.6	52450.6-52593.7
Time span (d)	253.2	146.4	143.1
$\dot{\nu}$ (10^{-12} Hz s^{-1})	-2.0585(3)	-2.3860(7)	-0.8334(8)
$3-20$ keV unabsorbed flux (10^{-10} erg cm^{-2} s^{-1})	6.22(2)	9.90(3)	2.21(1)

carries a memory from past history. This periodicity of the correlation states is consistent with the proposed orbital period of 1162 d ([212]; [221]) suggesting that the alteration of the states of positive and negative correlation states continues for several decades of orbital cycles. The accretion process in GX 1+4 is unique as it is qualitatively seen from correlation- anticorrelation episodes and torque noise power-law trend. Future monitoring observations of GX 1+4 will be useful to further understand the torque–X-ray luminosity relation.

CHAPTER 7

X PER

This Chapter describes the timing and noise strength analysis of X Per based on 4.5 years RXTE observation journey between 1998 July 1 and 2003 February 17. A further expansion of frequency history is also performed by making use of INTEGRAL observations. The relation between spin frequency derivative and X-ray luminosity is examined. This study only covers the pulse timing analysis part of the main article "*Timing studies of X Persei and the discovery of its transient quasi-periodic oscillation feature*" published in MNRAS which further illustrates the discovery of Quasi-periodic oscillations of ~ 0.2 Hz [228].

7.1 Introduction

From *Ariel 5* and *Copernicus* observations, X Persei (X Per; 4U 0352+309) has been revealed as a persistent low-luminosity accreting pulsar with a pulse period of ~ 836 s [232]. The neutron star in the binary system has a wide orbit around a Be-type star with an orbital period of ~ 250 d and an eccentricity of ~ 0.11 [233].

The binary orbit of the system is wide and rather circular, such that the X-ray pulsar does not pass through the equatorial disc of the Be star. Therefore, X Per does not exhibit Type I outbursts near periastron passages, despite the fact that such outbursts are typical of most Be X-ray binary systems. Taking into account the observed X-ray luminosities ($L_x \sim 10^{35}$ erg/s) of the system, Delgado-Marti et al. [233] have suggested that accreting matter is supplied by a slow (~ 150 km/s) and dense wind, possibly originating from the equatorial disc around the companion star.

The long-term pulse-period variation of the source has been monitored since the 1970s using observations from various X-ray observatories ([234]; [235]; [236];[237]; [238]; [233]; [239]). Before 1978, X Per was spinning up with a rate of $\dot{P}/P \sim 1.5 \times 10^{-4}$ yr^{-1}. Between 1978 and 2002, the source was in a long-term spin-down episode with a rate of $\dot{P}/P \sim 1.3 \times 10^{-4}$ yr^{-1}. After 2002, it was found that the spin rate changed sign again, as the source was found to spin up with a rate of $\dot{P}/P \sim -3.6 \times 10^{-4}$ yr^{-1}. This is significantly higher in magnitude compared to that of the previous spin-up episode before 1978.

In the following sections, the results of the timing analysis of X Per using observations from the RXTE-PCA and from the INTEGRAL Soft Gamma-Ray Imager (ISGRI) are shown. In Section 7.2, the used observations and the data reduction procedures are described. In Section 7.3 and 7.4, the timing analysis results and the discussion are depicted.

7.2 Observations

7.2.1 RXTE Observations

The PCA onboard the RXTE had five identical co-aligned proportional counter units (PCUs; [129]; [240]). Each PCU had an effective area of approximately 1300 cm^2. The PCA was able to detect photons that had energies between 2 and 60 keV, with a spectral resolution of 18 per cent at 6 keV and a field of view (FOV) at full width at half-maximum (FWHM) of $\sim 1°$. The number of active PCUs during the observations of X Per varied between one and three. Data from all the available PCUs are used in this analysis and the count rates shown in Fig. 7.1 are the values corrected as if five PCUs were operational. X Per was observed by the RXTE between 1998 July 1 and 2003 February 17. The exposures of the individual pointed observations vary between 2 and 15 ks. The total exposure of 148 pointings adds up to ~ 793 ks (see Table 7.1 for details). We extract light curves of the source with 0.1-s time binning in the $3 - 20$ keV energy band using the GoodXenon mode events from the PCA.

The HEASOFT v.6.13 software is used for the PCA data analysis. Only the data

Table 7.1: List of RXTE-PCA observations.

Proposal ID	Exposure (ks)	Number of pointings	Time (MJD)
30099	252	56	50995 - 51406
40424	60	14	51420 - 51597
50404	58	12	51634 - 51940
60067	398	58	52000 - 52687
60068	25	8	52094 - 52398

corresponding to times when the elevation angle is greater than $10°$, when the offset from the source is less than $0°.02$ and when the electron contamination of PCU2 is less than 0.1 are analysed. The latest background estimator models supplied by the RXTE Guest Observer Facility are used to extract background spectra and light curves. These background subtracted light curves are corrected to the barycentre of the Solar system as well as for binary motion using the orbital parameters of X Per (see table 2 of [233]).

7.2.2 INTEGRAL Observations

The Imager onboard the INTEGRAL Satellite (IBIS) is a coded mask instrument optimized for high angular resolution (12 arcmin at FWHM; [241]). As a consequence of the large FOV ($8°.3 \times 8°.0$ fully coded, $29° \times 29°$ zero response) of IBIS observations and the dithering strategy of INTEGRAL observations, sky coverage is good and the exposure times of detected sources reach up to millions of seconds. The IBIS consists of two detector layers operating in different energy bands. The data analysed in this study are obtained from the upper layer, the INTEGRAL-ISGRI, which operates in the energy range 15 keV - 1 MeV, and has a time resolution of $61\mu s$.

When the offset of the source of interest increases, the coding factor decreases, resulting in increased uncertainties in the images, flux values and spectra. Therefore, it is not recommended to include in the analysis observations in which the source lies outside the 50 per cent partially coded FOV ($19° \times 19°$). Because X Per is a bright
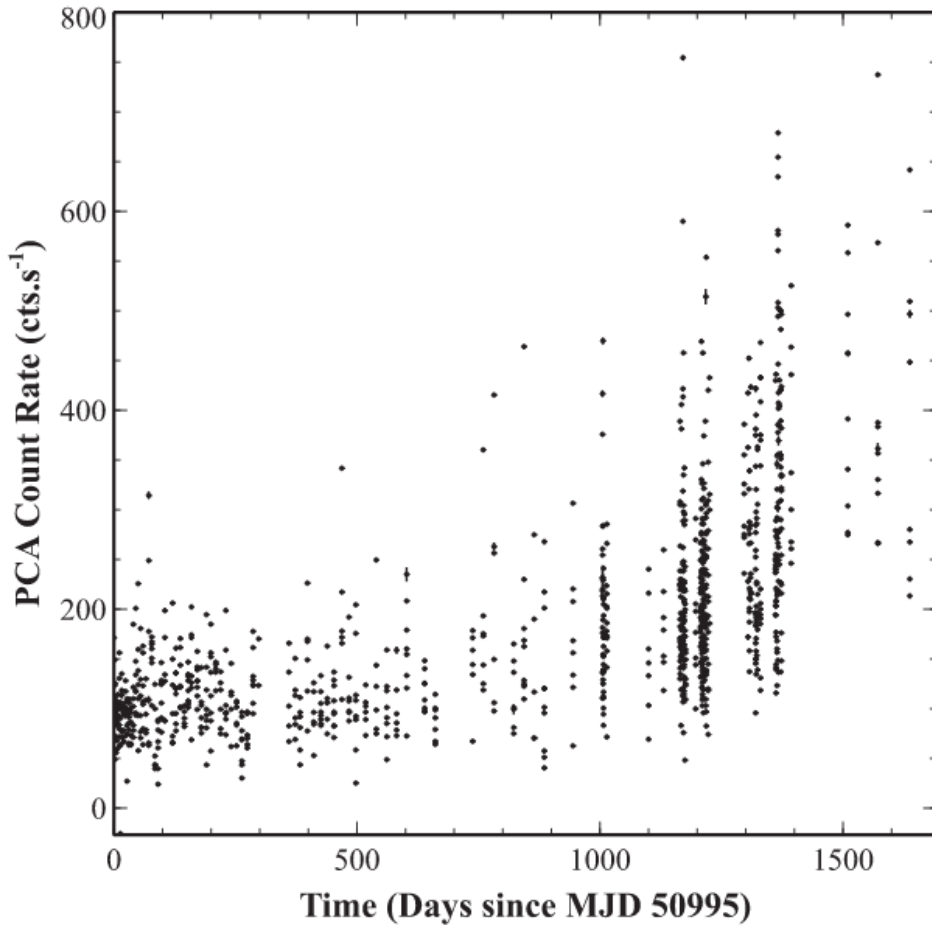
Figure 7.1: The 837-s binned light curve obtained from RXTE-PCA (3–20 keV, corrected for five PCUs) observations

source, its flux is confidently determined even when its position is in the partially coded region. Consequently, the selection criteria for INTEGRAL observations are an off-axis angle of less than $10°$ and ISGRI good times of more than 1 ks. The publicly available pointing observations between MJD 53069 and 55451 (2004 March 5-2010 September 12) reach a number of 766 science windows (SCWs), each having typical durations of 2-3 ks. These observations have been analysed previously by [239], but in this study we present a reanalysis of these observations in order to measure pulse periods using a different technique, as described in Section 7.3.1.

The latest version of the standard data analysis software OSA v.10.0 is used for pipeline processing. Images in two energy bands (20–40 and 40–60 keV) are gen-
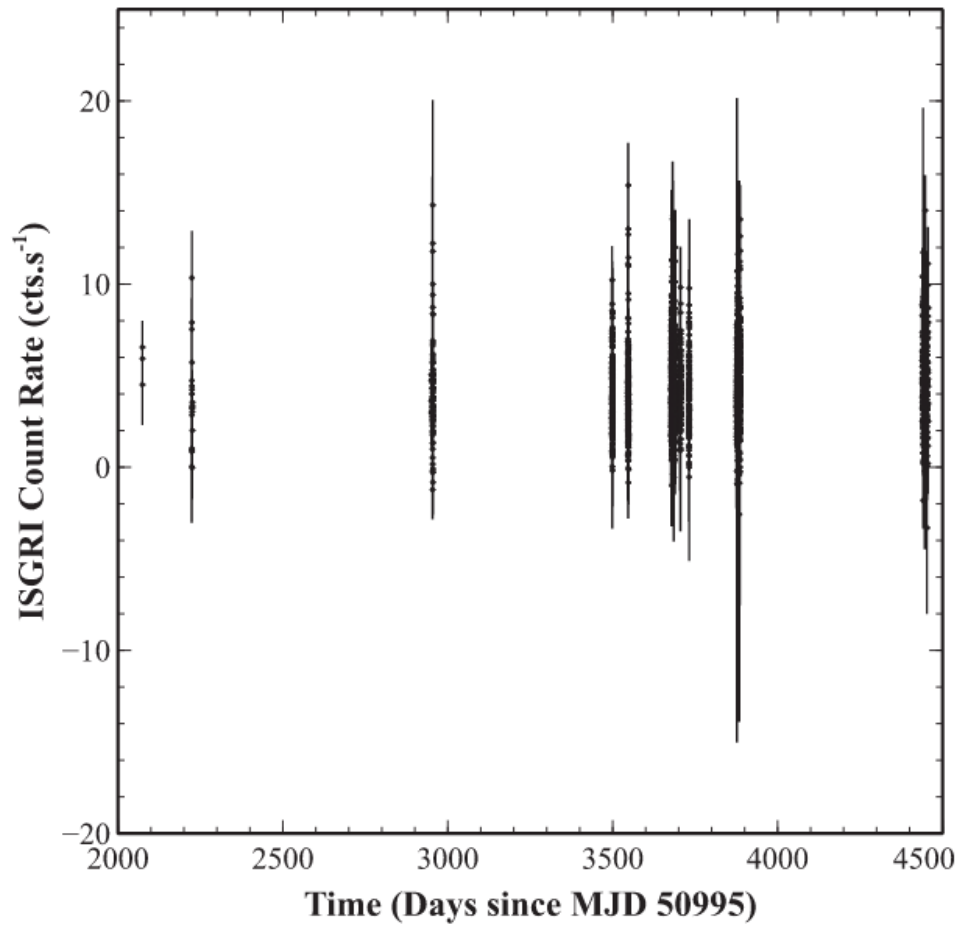
Figure 7.2: The 837-s binned light curve obtained from INTEGRAL IBIS-ISGRI (20-40 keV) observations

erated from IBIS-ISGRI data with an input catalogue consisting of strong sources in the FOV: Crab, 3C 111, NGC 1275, IGR J02343+3229, XY Ari, 1H 0323+342,RX J0440.9 +4431 and X Per. Background maps provided by the ISGRI team are used for background correction. The 10-s binned light curves are generated by the tool II_LIGHT and corrected to the Solar system barycentre. The effective exposure of the corrected IBIS-ISGRI light curve of X Per is around 2 Ms. The resulting light curves are also corrected for the binary motion using the orbital parameters of X Per (see [233]).

7.3 Timing Analysis

We use 0.1-s time binned RXTE-PCA and 10-s time binned INTEGRAL light curves, as described in Sections 7.2 and 7.2.2, for the timing analysis. Fig. 7.1 and 7.2 presents overall 837-s binned RXTE -PCA and INTEGRAL light curves of the source, respectively.

7.3.1 Pulse Timing

In order to measure the pulse periods of X Per, we fold time series on statistically independent trial periods [106]. We construct template pulse profiles by folding the data on the period corresponding to maximum χ^2. Pulse profiles consisting of 20 phase bins are represented by their Fourier harmonics [109]. Fig. 7.3 shows a typical pulse profile and the corresponding power spectrum in terms of harmonic number.
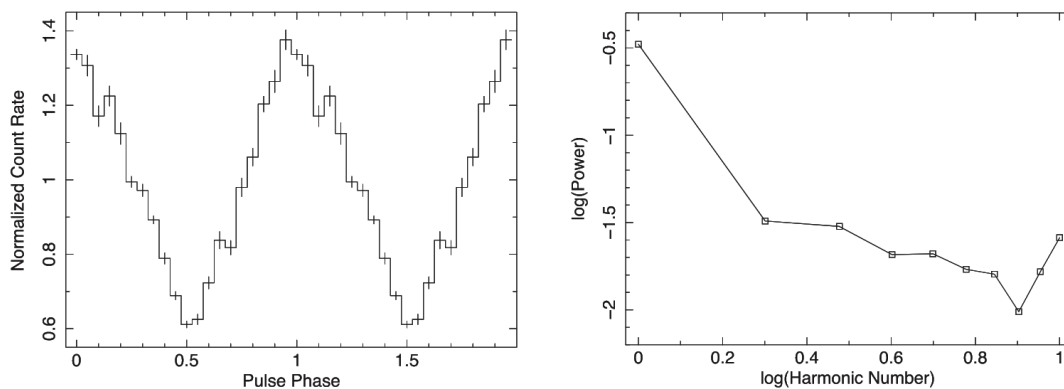
Figure 7.3: A typical pulse profile (left) obtained from RXTE-PCA and its power spectrum (right) in terms of harmonic number.

We have connected in phase all pulse arrival times of the RXTE observations over a 1550-d time-span. In the phase-connection process, we construct pulse arrival times for a time-span where the maximum phase shift is less than 1. In this way, we avoid cycle count ambiguity. This time-scale for X Per is around 220 d. We divide the total time-span into eight time intervals, each around 220 d. Then, we measure pulse arrival times with respect to the best period corresponding to that time interval. We align the slopes of the pulse arrival times in overlapping time intervals. The pulse

98

arrival times thus measured are presented in the upper panel of Fig. 7.4.

In order to see the effect of pulse shape fluctuations, we estimate pulse arrival times using first, second, fifth and tenth harmonic numbers. Analysing each set in the same way, we obtain residuals consistent with each other within the 1σ level. Therefore, we conclude that pulse shape variations do not cause drastic changes in the pulse timing analysis.

The phase-connected pulse arrival times in Fig. 7.4 are fitted to the fifth-order polynomial,

$$\delta\phi = \delta\phi_0 + \delta\nu(t - t_0) + \sum_{n=2}^{5} \frac{1}{n!}\frac{d^n\phi}{dt^n}(t - t_0)^n \tag{7.1}$$

where $\delta\phi$ is the pulse phase offset obtained from pulse timing analysis, t_0 is the mid-time of the observation, $\delta\phi_0$ is the residual phase offset at t_0, $\delta\nu$ is the correction of pulse frequency at time t_0 and $d^n\phi/dt^n$ for $n = 2, 3, 4$ and 5 are the first-, second-, third- and fourth-order derivatives of pulse frequency.

With only the statistical errors on the arrival phases, χ^2 per degree of freedom, which is 9.5, is not acceptable. Systematic errors or short-term variations not captured in the fifth-order polynomial could be responsible. The errors have been multiplied by a factor of 3 such that the reduced χ^2 is 1, in order to obtain errors on the polynomial fits to the longer-term variations. Pulse arrival times (pulse cycles) and the residuals of the fit after removal of the fifth-order polynomial trend are shown in Fig. 7.4. Table 7.2 presents the timing solutions for X Per between MJD 50995 and 52562.

In order to measure pulse frequencies, we fit a linear model to arrival times from $\sim 20 - 30$ d intervals. The slopes of these linear fits give us estimates of the pulse frequency values at the mid-times of the corresponding intervals. Fig. 4 presents the resulting pulse periods of the source, together with the previous pulse period measurements of the source (see references in [239]). In Fig. 7.5, we do not include measurements from RXTE and INTEGRAL by [239], because the values of their measurements are not reported numerically. However, when we compare the scanned values in fig. 2 of [239], it is seen that our measurements are in agreement with theirs. Table 3 presents our pulse period measurements.

For the timing analysis of INTEGRAL observations, we use 10-s binned background-
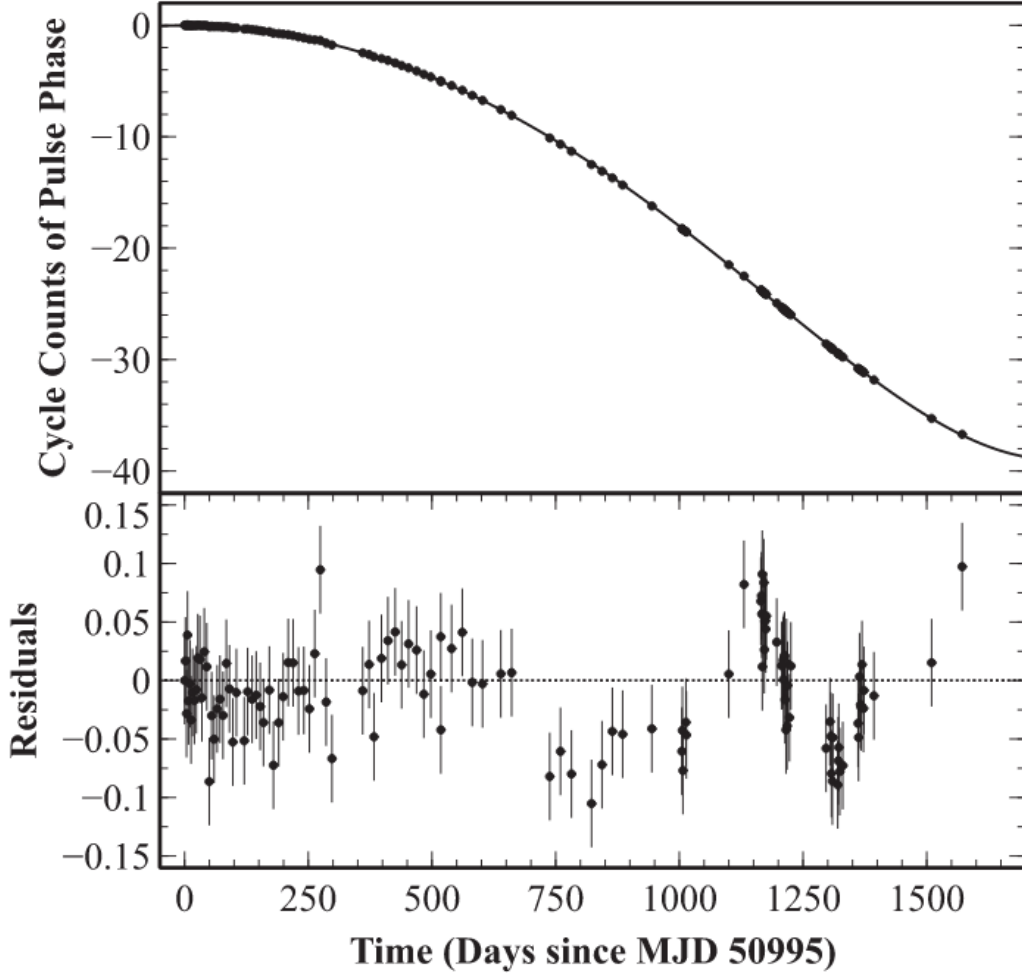
Figure 7.4: Pulse arrival times and their residuals after a fifth-order polynomial fit obtained from RXTE-PCA observations.

corrected 20–40 keV IBIS-ISGRI light curves of the source. From the light curves that have $\sim 7 - 10$ d time-spans, we measure the best pulse frequency by folding the light curve on statistically independent pulse frequencies. Then, we estimate the pulse arrival times by constructing master and sample pulses, as described above for the RXTE analysis. From the slopes of the pulse arrival times, $\delta\phi = \delta\nu(t - t_0)$, we obtain corrections to the pulse frequencies. In Fig. 7.5 and Table 7.3, we present pulse periods obtained from INTEGRAL observations.

We measure pulse frequency derivatives by fitting quadratic polynomials to ~ 200-d long stretches of pulse arrival times from RXTE-PCA observations. The quadratic coefficients of the fits give the pulse frequency derivatives. The corresponding $3 - 20$

Table 7.2: Timing solution for X Per between MJD 50995 and 52562.

Parameter	Value
Epoch (MJD)	50995.038(1)
Timing parameters at t_0:	
Spin frequency (Hz)	$1.19379(9) \times 10^{-3}$
Spin Period (s)	837.666(6)
$\dot{\nu}$ (Hz s^{-1})	$-5.5(3) \times 10^{-15}$
$\ddot{\nu}$ (Hz s^{-2})	$6.6(6) \times 10^{-23}$
$\dddot{\nu}$ (Hz s^{-3})	$-3.6(9) \times 10^{-30}$
$\ddddot{\nu}$ (Hz s^{-4})	$9(2) \times 10^{-38}$

keV X-ray flux values are calculated by modelling each corresponding spectrum with an absorbed blackbody and power-law model, a model previously used for this source [239]. In Fig. 7.8, we present the frequency derivatives and the corresponding flux measurements as a function of time, and the frequency derivative values as a function of unabsorbed $3 - 20$ keV X-ray flux.

7.3.2 Power Spectra of Pulse Frequency Derivatives

In order to compare the torque fluctuations of X Per with other accreting X-ray pulsars, the power density spectrum for the pulse frequency variations is constructed. The red noise power density and associated random walk noise strengths are obtained using the technique developed by [242] and [117]. Some important properties are summarized here. For the rth-order red noise with strength S_r, the mean square residual for the data spanning an interval with length T is proportional to $S_r T^{2r-1}$.

The expected mean square residual, after removing a polynomial of degree m over an interval of length T, is given by

$$< \sigma_R^2(m,T) >= S_r T^{2r-1} < \sigma_R^2(m,1) >_u \qquad (7.2)$$

where $< \sigma_R^2(m,1) >_u$ is the proportionality factor that can be estimated by measuring the variance of residuals by removing the degree of polynomial m for unit noise
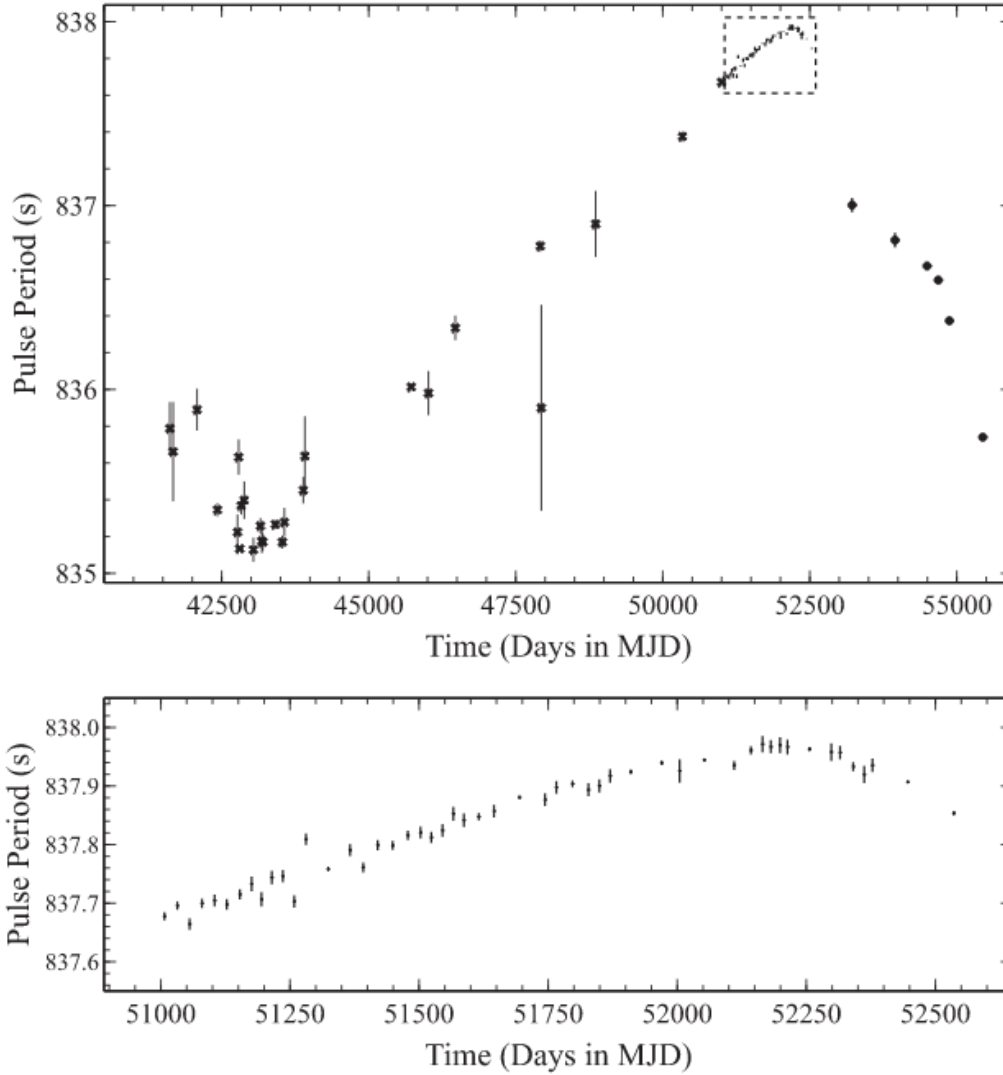
Figure 7.5: The top panel shows the pulse period history of X Per. Pulse periods denoted by crosses are previous measurements obtained from various observatories (see references in [239]). The solid circles represent INTEGRAL measurements in this work. Other data points enclosed in the dashed rectangle are RXTE-PCA measurements of this work. The bottom panel shows a closer view of the pulse period evolution obtained from RXTE-PCA observations.

strength (S_1). We estimate this factor by simulating time series for the rth-order red noise process for a unit noise strength (S_1) for X Per observations. Our expected proportionality factors are consistent with those obtained by direct mathematical evaluation ([117]; see also [114]).

Table 7.3: Pulse periods of X Per measured in this work. The numbers in parentheses indicate the uncertainties in the least significant figures. Pulse periods with superscript ^{a} are measured from INTEGRAL observations.

Epoch (MJD)	Pulse period (s)	Epoch (MJD)	Pulse period (s)	Epoch (MJD)	Pulse period (s)
51006.9	837.678(7)	51502.8	837.82(1)	52142.7	837.961(7)
51031.8	837.696(7)	51523.8	837.812(9)	52165.2	837.97(1)
51055.7	837.66(1)	51545.5	837.82(1)	52181.3	837.97(1)
51079.5	837.700(8)	51566.4	837.85(1)	52199.2	837.97(1)
51104.1	837.70(1)	51586.9	837.84(1)	52213.5	837.97(1)
51127.7	837.698(9)	51615.7	837.847(6)	52256.0	837.963(3)
51153.0	837.715(9)	51645.1	837.86(1)	52298.4	837.96(2)
51175.8	837.73(1)	51694.5	837.881(3)	52315.3	837.96(1)
51194.9	837.71(1)	51743.9	837.88(1)	52340.8	837.933(8)
51214.8	837.74(1)	51765.9	837.90(1)	52362.1	837.92(1)
51236.3	837.74(1)	51797.3	837.904(6)	52378.2	837.94(1)
51258.3	837.70(1)	51828.1	837.89(1)	52446.6	837.907(2)
51281.1	837.81(1)	51849.1	837.90(1)	52535.8	837.854(4)
51323.9	837.758(4)	51870.0	837.92(1)	53219.2^a	837.00(4)
51366.4	837.79(1)	51909.9	837.924(4)	53949.3^a	836.81(4)
51392.0	837.761(8)	51969.8	837.939(4)	54494.0^a	836.67(2)
51419.9	837.799(9)	52004.7	837.93(2)	54684.5^a	836.595(4)
51448.8	837.798(8)	52052.1	837.944(3)	54873.8^a	836.37(2)
51478.3	837.816(8)	52110.4	837.935(8)	55441.1^a	835.7402(3)

We obtain noise strengths at lower frequencies as $f = 1/T_{max}$, where T_{max} is the maximum time-span of the pulse frequency history, from the residuals of pulse frequencies by removing their linear trends. For the higher frequencies, we have $f_n = n/T_{max}$, where n is a positive integer and we remove quadratic trends from the pulse arrival times obtained from RXTE data.

In order to check whether noise strengths are stable or not, we estimate an alternative

power spectra by removing quadratic trends in the pulse frequency at longer time-scales and cubic trends in pulse arrival times at shorter time intervals.

In Fig. 7.6, we present power spectra estimates (or noise strengths) with respect to frequency $f = n/T$ (or reciprocal of the time-scale). We find that both power spectra are consistent with each other in terms of the average noise strength S_r and the slope of the power spectra, -0.85 to -1.47, with a noise strength $10^{-20} - 10^{-23}$ Hz s^{-2} for frequencies between 1/35 and 1 yr^{-1}.
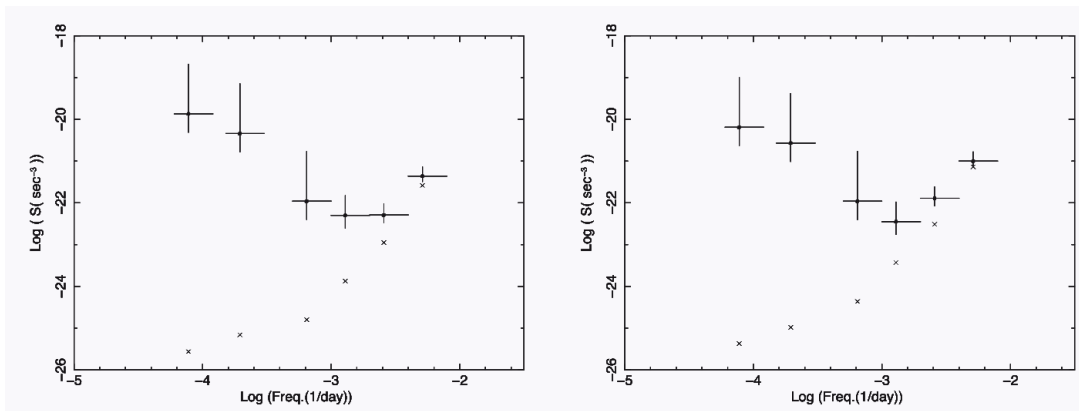
Figure 7.6: Power spectra estimated with respect to frequency obtained by removing (left) quadratic trends and (right) cubic trends. The crosses represent the power resulting from measurement noise.

7.3.3 Pulsed Fraction

We investigate the pulsed fraction variation of X Per for all the available RXTE-PCA data between MJD 50995 and 52687 in the $3 - 20$ keV energy band. Using the timing solution stated in Table 7.2, we extract 671 individual pulses of the source. Then we calculate the pulsed fraction and the mean count rate of each pulsation. The pulsed fractions are calculated with the standard definition,

$$\text{Pulsed Fraction} = \frac{p_{max} - p_{min}}{p_{max} + p_{min}} \tag{7.3}$$

where p_{min} and p_{max} refer to the minimum and maximum counts of the pulse, respectively. The pulsed fractions are then rebinned according to the mean count rate of the

pulsations. The results indicate that the pulsed fraction of the source correlates with the mean count rate (see Fig. 7.7).
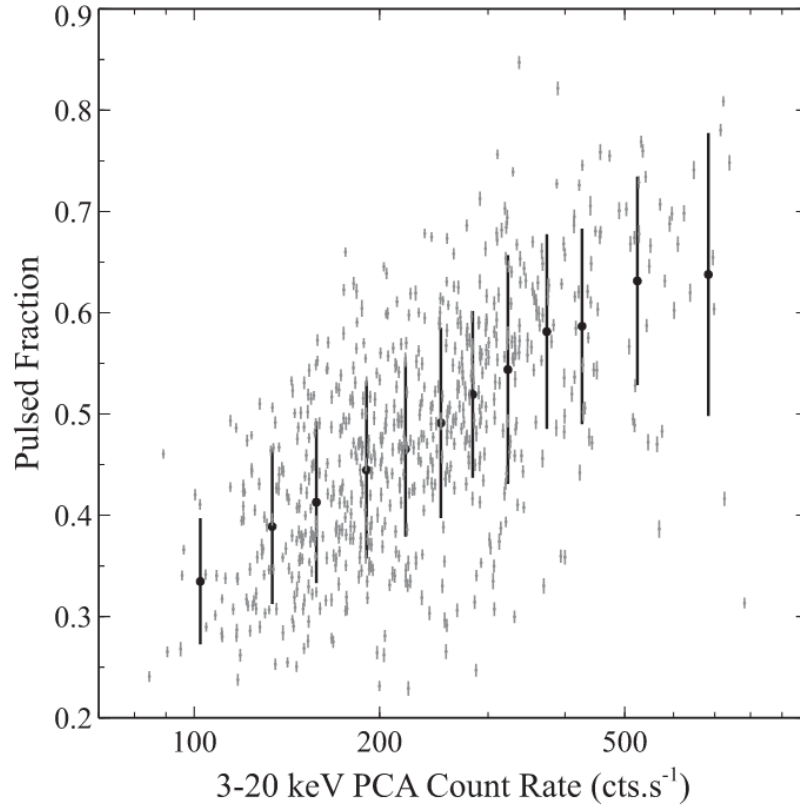
Figure 7.7: Variation of the pulsed fraction with the mean count rate of pulsations. The grey data points are the unbinned results, whereas the black data points are the results rebinned according to the count rates.

7.4 Discussion

In this study, we present our results of a timing analysis of RXTE and INTEGRAL observations of X Per. First, using the cross-correlation technique, we add new measurements to the pulse period history presented by [239]; see Table 7.3.

From the right panel of Fig. 7.8, it is seen that the frequency derivative of the source correlates with the X-ray flux when the source spins up or down and the 3–20 keV X-ray flux is above $\sim 3 \times 10^{-10}$ erg s^{-1}cm^{-2}, while the frequency derivative does not vary significantly when source spins down and the 3–20 keV X-ray flux is below

$\sim 3 \times 10^{-10}$ erg s^{-1}cm^{-2}. Fig. 7.8 resembles fig. 1 of [104], which presents the frequency derivative as a function of the normalized mass accretion rate (which should be positively correlated with the X-ray flux) of a neutron star accreting from a stellar wind. In fig. 1 of [104], a minimum spin-down rate value is reached when the mass accretion rate is equal to a critical mass accretion rate ($\dot{M}_{cr}$) above which the spin rate is correlated with the mass accretion rate. Mass accretion rates below or above this value lead to smaller spin-down rates, and above a certain normalized mass accretion rate value (y_0), the source enters a spin-up regime. This similarity might indicate that the primary source of the accreted matter is the stellar quasi-spherical stellar wind of the companion. However, the transient QPO feature of the source suggests a transient formation of an accretion disc as the neutron star accretes via the companion's stellar wind [228]. Another low-luminosity long-orbital-period persistent accretion-powered pulsar in a Be X-ray binary system, 1RXS J225352.8+624354, has recently been found to show signs of a possible transient accretion disc formation [243].

Figure 7.8: Left: unabsorbed 3-20 keV RXTE-PCA flux and frequency derivative as a function of time. Right: frequency derivative as a function of unabsorbed 3-20 keV RXTE-PCA flux.

The power spectra of pulse frequency derivatives have been studied for several accretion-powered X-ray pulsars. The random walk in pulse frequency or white noise in the pulse frequency derivative are suitable models for wind-accreting systems such as

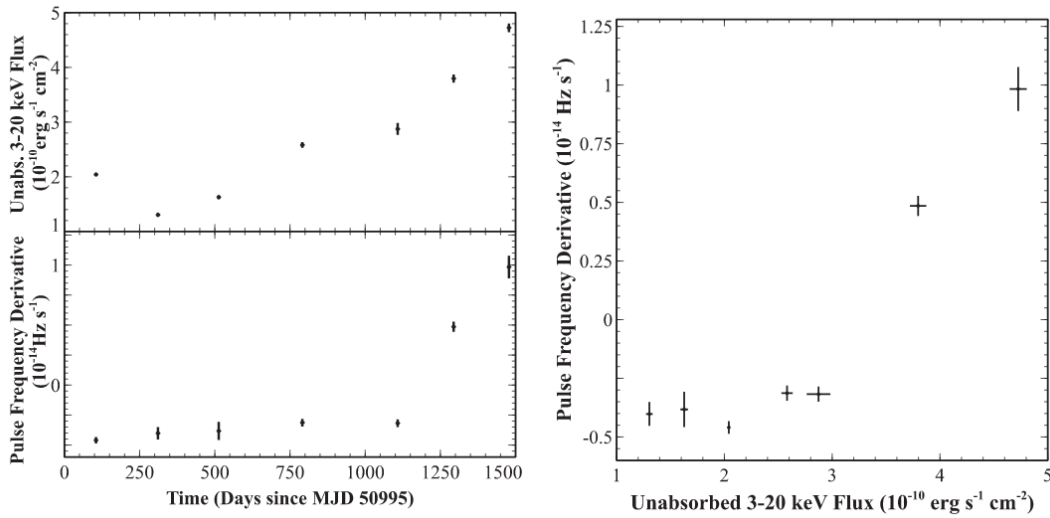Vela X-1, 4U 1538-52 and GX 301-2 ([244]; [245]; [132]). They have flat power spectra with white noise strengths in the range $10^{-20}-10^{-18}$ Hz s^{-2}. For 4U 1907+09, the random walk in pulse frequency is the appropriate model for frequencies between 1/1300 and 1/75 d^{-1} with noise strength 1.27×10^{-21} Hz s^{-2} [226]. For 4U 1907+09, Şahiner et al. [226] have suggested that at shorter time-scales there might be a transient accretion disc formation around the neutron star, which causes random walk in pulse frequency, while the source has a long- term steady spin-down trend. Her X-1 and 4U 1626-67 are disc accretors with low-mass companions. For these sources, it is found that pulse frequency time series are consistent with a random walk model with white noise strengths in the range $10^{-21} - 10^{-18}$ Hz s^{-2}. However, red noise in the pulse frequency derivative cannot be excluded because of the sampling pulse frequencies and the narrow range of power spectra. The disc accretor Cen X-3 has red noise in its pulse frequency derivatives and the noise strength varies from low to high frequencies in the range $10^{-16}-10^{-18}$ Hz s^{-2} [132]. The power-law index of the power spectra of X Per is ~ -1. This implies that at short time-scales, disc accretion dominates and noise is less; however, at longer time-scales greater than the viscous time-scales, there is excessive noise. The steepest power-law index for the power spectra of pulse frequency derivatives among high-mass X-ray binaries (HMXBs) has been seen in SAX J 2103.5+4545 with a power-law index of 2.13 [229]. For GX 1+4 and OAO 1657-415, the power-law indices ~ -1 and ~ 0, respectively, have been found. For these sources, accretion discs can be formed at short time-scales ([194]; [132]). X Per has the lowest noise strength (or torque noise) among the HMXBs discussed above ([223]; [132]). However, the steep power-law index or red noise in the pulse frequency derivative suggests that it could have a transient accretion disc.

The pulse fractions show a clear correlation with the source count rate. As the flux increases, the material appears to accrete more efficiently on the neutron star's magnetic poles. At higher mass accretion rates, the accreting plasma should be interacting with the magnetosphere closer to the neutron star. The shorter distance and the stronger field there could contribute to a higher fraction flowing to the poles.

CHAPTER 8

SUMMARY

In this thesis, the accreting X-ray binaries SWIFT J0513.4–6547, SXP 1062, GX 1+4, and X Per are studied in terms of their timing behaviour. For each source, pulse timing analysis is conducted to resolve its rotational motion. From the fluctuations of the spin frequency residuals, noise strength analysis is carried out to understand the dominant noise processes on different time scales. Furthermore, the torque-luminosity relations are also investigated to deduce the acting mass transfer mechanism within the system.

- The X-ray properties of SWIFT J0513.4–6547 are examined with SWIFT and RXTE observations of both the outburst that occurred in 2009 and the X-ray rebrightening in 2014. In 2009, the outburst prompt to a luminosity $L_x \sim 1.3 \times 10^{38}$ erg/s [126] at the peak which decayed around an order of magnitude and arrived at $\sim 10^{37}$ erg s^{-1} during final stages. At this stage, SWIFT J0513.4–6547 is tracked with 1.74×10^{-11} Hz s^{-1} spin-up rate. This value corresponds to almost half of the initial spin-up rate measurement at the initial stages [126]. Combining the results of this study and [126] fairly bolster the idea that spin-up rate and X-ray luminosity is reasonably correlated. The source faded to quiescence and remained undetected for approximately ~ 2000 days until the rebrightening with $L_x \sim 10^{36}$ erg s^{-1} taking place in 2014.

Interestingly, after the quiescent episode, the timing analysis uncovers that SWIFT J0513.4–6547 is spinning-down (with $\dot{\nu} = -(5.92 \pm 1.9) \times 10^{-14}$ Hz/s). By comparing the difference between the last spin frequency measurement of 2009 outburst and the initial spin frequency measurement of 2014 rebrightening, the average frequency derivative can be attained by $< \dot{\nu} > \sim \Delta\nu/\Delta t$. With this approach, SWIFT J0513.4–6547 actually exhibits an average spin-down rate of $\sim 1.52 \times 10^{-12}$ Hz s^{-1}

during quiescent episode which exceeds the spin-down rate of 2014 rebrightening with a factor of almost 25. Even though it is observed in few systems (e.g. [133]), the spin-down rate of this magnitude at long term quiescent episodes is uncommon for transient systems. The comparison of these two spin-down value measurements (the quiescent and 2014 re-brightening episodes) implies a further endorsement for frequency derivative and luminosity correlation. Because, it implies that whether the source spins up or spins down, its spin rate increases with the X-ray flux.

The magnetic field of SWIFT J0513.4–6547 is estimated under the assumption that observed spin-down rate is achieved at a propeller state during the quiescent episode. Thus, this study reports $\sim 1.5 \times 10^{13}$ G of B-field strength. This value is consistent with the B-field strength deduced from correlative torque-luminosity association at accretion phase by [126]. Furthermore, the results confirm and refine the previously reported orbit parameters by [121] and [126].

• Properties of an other BeXB source X Per is probed with ~ 4.5 years of data acquired by RXTE between 1998 July 1 and 2003 February 17. Following the pulse timing methodology, the timing solution covering all the RXTE data is obtained. Using the pulse TOAs, corresponding spin frequency history is generated. The frequency series are further extended using INTEGRAL observations. The results indicate that rotational motion of X Per underwent a torque reversal around ~ 52250 MJD. With these measurements, the long term frequency history is enriched significantly (see Figure 7.5).

Entire series of frequency measurements of X Per is held subject to noise strength analysis. The power density spectra are constructed from the residuals after both quadratic ($m = 2$) and cubic trends ($m = 3$). Both of the power spectra yield comparable results: the noise level varies between $10^{-20} - 10^{-23}$ Hz s^{-2} for analysis frequencies range in 1/35 to 1 yr^{-1} for both cases. The power spectra carry a red noise component with average steepness (power-law index) ~ -1, which get whiter at short time-scales. The noise level of X Per is the lowest among the sources in this study. Nevertheless, the shape of the power spectrum suggests the formation of a transient disk, since the noise process dominates the accretion on the time-scales greater than the viscous time-scales.

For the source X Per, the relation between spin frequency derivative and X-ray luminosity is also examined. It is shown that a positive correlation is present when the source flux is above $\sim 3 \times 10^{-10}$ erg s^{-1}cm^{-2}. Furthermore, there is no correlation among the two variables when the flux is below $\sim 3 \times 10^{-10}$ erg s^{-1}cm^{-2}. From theoretical perspective, for the sources that accrete from a quasi-spherical shell, it is expected that a correlation should exist above a critical value of flux [104] which is in a good agreement with the case of X Per. Therefore, it is argued that X Per is accreting from a quasi-spherical shell.

• The timing studies of GX 1+4 is conducted by examining the 2 years data set of RXTE observations between 2001 March 3 and 2003 January 31. Due to the gap within the data, timing solutions are acquired for two different time intervals (~ 250 and ~ 300 days long). Using these solutions, ~ 2 years of the frequency series is generated. With these measurements, the study contributes to the long term frequency history which had started from early 1970s (see [131] and also Figure 6.3). The complete set of frequency series of GX 1+4 is investigated in terms of the torque noise fluctuations. With this motivation, the power spectrum of the pulse frequency derivative fluctuations is established. This spectrum has the longest time coverage (from 31 days to 44 years) among all the spectra in the literature. At the smallest time-scales, the power estimate starts with a noise strength level of $S = 1.0 \times 10^{-18}$ Hz s^{-2} which alters steeply with f^{-1} noise process and reaches to $S = 6.5 \times 10^{-16}$ Hz s^{-2} level at the longest time-scale. The flicker type (f^{-1}) noise process of GX 1+4 is also consistent with previously reported noise analysis by [132]. Even though, since 1970s various X-ray studies had kept track of the spin frequency measurements of GX 1+4 [131], the orbital motion of the system remains still an enigma. In spite of not being observed in X-rays, an orbit with $P_{orb} \sim 1162$ days and $a/c \sin i \sim 773$ is inferred from radial velocity measurements in infrared observations [212]. The noise strength analysis of this study may shed a light on this enigma. Because the timing noise level on the suggested orbital motion time-scales produces higher frequency fluctuations than the proposed orbital modulation amplitude. Thus, the noise level dominates the frequency fluctuations which prevents the orbital parameters to be detected from modulations in X-ray spin frequency measurements.

On the other hand, this study further examines ~ 9 years of BATSE data between

1991 and 2000. Episodic alterations of torque-luminosity correlation is explored. The study reveals a recurrent mode-switching between correlation and anti-correlation episodes. Interestingly, the periodicity of the maximal correlation episodes is consistent with the orbital period deduced from infrared observations [212].

• The SXP 1062 is studied through two years of observation journey with various X-ray missions between 2012 and 2014 . The source underwent recurrent bursts of *Type I* with flux enhancements in both optical and X-ray bands. In X-rays, the flux enhancement led to $L_x \simeq 1.3 \times 10^{37}$ erg/s peak value, which declined towards $L_x \sim 10^{36}$ erg/s at the end of observation sequence. The observation journey ends before reaching the priori quiescent level back again ($\approx 2.4 \times 10^{35}$ erg/s at minimum) . The recurrence period of bursting sequence is about 656 days which is an indicator of the orbital period [144]. The results of this study further derive the orbital parameters by measuring the modulations of the pulse TOAs (see Table 5.1). Moreover, the resultant mass of the companion compiles with the one inferred from optical studies by [140]. However, orbital parameters are deduced only by using the pulse TOAs prior to the glitch which covers a bit less than one complete cycle. Hence a further monitoring of SXP 1062 is required to make a better assessment about orbital motion.

The SXP 1062 rotates very slowly ($P_{spin} \sim 1062$ s) but still spins-down regularly. These properties have led to the thought that the pulsar in the SXP 1062 system possesses a colossal field strength which may even be "magnetar-like" field. Several attempts have been made to understand the strength of its magnetic field using various theories, all of which have returned values more than 10^{14} G [148]. In this study, a magnetic field estimation is offered via standard disk theories (e.g. [68]; [70]). Using the frequency derivative value measured prior to the glitch, the B-field is estimated to be $\sim 1.5 \times 10^{14}$ G, which is totally consistent with the values suggested by [148].

The results of the pulse timing studies of SXP 1062 uncovered an important feature taking place in accreting pulsars. This study revealed the occurrence of a sudden frequency jump in the pulsed emission of SXP 1062. The frequency jump, called glitch event, happened 25 days after the outburst. In other words, the outburst did not yield a significant change in any timing parameter and the source steadily resumed its rotational motion for another 25 days which implies that the observed event is not

112

originated from accretion torques. Thus, the frequency jump should be connected with the physical changes within the interior structure of the neutron star. These events are usually observed in isolated pulsars, but so far they were not observed in any accreting system. In accreting pulsars, the accretion maintains an external torque which dominantly governs the rotational motion of the pulsar. Therefore, the glitch events are extremely difficult to resolve in the presence of accretion. After decades of observing hundreds of accreting pulsars, this study is the only one that is able to distinguish a glitch event from accretion torques. From theoretical point of view, the observability of such events were already brought to attention by [196]. The magnitude of the resolved glitch event is $\Delta\nu = 1.28(5) \times 10^{-6}$ Hz. Using the theoretical model of [196], the accreting pulsar in SXP 1062 system has either high coupled-vortex fraction (around 78%) or a low pining force (6.4×10^{13} dyn/cm) when compared to ordinary isolated pulsars. In order for the latter case to be possible, the accretion must yield a "softer" crust. Furthermore, the fractional amplitude of the jump ($\sim 10^{-3}$) is the largest fractional jump discovered up to now. While glitch events are common for isolated pulsars, the glitch of SXP 1062 is the first confirmation of the observability of this type of events among accretion-powered pulsars.

REFERENCES

[1] J. Chadwick, "The existence of a neutron," *Proceedings of the Royal Society*, vol. 136, June 1932.

[2] W. Baade and F. Zwicky, "Cosmic Rays from Super-novae," *Contributions from the Mount Wilson Observatory, vol. 3, pp.79-83*, vol. 3, pp. 79–83, 1934.

[3] A. Hewish, S. J. Bell, J. D. H. Pilkington, P. F. Scott, and R. A. Collins, "Observation of a Rapidly Pulsating Radio Source," *Nature*, vol. 217, pp. 709–713, Feb. 1968.

[4] J. M. Lattimer and M. Prakash, "The Physics of Neutron Stars," *Science*, vol. 304, pp. 536–542, Apr. 2004.

[5] V. E. Zavlin, "Theory of Radiative Transfer in Neutron Star Atmospheres and Its Applications," in *Astrophysics and Space Science Library* (W. Becker, ed.), vol. 357 of *Astrophysics and Space Science Library*, p. 181, 2009.

[6] V. M. Kaspi, "Grand unification of neutron stars," *Proceedings of the National Academy of Science*, vol. 107, pp. 7147–7152, Apr. 2010.

[7] E. V. Gotthelf, J. P. Halpern, and J. Alford, "The Spin-down of PSR J0821-4300 and PSR J1210-5226: Confirmation of Central Compact Objects as Anti-magnetars," *ApJ*, vol. 765, p. 58, Mar. 2013.

[8] A. De Luca, "Central compact objects in supernova remnants," in *Journal of Physics Conference Series*, vol. 932 of *Journal of Physics Conference Series*, p. 012006, Dec. 2017.

[9] V. M. Kaspi and A. M. Beloborodov, "Magnetars," *Annu. Rev. Astron. Astrophys.*, vol. 55, pp. 261–301, Aug. 2017.

[10] R. Turolla, S. Zane, and A. L. Watts, "Magnetars: the physics behind observations. A review," *Reports on Progress in Physics*, vol. 78, p. 116901, Nov. 2015.

[11] K. Hurley, T. Cline, E. Mazets, S. Barthelmy, P. Butterworth, F. Marshall, D. Palmer, R. Aptekar, S. Golenetskii, V. Il'Inskii, D. Frederiks, J. McTiernan, R. Gold, and J. Trombka, "A giant periodic flare from the soft γ-ray repeater SGR1900+14," *Nature*, vol. 397, pp. 41–43, Jan. 1999.

[12] E. P. Mazets, S. V. Golenetskij, and Y. A. Guryan, "Soft gamma-ray bursts from the source B1900+14," *Soviet Astronomy Letters*, vol. 5, pp. 641–643, Dec. 1979.

[13] M. A. McLaughlin, A. G. Lyne, D. R. Lorimer, M. Kramer, A. J. Faulkner, R. N. Manchester, J. M. Cordes, F. Camilo, A. Possenti, I. H. Stairs, G. Hobbs, N. D'Amico, M. Burgay, and J. T. O'Brien, "Transient radio bursts from rotating neutron stars," *Nature*, vol. 439, pp. 817–820, Feb. 2006.

[14] H. S. Knight, M. Bailes, R. N. Manchester, S. M. Ord, and B. A. Jacoby, "Green Bank Telescope Studies of Giant Pulses from Millisecond Pulsars," *ApJ*, vol. 640, pp. 941–949, Apr. 2006.

[15] J. M. Cordes and R. M. Shannon, "Rocking the Lighthouse: Circumpulsar Asteroids and Radio Intermittency," *ApJ*, vol. 682, pp. 1152–1165, Aug. 2008.

[16] S. L. Redman and J. M. Rankin, "On the randomness of pulsar nulls," *MNRAS*, vol. 395, pp. 1529–1532, May 2009.

[17] B. Posselt, S. B. Popov, F. Haberl, J. Trümper, R. Turolla, and R. Neuhauser, "The Magnificent Seven in the dusty prairie," *Astrophysics and Space Science*, vol. 308, pp. 171–179, Apr. 2007.

[18] M. H. van Kerkwijk and D. L. Kaplan, "Isolated neutron stars: magnetic fields, distances,and spectra," *Astrophysics and Space Science*, vol. 308, pp. 191–201, Apr. 2007.

[19] D. L. Kaplan and M. H. van Kerkwijk, "A Coherent Timing Solution for the Nearby, Thermally Emitting Isolated Neutron Star RX J0420.0-5022," *ApJL*, vol. 740, p. L30, Oct. 2011.

[20] F. Haberl, "The magnificent seven: magnetic fields and surface temperature distributions," *Astrophysics and Space Science*, vol. 308, pp. 181–190, Apr. 2007.

[21] D. L. Kaplan, "Nearby, Thermally Emitting Neutron Stars," in *Astrophysics of Compact Objects* (Y.-F. Yuan, X.-D. Li, and D. Lai, eds.), vol. 968 of *American Institute of Physics Conference Series*, pp. 129–136, Jan. 2008.

[22] R. Turolla, "Isolated Neutron Stars: The Challenge of Simplicity," in *Astrophysics and Space Science Library* (W. Becker, ed.), vol. 357 of *Astrophysics and Space Science Library*, p. 141, 2009.

[23] E. E. Salpeter, "Models for Compact X-Ray Sources," in *X- and Gamma-Ray Astronomy* (H. Bradt and R. Giacconi, eds.), vol. 55 of *IAU Symposium*, p. 135, 1973.

[24] Q. Z. Liu, J. van Paradijs, and E. P. J. van den Heuvel, "VizieR Online Data Catalog: Catalogue of Galactic low-mass X-ray binaries (Liu+, 2007)," *VizieR Online Data Catalog*, vol. 346, June 2007.

[25] M. A. Alpar, A. F. Cheng, M. A. Ruderman, and J. Shaham, "A new class of radio pulsars," *Nature*, vol. 300, pp. 728–730, Dec. 1982.

[26] T. M. Tauris and E. P. J. van den Heuvel, *Formation and evolution of compact stellar X-ray sources*, pp. 623–665. Apr. 2006.

[27] D. Bhattacharya and E. P. J. van den Heuvel, "Formation and evolution of binary and millisecond radio pulsars," *Physics Reports*, vol. 203, pp. 1–124, 1991.

[28] A. Ibragimov and J. Poutanen, "Accreting millisecond pulsar SAX J1808.4-3658 during its 2002 outburst: evidence for a receding disc," *MNRAS*, vol. 400, pp. 492–508, Nov. 2009.

[29] D. Psaltis and F. K. Lamb, "Magnetic fields of neutron stars in low mass X-ray binaries," *Astronomical and Astrophysical Transactions*, vol. 18, pp. 447–454, 1999.

[30] N. I. Shakura, "Disk Model of Gas Accretion on a Relativistic Star in a Close Binary System.," *Soviet Astronomy*, vol. 16, p. 756, Apr. 1973.

[31] S. Bhattacharyya, "Measurement of neutron star parameters: A review of

methods for low-mass X-ray binaries," *Advances in Space Research*, vol. 45, pp. 949–978, Apr. 2010.

[32] D. K. Galloway, M. P. Muno, J. M. Hartman, D. Psaltis, and D. Chakrabarty, "Thermonuclear (Type I) X-Ray Bursts Observed by the Rossi X-Ray Timing Explorer," *ApJS*, vol. 179, pp. 360–422, Dec. 2008.

[33] T. Strohmayer and L. Bildsten, *New views of thermonuclear bursts*, pp. 113–156. Apr. 2006.

[34] P. C. Joss, "X-ray bursts and neutron-star thermonuclear flashes," *Nature*, vol. 270, pp. 310–314, Nov. 1977.

[35] D. Q. Lamb and F. K. Lamb, "Nuclear burning in accreting neutron stars and X-ray bursts," *ApJ*, vol. 220, pp. 291–302, Feb. 1978.

[36] J. H. Swank, R. H. Becker, E. A. Boldt, S. S. Holt, S. H. Pravdo, and P. J. Serlemitsos, "Spectral evolution of a long X-ray burst," *ApJL*, vol. 212, pp. L73–L76, Mar. 1977.

[37] J. A. Hoffman, W. H. G. Lewin, and J. Doty, "Observations of the X-ray burst source MXB 1636-53," *ApJL*, vol. 217, pp. L23–L28, Oct. 1977.

[38] T. E. Strohmayer, W. Zhang, J. H. Swank, A. Smale, L. Titarchuk, C. Day, and U. Lee, "Millisecond X-Ray Variability from an Accreting Neutron Star System," *ApJL*, vol. 469, p. L9, Sept. 1996.

[39] T. E. Strohmayer, W. Zhang, J. H. Swank, and I. Lapidus, "The Long-Term Stability of Oscillations during Thermonuclear X-Ray Bursts: Constraining the Binary X-Ray Mass Function," *ApJL*, vol. 503, pp. L147–L150, Aug. 1998.

[40] Q. Z. Liu, J. van Paradijs, and E. P. J. van den Heuvel, "Catalogue of high-mass X-ray binaries in the Galaxy (4th edition)," *Astronomy and Astrophysics*, vol. 455, pp. 1165–1168, Sept. 2006.

[41] R. H. D. Corbet, "The three types of high-mass X-ray pulsator," *MNRAS*, vol. 220, pp. 1047–1056, June 1986.

[42] P. Reig, "Be/X-ray binaries," *ApSS*, vol. 332, pp. 1–29, Mar. 2011.

[43] S. Chaty, "High Mass X-ray Binaries: Progenitors of double neutron star systems," *arXiv e-prints*, Oct. 2015.

[44] R. Walter, A. A. Lutovinov, E. Bozzo, and S. S. Tsygankov, "High-mass X-ray binaries in the Milky Way. A closer look with INTEGRAL," *The Astronomy and Astrophysics Review*, vol. 23, p. 2, Aug. 2015.

[45] I. Negueruela, D. M. Smith, P. Reig, S. Chaty, and J. M. Torrejón, "Supergiant Fast X-ray Transients: A New Class of High Mass X-ray Binaries Unveiled by INTEGRAL," in *The X-ray Universe 2005* (A. Wilson, ed.), vol. 604 of *ESA Special Publication*, p. 165, Jan. 2006.

[46] M. C. Runacres and S. P. Owocki, "A pseudo-planar, periodic-box formalism for modelling the outer evolution of structure in spherically expanding stellar winds," *Astronomy and Astrophysics*, vol. 429, pp. 323–333, Jan. 2005.

[47] L. Sidoli, P. Romano, S. Mereghetti, A. Paizis, S. Vercellone, V. Mangano, and D. Götz, "An alternative hypothesis for the outburst mechanism in supergiant fast X-ray transients: the case of IGR J11215-5952," *Astronomy and Astrophysics*, vol. 476, pp. 1307–1315, Dec. 2007.

[48] L. Sidoli, "Transient outburst mechanisms in Supergiant Fast X-ray Transients," *Advances in Space Research*, vol. 43, pp. 1464–1470, May 2009.

[49] E. Bozzo, M. Falanga, and L. Stella, "Are There Magnetars in High-Mass X-Ray Binaries? The Case of Supergiant Fast X-Ray Transients," *ApJ*, vol. 683, pp. 1031–1044, Aug. 2008.

[50] M. J. Coe and J. A. Orosz, "OGLE observations of four X-ray binary pulsars in the Small Magellanic Cloud," *MNRAS*, vol. 311, pp. 169–175, Jan. 2000.

[51] I. Negueruela, "On the nature of Be/X-ray binaries," *Astronomy and Astrophysics*, vol. 338, pp. 505–510, Oct. 1998.

[52] J. M. Porter and T. Rivinius, "Classical Be Stars," *The Publications of the Astronomical Society of the Pacific*, vol. 115, pp. 1153–1170, Oct. 2003.

[53] R. H. D. Townsend, S. P. Owocki, and I. D. Howarth, "Be-star rotation: how close to critical?," *MNRAS*, vol. 350, pp. 189–195, May 2004.

[54] I. Negueruela, P. Reig, M. J. Coe, and J. Fabregat, "Large-scale perturbations in the circumstellar envelopes of Be/X-ray binaries," *Astronomy and Astrophysics*, vol. 336, pp. 251–262, Aug. 1998.

[55] E. P. J. van den Heuvel and S. Rappaport, "X-ray observations of B-emission stars," in *IAU Colloq. 92: Physics of Be Stars* (A. Slettebak and T. P. Snow, eds.), pp. 291–307, 1987.

[56] A. T. Okazaki and I. Negueruela, "A natural explanation for periodic X-ray outbursts in Be/X-ray binaries," *Astronomy and Astrophysics*, vol. 377, pp. 161–174, Oct. 2001.

[57] I. Negueruela, A. T. Okazaki, J. Fabregat, M. J. Coe, U. Munari, and T. Tomov, "The Be/X-ray transient 4U 0115+63/V635 Cassiopeiae. II. Outburst mechanisms," *Astronomy and Astrophysics*, vol. 369, pp. 117–131, Apr. 2001.

[58] L. Stella, N. E. White, and R. Rosner, "Intermittent stellar wind accretion and the long-term activity of Population I binary systems containing an X-ray pulsar," *ApJ*, vol. 308, pp. 669–679, Sept. 1986.

[59] S. Campana, L. Stella, G. L. Israel, A. Moretti, A. N. Parmar, and M. Orlandini, "The Quiescent X-Ray Emission of Three Transient X-Ray Pulsars," *ApJ*, vol. 580, pp. 389–393, Nov. 2002.

[60] J. Ziolkowski, "Be/X-ray binaries.," *Memorie della Societa Astronomica Italiana*, vol. 73, pp. 1038–1038, 2002.

[61] C. A. Wilson, M. H. Finger, and A. Camero-Arranz, "Outbursts Large and Small from EXO 2030+375," *ApJ*, vol. 678, pp. 1263–1272, May 2008.

[62] K. Brecher, R. A. Fesen, S. P. Maran, and J. C. Brandt, "Ancient records and the Crab Nebula supernova," *The Observatory*, vol. 103, pp. 106–113, June 1983.

[63] A. G. Lyne, C. A. Jordan, F. Graham-Smith, C. M. Espinoza, B. W. Stappers, and P. Weltevrede, "45 years of rotation of the Crab pulsar," *MNRAS*, vol. 446, pp. 857–864, Jan. 2015.

[64] C.-A. Faucher-Giguère and V. M. Kaspi, "Birth and Evolution of Isolated Radio Pulsars," *ApJ*, vol. 643, pp. 332–355, May 2006.

[65] P. R. Brook, A. Karastergiou, S. Johnston, M. Kerr, R. M. Shannon, and S. J. Roberts, "Emission-rotation correlation in pulsars: new discoveries with optimal techniques," *MNRAS*, vol. 456, pp. 1374–1393, Feb. 2016.

[66] E. E. Salpeter, "Accretion of Interstellar Matter by Massive Objects.," *ApJ*, vol. 140, pp. 796–800, Aug. 1964.

[67] Y. B. Zel'dovich, "The Fate of a Star and the Evolution of Gravitational Energy Upon Accretion," *Soviet Physics Doklady*, vol. 9, p. 195, Sept. 1964.

[68] J. E. Pringle and M. J. Rees, "Accretion Disc Models for Compact X-Ray Sources," *Astronomy and Astrophysics*, vol. 21, p. 1, Oct. 1972.

[69] F. K. Lamb, C. J. Pethick, and D. Pines, "A Model for Compact X-Ray Sources: Accretion by Rotating Magnetic Stars," *ApJ*, vol. 184, pp. 271–290, Aug. 1973.

[70] P. Ghosh and F. K. Lamb, "Accretion by rotating magnetic neutron stars. III - Accretion torques and period changes in pulsating X-ray sources," *ApJ*, vol. 234, pp. 296–316, Nov. 1979.

[71] A. F. Illarionov and R. A. Sunyaev, "Why the Number of Galactic X-ray Stars Is so Small?," *Astronomy and Astrophysics*, vol. 39, p. 185, Feb. 1975.

[72] D. H. Sharp, "An overview of Rayleigh-Taylor instability," *Physica D: Nonlinear Phenomena*, vol. 12, pp. 3–10, 1984.

[73] P. Ghosh and F. K. Lamb, "Disk accretion by magnetic neutron stars," *ApJL*, vol. 223, pp. L83–L87, July 1978.

[74] P. Ghosh and F. K. Lamb, "Accretion by rotating magnetic neutron stars. II - Radial and vertical structure of the transition zone in disk accretion," *ApJ*, vol. 232, pp. 259–276, Aug. 1979.

[75] J. Arons and S. M. Lea, "Accretion onto magnetized neutron stars - Structure and interchange instability of a model magnetosphere," *ApJ*, vol. 207, pp. 914–936, Aug. 1976.

[76] R. F. Elsner and F. K. Lamb, "Accretion by magnetic neutron stars. I - Magne-tospheric structure and stability," *ApJ*, vol. 215, pp. 897–913, Aug. 1977.

[77] J. M. Stone and T. Gardiner, "The Magnetic Rayleigh-Taylor Instability in Three Dimensions," *ApJ*, vol. 671, pp. 1726–1735, Dec. 2007.

[78] A. K. Kulkarni and M. M. Romanova, "Accretion to magnetized stars through the Rayleigh-Taylor instability: global 3D simulations," *MNRAS*, vol. 386, pp. 673–687, May 2008.

[79] R. V. E. Lovelace, "Electrodynamic/Hydrodynamic Models for Jets in Galactic Nuclei," in *Bulletin of the American Astronomical Society*, vol. 13 of *Bulletin of the American Astronomical Society*, p. 824, Mar. 1981.

[80] L.-X. Li and R. Narayan, "Quasi-periodic Oscillations from Rayleigh-Taylor and Kelvin-Helmholtz Instability at a Disk-Magnetosphere Interface," *ApJ*, vol. 601, pp. 414–427, Jan. 2004.

[81] N. I. Shakura and R. A. Sunyaev, "A theory of the instability of disk accretion on to black holes and the variability of binary X-ray sources, galactic nuclei and quasars," *MNRAS*, vol. 175, pp. 613–632, June 1976.

[82] I. Negueruela, "Stellar Wind Accretion in High-Mass X-Ray Binaries," in *High Energy Phenomena in Massive Stars* (J. Martí, P. L. Luque-Escamilla, and J. A. Combi, eds.), vol. 422 of *Astronomical Society of the Pacific Conference Series*, p. 57, May 2010.

[83] J. E. Pringle, "Accretion discs in astrophysics," *In: Annual review of astronomy and astrophysics*, vol. 19, pp. 137–162, 1981.

[84] J. Frank, A. King, and D. J. Raine, *Accretion Power in Astrophysics: Third Edition*. Jan. 2002.

[85] P. Jetzer, M. Strässle, and N. Straumann, "On the variation of pulsar periods in close binary systems," *New Astronomy*, vol. 3, pp. 619–630, Dec. 1998.

[86] R. Perna, E. Bozzo, and L. Stella, "On the Spin-up/Spin-down Transitions in Accreting X-Ray Binaries," *ApJ*, vol. 639, pp. 363–376, Mar. 2006.

[87] F. Shu, J. Najita, E. Ostriker, F. Wilkin, S. Ruden, and S. Lizano, "Magnetocentrifugally driven flows from young stars and disks. 1: A generalized model," *ApJ*, vol. 429, pp. 781–796, July 1994.

[88] F. H. Shu, G. Laughlin, S. Lizano, and D. Galli, "Singular Isothermal Disks. I. Linear Stability Analysis," *ApJ*, vol. 535, pp. 190–210, May 2000.

[89] R. V. E. Lovelace, M. M. Romanova, and G. S. Bisnovatyi-Kogan, "Spin-up/spin-down of magnetized stars with accretion discs and outflows," *MNRAS*, vol. 275, pp. 244–254, July 1995.

[90] R. V. E. Lovelace, M. M. Romanova, and G. S. Bisnovatyi-Kogan, "Magnetic Propeller Outflows," *ApJ*, vol. 514, pp. 368–372, Mar. 1999.

[91] D. A. Uzdensky, "Magnetic Interaction Between Stars And Accretion Disks," *Astrophysics and Space Science*, vol. 292, pp. 573–585, Aug. 2004.

[92] S. Matt and R. E. Pudritz, "Accretion-powered Stellar Winds as a Solution to the Stellar Angular Momentum Problem," *ApJL*, vol. 632, pp. L135–L138, Oct. 2005.

[93] D. Lai, "Theory of Disk Accretion onto Magnetic Stars," in *European Physical Journal Web of Conferences*, vol. 64 of *European Physical Journal Web of Conferences*, p. 01001, Jan. 2014.

[94] J. Frank, A. King, and D. Raine, "Books-Received - Accretion Power in Astrophysics - ED.2," *Journal of the British Astronomical Association*, vol. 102, p. 287, Oct. 1992.

[95] M. Sugizaki, T. Mihara, M. Nakajima, and K. Makishima, "Correlation between the luminosity and spin-period changes during outbursts of 12 Be binary pulsars observed by the MAXI/GSC and the Fermi/GBM," *Publications of the Astronomical Society of Japan*, vol. 69, p. 100, Dec. 2017.

[96] K. Davidson and J. P. Ostriker, "Neutron-Star Accretion in a Stellar Wind: Model for a Pulsed X-Ray Source," *ApJ*, vol. 179, pp. 585–598, Jan. 1973.

[97] H. Bondi and F. Hoyle, "On the mechanism of accretion by stars," *MNRAS*, vol. 104, p. 273, 1944.

[98] "Book Review: Introduction to stellar winds / Cambridge U Press, 1999," *Irish Astronomical Journal*, vol. 26, p. 171, 1999.

[99] J. S. Vink, A. de Koter, and H. J. G. L. M. Lamers, "New theoretical mass-loss rates of O and B stars," *Astronomy and Astrophysics*, vol. 362, pp. 295–309, Oct. 2000.

[100] R. Edgar, "A review of Bondi-Hoyle-Lyttleton accretion," *New Astronomy Reviews*, vol. 48, pp. 843–859, Sept. 2004.

[101] R. E. Davies and J. E. Pringle, "Spindown of neutron stars in close binary systems. II," *MNRAS*, vol. 196, pp. 209–224, July 1981.

[102] D. J. Burnard, J. Arons, and S. M. Lea, "Accretion onto magnetized neutron stars - X-ray pulsars with intermediate rotation rates," *ApJ*, vol. 266, pp. 175–187, Mar. 1983.

[103] N. Shakura and K. Postnov, "Wind Accretion - Observations Vs Theory," *arXiv e-prints*, Feb. 2017.

[104] N. Shakura, K. Postnov, A. Kochetkova, and L. Hjalmarsdotter, "Theory of quasi-spherical accretion in X-ray pulsars," *MNRAS*, vol. 420, pp. 216–236, Feb. 2012.

[105] F. Fürst, I. Kreykenbohm, K. Pottschmidt, J. Wilms, M. Hanke, R. E. Rothschild, P. Kretschmar, N. S. Schulz, D. P. Huenemoerder, D. Klochkov, and R. Staubert, "X-ray variation statistics and wind clumping in Vela X-1," *Astronomy and Astrophysics*, vol. 519, p. A37, Sept. 2010.

[106] D. A. Leahy, W. Darbro, R. F. Elsner, M. C. Weisskopf, P. G. Sutherland, S. Kahn, and J. E. Grindlay, "On searches for pulsed emission with application to four globular cluster X-ray sources - NGC 1851, 6441, 6624, and 6712," *ApJ*, vol. 266, pp. 160–170, Mar. 1983.

[107] R. N. Manchester and J. H. Taylor, *Pulsars*. 1977.

[108] J. E. Deeter, P. E. Boynton, and S. H. Pravdo, "Pulse-timing observations of Hercules X-1," *ApJ*, vol. 247, pp. 1003–1012, Aug. 1981.

[109] J. E. Deeter and P. E. Boynton, "Timing Studies of X-ray Sources," in *Proc. Inuyama Workshop*, Nagoya Univ., p. 29, 1985.

[110] R. Manchester, J. Taylor, W. Peters, J. Weisberg, A. Irwin, N. Wex, I. Stairs, P. Demorest, and D. Nice, "Tempo: Pulsar timing data analysis." Astrophysics Source Code Library, Sept. 2015.

[111] P. E. Boynton, E. J. Groth, D. P. Hutchinson, G. P. Nanos, Jr., R. B. Partridge, and D. T. Wilkinson, "Optical Timing of the Crab Pulsar, NP 0532," *ApJ*, vol. 175, p. 217, July 1972.

[112] F. D'Alessandro, P. M. McCulloch, P. A. Hamilton, and A. A. Deshpande, "The timing noise of 45 southern pulsars," *MNRAS*, vol. 277, pp. 1033–1046, Dec. 1995.

[113] J. M. Cordes and G. S. Downs, "JPL pulsar timing observations. III - Pulsar rotation fluctuations," *ApJS*, vol. 59, pp. 343–382, Nov. 1985.

[114] J. M. Cordes, "Pulsar timing. II - Analysis of random walk timing noise - Application to the Crab pulsar," *ApJ*, vol. 237, pp. 216–226, Apr. 1980.

[115] Z. Arzoumanian, D. J. Nice, J. H. Taylor, and S. E. Thorsett, "Timing behavior of 96 radio pulsars," *ApJ*, vol. 422, pp. 671–680, Feb. 1994.

[116] D. N. Matsakis, J. H. Taylor, and T. M. Eubanks, "A statistic for describing pulsar and clock stabilities.," *Astronomy and Astrophysics*, vol. 326, pp. 924–928, Oct. 1997.

[117] J. E. Deeter, "Techniques for the estimation of red power spectra. II Evaluation of alternative methods," *ApJ*, vol. 281, pp. 482–491, June 1984.

[118] D. M. Scott, M. H. Finger, and C. A. Wilson, "Characterization of the timing noise of the Crab pulsar," *MNRAS*, vol. 344, pp. 412–430, Sept. 2003.

[119] M. A. Alpar, R. Nandkumar, and D. Pines, "Vortex creep and the internal temperature of neutron stars The Crab pulsar and PSR 0525 + 21," *ApJ*, vol. 288, pp. 191–195, Jan. 1985.

[120] K. S. Cheng, "Could glitches inducing magnetospheric fluctuations produce low-frequency pulsar timing noise?," *ApJ*, vol. 321, pp. 805–812, Oct. 1987.

[121] M. H. Finger and E. Beklen, "Detection of pulsation from Swift J0513.4-6547 with Fermi/GBM," *The Astronomer's Telegram*, vol. 2023, Apr. 2009.

[122] Ş. Şahiner, M. M. Serim, A. Baykal, and S. Ç. İnam, "RXTE and Swift Observations of SWIFT J0513.4-6547," *MNRAS*, vol. 456, pp. 845–852, Feb. 2016.

[123] H. A. Krimm, R. H. D. Corbet, P. A. Evans, S. T. Holland, C. B. Markwardt, T. E. Strohmayer, S. D. Barthelmy, W. Baumgartner, J. R. Cummings, E. Fenimore, N. Gehrels, D. Palmer, A. M. Parsons, T. Sakamoto, G. Skinner, M. Stamatikos, and J. Tueller, "Swift and RXTE report the detection of a new transient pulsar Swift J0513.4-6547 in the Large Magellanic Cloud," *The Astronomer's Telegram*, vol. 2011, Apr. 2009.

[124] H. A. Krimm, S. T. Holland, R. H. D. Corbet, A. B. Pearlman, P. Romano, J. A. Kennea, J. S. Bloom, S. D. Barthelmy, W. H. Baumgartner, J. R. Cummings, N. Gehrels, A. Y. Lien, C. B. Markwardt, D. M. Palmer, T. Sakamoto, M. Stamatikos, and T. N. Ukwatta, "The Swift/BAT Hard X-Ray Transient Monitor," *ApJS*, vol. 209, p. 14, Nov. 2013.

[125] M. J. Coe, A. Udalski, and M. Finger, "Discovery of an optical modulation in Swift J0513.4-6547," *The Astronomer's Telegram*, vol. 5511, Oct. 2013.

[126] M. J. Coe, M. Finger, E. S. Bartlett, and A. Udalski, "Swift J0513.4-6547 = LXP 27.2: a new Be/X-ray binary system in the Large Magellanic Cloud," *MNRAS*, vol. 447, pp. 1630–1637, Feb. 2015.

[127] R. H. D. Corbet, "Be/neutron star binaries - A relationship between orbital period and neutron star spin period," *Astronomy and Astrophysics*, vol. 141, pp. 91–93, Dec. 1984.

[128] R. Sturm, S. Carpano, F. Haberl, P. Maggi, and G. Vasilopoulos, "Swift J0513.4-6547 in outburst," *The Astronomer's Telegram*, vol. 6483, Sept. 2014.

[129] K. Jahoda, J. H. Swank, A. B. Giles, M. J. Stark, T. Strohmayer, W. Zhang, and E. H. Morgan, "In-orbit performance and calibration of the Rossi X-ray Timing Explorer (RXTE) Proportional Counter Array (PCA)," in *EUV, X-Ray, and Gamma-Ray Instrumentation for Astronomy VII* (O. H. Siegmund and M. A. Gummin, eds.), vol. 2808 of *Proceedings of SPIE*, pp. 59–70, Oct. 1996.

[130] D. N. Burrows, J. E. Hill, J. A. Nousek, J. A. Kennea, A. Wells, J. P. Osborne, A. F. Abbey, A. Beardmore, K. Mukerjee, A. D. T. Short, G. Chincarini, S. Campana, O. Citterio, A. Moretti, C. Pagani, G. Tagliaferri, P. Giommi, M. Capalbi, F. Tamburelli, L. Angelini, G. Cusumano, H. W. Bräuninger, W. Burkert, and G. D. Hartner, "The Swift X-Ray Telescope," *Space Science Reviews*, vol. 120, pp. 165–195, Oct. 2005.

[131] A. González-Galán, E. Kuulkers, P. Kretschmar, S. Larsson, K. Postnov, A. Kochetkova, and M. H. Finger, "Spin period evolution of GX 1+4," *Astronomy and Astrophysics*, vol. 537, p. A66, Jan. 2012.

[132] L. Bildsten, D. Chakrabarty, J. Chiu, M. H. Finger, D. T. Koh, R. W. Nelson, T. A. Prince, B. C. Rubin, D. M. Scott, M. Stollberg, B. A. Vaughan, C. A. Wilson, and R. B. Wilson, "Observations of Accreting Pulsars," *ApJS*, vol. 113, pp. 367–408, Dec. 1997.

[133] H. Klus, W. C. G. Ho, M. J. Coe, R. H. D. Corbet, and L. J. Townsend, "Spin period change and the magnetic fields of neutron stars in Be X-ray binaries in the Small Magellanic Cloud," *MNRAS*, vol. 437, pp. 3863–3882, Feb. 2014.

[134] M. A. Alpar, "On Young Neutron Stars as Propellers and Accretors with Conventional Magnetic Fields," *ApJ*, vol. 554, pp. 1245–1254, June 2001.

[135] I. Negueruela, G. L. Israel, A. Marco, A. J. Norton, and R. Speziali, "The Be/X-ray transient <ASTROBJ>KS 1947+300</ASTROBJ>," *Astronomy and Astrophysics*, vol. 397, pp. 739–745, Jan. 2003.

[136] D. K. Galloway, Z. Wang, and E. H. Morgan, "Discovery of Pulsations in the X-Ray Transient 4U 1901+03," *ApJ*, vol. 635, pp. 1217–1223, Dec. 2005.

[137] R. L. Kelley, S. Rappaport, and S. Ayasli, "Discovery of 9.3 S X-ray pulsations from 2S 1553-542 and a determination of the orbit," *ApJ*, vol. 274, pp. 765–770, Nov. 1983.

[138] M. Kuehnel, M. H. Finger, F. Fuerst, K. Pottschmidt, F. Haberl, and J. Wilms, "Orbital parameters and spin evolution of RX J0520.5-6932," *The Astronomer's Telegram*, vol. 5856, Feb. 2014.

[139] M. M. Serim, Ş. Şahiner, D. ćerri-Serim, S. ć. Inam, and A. Baykal, "Discovery of a glitch in the accretion-powered pulsar SXP 1062," *MNRAS*, vol. 471, pp. 4982–4989, Nov. 2017.

[140] V. Hénault-Brunet, L. M. Oskinova, M. A. Guerrero, W. Sun, Y.-H. Chu, C. J. Evans, J. S. Gallagher, III, R. A. Gruendl, and J. Reyes-Iturbide, "Discovery of a Be/X-ray pulsar binary and associated supernova remnant in the Wing of the Small Magellanic Cloud," *MNRAS*, vol. 420, pp. L13–L17, Feb. 2012.

[141] F. Haberl, R. Sturm, M. D. Filipović, W. Pietsch, and E. J. Crawford, "SXP 1062, a young Be X-ray binary pulsar with long spin period. Implications for the neutron star birth spin," *Astronomy and Astrophysics*, vol. 537, p. L1, Jan. 2012.

[142] R. Sturm, F. Haberl, L. M. Oskinova, M. P. E. Schurch, V. Hénault-Brunet, J. S. Gallagher, and A. Udalski, "Long-term evolution of the neutron-star spin period of SXP 1062," *Astronomy and Astrophysics*, vol. 556, p. A139, Aug. 2013.

[143] A. Udalski, "XROM and RCOM: Two New OGLE-III Real Time Data Analysis Systems," *Acta Astronomica*, vol. 58, pp. 187–192, Sept. 2008.

[144] P. C. Schmidtke, A. P. Cowley, and A. Udalski, "The Probable Orbital Period of SXP1062 (CXO J012745.97-733256.5)," *The Astronomer's Telegram*, vol. 4596, Nov. 2012.

[145] L. M. Oskinova, M. A. Guerrero, V. Hénault-Brunet, W. Sun, Y.-H. Chu, C. Evans, J. S. Gallagher, R. A. Gruendl, and J. Reyes-Iturbide, "The slow X-ray pulsar SXP 1062 and associated supernova remnant in the Wing of the Small Magellanic Cloud," in *Neutron Stars and Pulsars: Challenges and Opportunities after 80 years* (J. van Leeuwen, ed.), vol. 291 of *IAU Symposium*, pp. 459–461, Mar. 2013.

[146] S. B. Popov and R. Turolla, "Probing the neutron star spin evolution in the young Small Magellanic Cloud Be/X-ray binary SXP 1062," *MNRAS*, vol. 421, pp. L127–L131, Mar. 2012.

[147] N. R. Ikhsanov, "Signs of magnetic accretion in the young Be/X-ray pulsar SXP 1062," *MNRAS*, vol. 424, pp. L39–L43, July 2012.

[148] L. Fu and X.-D. Li, "Could SXP 1062 be an Accreting Magnetar?," *ApJ*, vol. 757, p. 171, Oct. 2012.

[149] K. A. Postnov, N. I. Shakura, A. Y. Kochetkova, and L. Hjalmarsdotter, "Do we see accreting magnetars in X-ray pulsars?," in *European Physical Journal Web of Conferences*, vol. 64 of *European Physical Journal Web of Conferences*, p. 02002, Jan. 2014.

[150] N. I. Shakura, K. A. Postnov, A. Y. Kochetkova, and L. Hjalmarsdotter, "Quasispherical subsonic accretion in X-ray pulsars," *Physics Uspekhi*, vol. 56, pp. 321–346, Apr. 2013.

[151] W. Cash, "Parameter estimation in astronomy through application of the likelihood ratio," *ApJ*, vol. 228, pp. 939–947, Mar. 1979.

[152] R. W. Hilditch, I. D. Howarth, and T. J. Harries, "Forty eclipsing binaries in the Small Magellanic Cloud: fundamental parameters and Cloud distance," *MNRAS*, vol. 357, pp. 304–324, Feb. 2005.

[153] L. Strüder, U. Briel, K. Dennerl, and et. al., "The European Photon Imaging Camera on XMM-Newton: The pn-CCD camera," *Astronomy and Astrophysics*, vol. 365, pp. L18–L26, Jan. 2001.

[154] G. P. Garmire, M. W. Bautz, P. G. Ford, J. A. Nousek, and G. R. Ricker, Jr., "Advanced CCD imaging spectrometer (ACIS) instrument on the Chandra X-ray Observatory," in *X-Ray and Gamma-Ray Telescopes and Instruments for Astronomy.* (J. E. Truemper and H. D. Tananbaum, eds.), vol. 4851 of *Proceedings of SPIE*, pp. 28–44, Mar. 2003.

[155] A. Fruscione, J. C. McDowell, G. E. Allen, N. S. Brickhouse, D. J. Burke, J. E. Davis, N. Durham, M. Elvis, E. C. Galle, D. E. Harris, D. P. Huenemoerder, J. C. Houck, B. Ishibashi, M. Karovska, F. Nicastro, M. S. Noble, M. A. Nowak, F. A. Primini, A. Siemiginowska, R. K. Smith, and M. Wise, "CIAO: Chandra's data analysis system," in *Society of Photo-Optical Instru-*

mentation Engineers (SPIE) Conference Series, vol. 6270 of *Proceedings of SPIE*, p. 62701V, June 2006.

[156] B. Içdem, A. Baykal, and S. Ç. Inam, "RXTE timing analysis of the anomalous X-ray pulsar 1E 2259+586," *MNRAS*, vol. 419, pp. 3109–3114, Feb. 2012.

[157] A. Baykal, M. J. Stark, and J. Swank, "Discovery of the Orbit of the Transient X-Ray Pulsar SAX J2103.5+4545," *ApJL*, vol. 544, pp. L129–L132, Dec. 2000.

[158] J. J. M. in't Zand, R. H. D. Corbet, and F. E. Marshall, "Discovery of a 75 Day Orbit in XTE J1543-568," *ApJL*, vol. 553, pp. L165–L168, June 2001.

[159] A. Baykal, E. Göğüş, S. Çağdaş İnam, and T. Belloni, "The Orbital Period of Swift J1626.6-5156," *ApJ*, vol. 711, pp. 1306–1309, Mar. 2010.

[160] M. Lampton, B. Margon, and S. Bowyer, "Parameter estimation in X-ray astronomy," *ApJ*, vol. 208, pp. 177–190, Aug. 1976.

[161] P. Reig and P. Roche, "Discovery of two new persistent Be/X-ray pulsar systems," *MNRAS*, vol. 306, pp. 100–106, June 1999.

[162] C. Knigge, M. J. Coe, and P. Podsiadlowski, "Two populations of X-ray pulsars produced by two types of supernova," *Nature*, vol. 479, pp. 372–375, Nov. 2011.

[163] J. Yang, S. G. T. Laycock, D. M. Christodoulou, S. Fingerman, M. J. Coe, and J. J. Drake, "A Comprehensive Library of X-Ray Pulsars in the Small Magellanic Cloud: Time Evolution of Their Luminosities and Spin Periods," *ApJ*, vol. 839, p. 119, Apr. 2017.

[164] Y.-M. Wang, "Disc accretion by magnetized neutron stars - A reassessment of the torque," *Astronomy and Astrophysics*, vol. 183, pp. 257–264, Sept. 1987.

[165] P. Ghosh, "Spin Evolution of Neutron Stars in Accretion Powered Pulsars," in *The Evolution of X-ray Binariese* (S. Holt and C. S. Day, eds.), vol. 308 of *American Institute of Physics Conference Series*, p. 439, Jan. 1994.

[166] U. Torkelsson, "Magnetic torques between accretion discs and stars," *MNRAS*, vol. 298, pp. L55–L59, Aug. 1998.

[167] P. Reig, J. M. Torrejón, and P. Blay, "Accreting magnetars: a new type of high-mass X-ray binaries?," *MNRAS*, vol. 425, pp. 595–604, Sept. 2012.

[168] D. Lynden-Bell and J. E. Pringle, "The evolution of viscous discs and the origin of the nebular variables.," *MNRAS*, vol. 168, pp. 603–637, Sept. 1974.

[169] V. M. Lipunov, "The magnetic fields of X-ray pulsars," *Soviet Astronomy*, vol. 26, pp. 537–541, Oct. 1982.

[170] G. S. Bisnovatyi-Kogan, "Rotational equilibrium of long-periodic X-ray pulsars," *Astronomy and Astrophysics*, vol. 245, pp. 528–530, May 1991.

[171] A. F. Illarionov and D. A. Kompaneets, "A Spin-Down Mechanism for Accreting Neutron Stars," *MNRAS*, vol. 247, p. 219, Nov. 1990.

[172] B. Haskell and A. Melatos, "Models of pulsar glitches," *International Journal of Modern Physics D*, vol. 24, p. 1530008, Jan. 2015.

[173] C. M. Espinoza, A. G. Lyne, B. W. Stappers, and M. Kramer, "A study of 315 glitches in the rotation of 102 pulsars," *MNRAS*, vol. 414, pp. 1679–1704, June 2011.

[174] M. Yu, R. N. Manchester, G. Hobbs, S. Johnston, V. M. Kaspi, M. Keith, A. G. Lyne, G. J. Qiao, V. Ravi, J. M. Sarkissian, R. Shannon, and R. X. Xu, "Detection of 107 glitches in 36 southern pulsars," *MNRAS*, vol. 429, pp. 688–724, Feb. 2013.

[175] R. Dib and V. M. Kaspi, "16 yr of RXTE Monitoring of Five Anomalous X-Ray Pulsars," *ApJ*, vol. 784, p. 37, Mar. 2014.

[176] F. K. Lamb, D. Pines, and J. Shaham, "Period variations in pulsating X-ray sources. I - Accretion flow parameters and neutron star structure from timing observations," *ApJ*, vol. 224, pp. 969–987, Sept. 1978.

[177] F. K. Lamb, D. Pines, and J. Shaham, "Period variations in pulsating X-ray sources. II - Torque variations and stellar response," *ApJ*, vol. 225, pp. 582–590, Oct. 1978.

[178] J. Sauls, "Superfluidity in the interiors of neutron stars," in *NATO Advanced Science Institutes (ASI) Series C* (H. Ögelman and E. P. J. van den Heuvel,

eds.), vol. 262 of *NATO Advanced Science Institutes (ASI) Series C*, p. 457, 1989.

[179] F. K. Lamb, "Neutron stars and black holes," in *Frontiers of Stellar Evolution* (D. L. Lambert, ed.), vol. 20 of *Astronomical Society of the Pacific Conference Series*, pp. 299–388, 1991.

[180] B. Datta and M. A. Alpar, "Implications of the Crustal Moment of Inertia for Neutron Star Equations of State," *Astronomy and Astrophysics*, vol. 275, p. 210, Aug. 1993.

[181] J. M. Lattimer and M. Prakash, "Neutron star observations: Prognosis for equation of state constraints," *Physics Reports*, vol. 442, pp. 109–165, Apr. 2007.

[182] M. A. Alpar, P. W. Anderson, D. Pines, and J. Shaham, "Giant glitches and pinned vorticity in the VELA and other pulsars," *ApJL*, vol. 249, pp. L29–L33, Oct. 1981.

[183] O. Akbal, E. Gügercinoğlu, S. Şaşmaz Muş, and M. A. Alpar, "Peculiar glitch of PSR J1119-6127 and extension of the vortex creep model," *MNRAS*, vol. 449, pp. 933–941, May 2015.

[184] M. A. Livingstone, V. M. Kaspi, and F. P. Gavriil, "Timing Behavior of the Magnetically Active Rotation-Powered Pulsar in the Supernova Remnant Kesteven 75," *ApJ*, vol. 710, pp. 1710–1717, Feb. 2010.

[185] R. N. Manchester and G. Hobbs, "A Giant Glitch in PSR J1718-3718," *ApJL*, vol. 736, p. L31, Aug. 2011.

[186] R. F. Archibald, V. M. Kaspi, S. P. Tendulkar, and P. Scholz, "A Magnetar-like Outburst from a High-B Radio Pulsar," *ApJL*, vol. 829, p. L21, Sept. 2016.

[187] R. F. Archibald, V. M. Kaspi, C.-Y. Ng, K. N. Gourgouliatos, D. Tsang, P. Scholz, A. P. Beardmore, N. Gehrels, and J. A. Kennea, "An anti-glitch in a magnetar," *Nature*, vol. 497, pp. 591–593, May 2013.

[188] P. M. Woods, C. Kouveliotou, J. van Paradijs, M. H. Finger, C. Thompson, R. C. Duncan, K. Hurley, T. Strohmayer, J. Swank, and T. Murakami, "Variable

Spin-Down in the Soft Gamma Repeater SGR 1900+14 and Correlations with Burst Activity," *ApJL*, vol. 524, pp. L55–L58, Oct. 1999.

[189] C. Thompson, R. C. Duncan, P. M. Woods, C. Kouveliotou, M. H. Finger, and J. van Paradijs, "Physical Mechanisms for the Variable Spin-down and Light Curve of SGR 1900+14," *ApJ*, vol. 543, pp. 340–350, Nov. 2000.

[190] S. Şaşmaz Muş and E. Göğüş, "Long-term Timing and Glitch Characteristics of Anomalous X-Ray Pulsar 1RXS J170849.0-400910," *ApJ*, vol. 778, p. 156, Dec. 2013.

[191] R. F. Archibald, V. M. Kaspi, P. Scholz, A. P. Beardmore, N. Gehrels, and J. A. Kennea, "SWIFT Observations of Two Outbursts from the Magnetar 4U0142+61," *ApJ*, vol. 834, p. 163, Jan. 2017.

[192] R. C. Duncan, "Astrophysics: A glimpse inside a magnetar," *Nature*, vol. 497, pp. 574–576, May 2013.

[193] E. Gügercinoğlu and M. A. Alpar, "Vortex Creep Against Toroidal Flux Lines, Crustal Entrainment, and Pulsar Glitches," *ApJL*, vol. 788, p. L11, June 2014.

[194] A. Baykal, "The torque and X-ray flux changes of OAO 1657-415.," *Astronomy and Astrophysics*, vol. 319, pp. 515–524, Mar. 1997.

[195] D. K. Galloway, E. H. Morgan, and A. M. Levine, "A Frequency Glitch in an Accreting Pulsar," *ApJ*, vol. 613, pp. 1164–1172, Oct. 2004.

[196] L. Ducci, P. M. Pizzochero, V. Doroshenko, A. Santangelo, S. Mereghetti, and C. Ferrigno, "Properties and observability of glitches and anti-glitches in accreting pulsars," *Astronomy and Astrophysics*, vol. 578, p. A52, June 2015.

[197] A. Baykal, A. Alpar, and U. Kiziloglu, "A shot noise model for a two-component neutron star," *Astronomy and Astrophysics*, vol. 252, pp. 664–668, Dec. 1991.

[198] P. M. Pizzochero, "Angular Momentum Transfer in Vela-like Pulsar Glitches," *ApJL*, vol. 743, p. L20, Dec. 2011.

[199] G. Baym, C. Pethick, and D. Pines, "Superfluidity in Neutron Stars," *Nature*, vol. 224, pp. 673–674, Nov. 1969.

[200] M. A. Alpar, S. A. Langer, and J. A. Sauls, "Rapid postglitch spin-up of the superfluid core in pulsars," *ApJ*, vol. 282, pp. 533–541, July 1984.

[201] M. A. Alpar and J. A. Sauls, "On the dynamical coupling between the superfluid interior and the crust of a neutron star," *ApJ*, vol. 327, pp. 723–725, Apr. 1988.

[202] T. Sidery and M. A. Alpar, "The effect of quantized magnetic flux lines on the dynamics of superfluid neutron star cores," *MNRAS*, vol. 400, pp. 1859–1867, Dec. 2009.

[203] M. A. Alpar, D. Pines, P. W. Anderson, and J. Shaham, "Vortex creep and the internal temperature of neutron stars. I - General theory," *ApJ*, vol. 276, pp. 325–334, Jan. 1984.

[204] T. Delsate, N. Chamel, N. Gürlebeck, A. F. Fantina, J. M. Pearson, and C. Ducoin, "Giant pulsar glitches and the inertia of neutron star crusts," *Physical Review D*, vol. 94, p. 023008, July 2016.

[205] W. G. Newton, S. Berger, and B. Haskell, "Observational constraints on neutron star crust-core coupling during glitches," *MNRAS*, vol. 454, pp. 4400–4410, Dec. 2015.

[206] M. M. Serim, Ş. Şahiner, D. Çerri-Serim, S. Ç. İnam, and A. Baykal, "Comprehensive timing and X-ray spectral analysis of GX 1+4," *MNRAS*, vol. 469, pp. 2509–2516, Aug. 2017.

[207] W. H. G. Lewin, G. R. Ricker, and J. E. McClintock, "X-Rays from a New Variable Source GX 1+4," *ApJL*, vol. 169, p. L17, Oct. 1971.

[208] N. E. White, J. H. Swank, and S. S. Holt, "Accretion powered X-ray pulsars," *ApJ*, vol. 270, pp. 711–734, July 1983.

[209] K. Makishima, T. Ohashi, T. Sakao, T. Dotani, H. Inoue, K. Koyama, F. Makino, K. Mitsuda, F. Nagase, H. D. Thomas, M. J. L. Turner, T. Kii, and Y. Tawara, "Spin-down of the X-ray pulsar GX1 +4 during an extended low state," *Nature*, vol. 333, pp. 746–748, June 1988.

[210] I. S. Glass and M. W. Feast, "Peculiar Object near X2+5," *Nature Physical Science*, vol. 245, pp. 39–40, Sept. 1973.

[211] D. Chakrabarty and P. Roche, "The Symbiotic Neutron Star Binary GX 1+4/V2116 Ophiuchi," *ApJ*, vol. 489, pp. 254–271, Nov. 1997.

[212] K. H. Hinkle, F. C. Fekel, R. R. Joyce, P. R. Wood, V. V. Smith, and T. Lebzelter, "Infrared Spectroscopy of Symbiotic Stars. IV. V2116 Ophiuchi/GX 1+4, The Neutron Star Symbiotic," *ApJ*, vol. 641, pp. 479–487, Apr. 2006.

[213] R. H. D. Corbet, J. L. Sokoloski, K. Mukai, C. B. Markwardt, and J. Tueller, "A Comparison of the Variability of the Symbiotic X-Ray Binaries GX 1+4, 4U 1954+31, and 4U 1700+24 from Swift BAT and RXTE ASM Observations," *ApJ*, vol. 675, pp. 1424–1435, Mar. 2008.

[214] T. Dotani, T. Kii, F. Nagase, K. Makishima, T. Ohashi, T. Sakao, K. Koyama, and I. R. Tuohy, "Peculiar pulse profile of GX 1+4 observed in the spin-down phase," *Astronomical Society of Japan, Publications*, vol. 41, pp. 427–440, 1989.

[215] W. Cui and B. Smith, "Cessation of X-Ray Pulsation of GX 1+4," *ApJ*, vol. 602, pp. 320–326, Feb. 2004.

[216] N. Rea, L. Stella, G. L. Israel, G. Matt, S. Zane, A. Segreto, T. Oosterbroek, and M. Orlandini, "A Compton reflection dominated spectrum in a peculiar accreting neutron star," *MNRAS*, vol. 364, pp. 1229–1238, Dec. 2005.

[217] C. Ferrigno, A. Segreto, A. Santangelo, J. Wilms, I. Kreykenbohm, M. Denis, and R. Staubert, "INTEGRAL observation of the accreting pulsar GX 1+4," *Astronomy and Astrophysics*, vol. 462, pp. 995–1005, Feb. 2007.

[218] E. P. Cutler, B. R. Dennis, and J. F. Dolan, "An elliptical binary orbit model of GX 1 + 4," *ApJ*, vol. 300, pp. 551–556, Jan. 1986.

[219] M. G. Pereira, J. Braga, and F. Jablonski, "The Orbital Period of the Accreting Pulsar GX 1+4," *ApJL*, vol. 526, pp. L105–L109, Dec. 1999.

[220] J. Braga, M. G. Pereira, and F. J. Jablonski, "Evidence for a 304-day orbital period for GX 1+4," in *American Institute of Physics Conference Series* (M. L.

McConnell and J. M. Ryan, eds.), vol. 510 of *American Institute of Physics Conference Series*, pp. 188–192, Apr. 2000.

[221] K. Iłkiewicz, J. Mikołajewska, and B. Monard, "Variability of the symbiotic X-ray binary GX 1+4. Enhanced activity near periastron passage," *Astronomy and Astrophysics*, vol. 601, p. A105, May 2017.

[222] D. Chakrabarty, L. Bildsten, M. H. Finger, J. M. Grunsfeld, D. T. Koh, R. W. Nelson, T. A. Prince, B. A. Vaughan, and R. B. Wilson, "On the Correlation of Torque and Luminosity in GX 1+4," *ApJL*, vol. 481, pp. L101–L105, June 1997.

[223] A. Baykal and H. Oegelman, "An empirical torque noise and spin-up model for accretion-powered X-ray pulsars," *Astronomy and Astrophysics*, vol. 267, pp. 119–125, Jan. 1993.

[224] A. Baykal, Ç. Inam, M. Ali Alpar, J. in't Zand, and T. Strohmayer, "The steady spin-down rate of 4U 1907+09," *MNRAS*, vol. 327, pp. 1269–1272, Nov. 2001.

[225] A. Baykal, S. Ç. İnam, and E. Beklen, "Evidence of a change in the long-term spin-down rate of the X-ray pulsar 4U 1907+09," *MNRAS*, vol. 369, pp. 1760–1764, July 2006.

[226] Ş. Şahiner, S. Ç. Inam, and A. Baykal, "A comprehensive study of RXTE and INTEGRAL observations of the X-ray pulsar 4U 1907+09," *MNRAS*, vol. 421, pp. 2079–2087, Apr. 2012.

[227] A. Baykal, "Short-term pulse frequency fluctuations of OAO 1657-415 from RXTE observations," *MNRAS*, vol. 313, pp. 637–640, Apr. 2000.

[228] Z. Acuner, S. Ç. İnam, Ş. Şahiner, M. M. Serim, A. Baykal, and J. Swank, "Timing studies of X Persei and the discovery of its transient quasi-periodic oscillation feature," *MNRAS*, vol. 444, pp. 457–465, Oct. 2014.

[229] A. Baykal, S. Ç. Inam, M. J. Stark, C. M. Heffner, A. E. Erkoca, and J. H. Swank, "Timing studies on RXTE observations of SAX J2103.5+4545," *MNRAS*, vol. 374, pp. 1108–1114, Jan. 2007.

[230] M. Feroci, L. Stella, M. van der Klis, and et. al., "The Large Observatory for X-ray Timing (LOFT)," *Experimental Astronomy*, vol. 34, pp. 415–444, Oct. 2012.

[231] B. Paul, A. R. Rao, and K. P. Singh, "Torque-luminosity correlation and possible evidence for core-crust relaxation in the X-ray pulsar GX 1+4.," *Astronomy and Astrophysics*, vol. 320, pp. L9–L12, Apr. 1997.

[232] N. E. White, K. O. Mason, P. W. Sanford, and P. Murdin, "The X-ray behaviour of 3U 0352+30 (X Per)," *MNRAS*, vol. 176, pp. 201–215, July 1976.

[233] H. Delgado-Martí, A. M. Levine, E. Pfahl, and S. A. Rappaport, "The Orbit of X Persei and Its Neutron Star Companion," *ApJ*, vol. 546, pp. 455–468, Jan. 2001.

[234] F. Nagase, "Accretion-powered X-ray pulsars," *Astronomical Society of Japan, Publications*, vol. 41, pp. 1–79, 1989.

[235] A. A. Lutovinov, S. A. Grebenev, R. A. Syunyaev, and M. N. Pavlinskii, "Timing of x-ray pulsars from data obtained with the ART-P telescope of the GRANAT space observatory in 1990-1992," *Astronomy Letters*, vol. 20, pp. 538–564, Sept. 1994.

[236] F. Haberl, "ROSAT soft X-ray observations of the Be/X-ray binary X Persei," *Astronomy and Astrophysics*, vol. 283, pp. 175–178, Mar. 1994.

[237] N. R. Robba, L. Burderi, G. A. Wynn, R. S. Warwick, and T. Murakami, "A GINGA Observation of the X-Ray Pulsar 4U 0352+30," *ApJ*, vol. 472, p. 341, Nov. 1996.

[238] T. Di Salvo, L. Burderi, N. R. Robba, and M. Guainazzi, "The Two-Component X-Ray Broadband Spectrum of X Persei Observed by BeppoSAX," *ApJ*, vol. 509, pp. 897–903, Dec. 1998.

[239] A. Lutovinov, S. Tsygankov, and M. Chernyakova, "Strong outburst activity of the X-ray pulsar X Persei during 2001-2011," *MNRAS*, vol. 423, pp. 1978–1984, June 2012.

[240] K. Jahoda, C. B. Markwardt, Y. Radeva, A. H. Rots, M. J. Stark, J. H. Swank, T. E. Strohmayer, and W. Zhang, "Calibration of the Rossi X-Ray Timing Explorer Proportional Counter Array," *ApJS*, vol. 163, pp. 401–423, Apr. 2006.

[241] P. Ubertini, F. Lebrun, G. Di Cocco, A. Bazzano, A. J. Bird, K. Broenstad, A. Goldwurm, G. La Rosa, C. Labanti, P. Laurent, I. F. Mirabel, E. M. Quadrini, B. Ramsey, V. Reglero, L. Sabau, B. Sacco, R. Staubert, L. Vigroux, M. C. Weisskopf, and A. A. Zdziarski, "IBIS: The Imager on-board INTE-GRAL," *Astronomy and Astrophysics*, vol. 411, pp. L131–L139, Nov. 2003.

[242] J. E. Deeter and P. E. Boynton, "Techniques for the estimation of red power spectra. I - Context and methodology," *ApJ*, vol. 261, pp. 337–350, Oct. 1982.

[243] P. Esposito, G. L. Israel, L. Sidoli, E. Mason, G. A. Rodríguez Castillo, J. P. Halpern, A. Moretti, and D. Götz, "Discovery of 47-s pulsations in the X-ray source 1RXS J225352.8+624354," *MNRAS*, vol. 433, pp. 2028–2035, Aug. 2013.

[244] J. E. Deeter, *Pulse timing techniques and applications to X-ray pulsars*. PhD thesis, Washington Univ., Seattle., 1981.

[245] J. E. Deeter, P. E. Boynton, F. K. Lamb, and G. Zylstra, "VELA X-1 pulse timing. II - Variations in pulse frequency," *ApJ*, vol. 336, pp. 376–393, Jan. 1989.

CURRICULUM VITAE

PERSONAL INFORMATION

Surname, Name: Serim, Muhammed Miraç
Nationality: Turkish (TC)
Date and Place of Birth: 30.09.1987, Ankara
Marital Status: Married
Phone: 0 312 210 43 19
Fax: 0 312 210 50 99
e-mail: muhammed@astroa.physics.metu.edu.tr

EDUCATION

Degree	Institution	Place	Grad. Date
Ph.D.	Department of Physics, METU	Ankara	January 2019
M.S.	Department of Physics, METU	Ankara	September 2012
B.S.	Department of Physics, METU	Ankara	June 2009

PROFESSIONAL EXPERIENCE

Year	Place	Enrollment
2011-2018	METU Physics	Research Assistant
2015-2018	METU Physics	Pre-Doctoral Fellow TUBİTAK: 114F345
2011-2012	METU Physics	Pre-Doctoral Fellow TUBİTAK: 109T748

PUBLICATIONS

1) *Discovery of a Glitch in the Accretion Powered Pulsar SXP 1062*
    Serim M. M., Şahiner Ş., Çerri-Serim D., İnam S. Ç., Baykal A., Vol 471, MNRAS, (2017)

2) *Comprehensive Timing and X-ray Spectral Analysis of GX 1+4*
    Serim M. M., Şahiner Ş., Çerri-Serim D., İnam S. Ç., Baykal A., Vol 469, MNRAS, (2017)

3) *RXTE & SWIFT Observations of SWIFT J0513.4-6547*
    Şahiner Ş., Serim M. M., Inam S. Ç., Baykal A., Vol 456, MNRAS (2016)

4) *Timing Studies of X Persei and the Discovery of Its Transient Quasi-Periodic Oscillation Feature*
    Acuner Z., İnam S. Ç., Şahiner Ş., Serim M. M., Baykal A., Swank J., Vol 444, MNRAS (2014)

5) *RXTE & SWIFT Observations of SWIFT J1729.0-3437*
    Şahiner Ş., İnam S. Ç., Serim M. M., Baykal A., Vol 434, MNRAS (2013)

International Conference Publications

1) *The Timing Noise of Magnetars*
    Çerri-Serim D., Serim M. M., Yucalan D., Şahiner Ş., İnam S. Ç., Baykal A., *Proc. of Science, 2017*

2) *Episodic Torque-Luminosity Correlations and Anti-correlations of GX 1+4*
    Serim M. M., Şahiner Ş., Çerri-Serim D., İnam S. Ç., Baykal A., *Proc. of Science, 2017*

3) *Noise Strength Estimates of Three SGRs:Swift J1822.3-1606, SGR J1833-0832 and Swift J1834.9-0846*
    Serim M. M., İnam S. Ç. , Baykal A., *Astronomical Society of the Pacific Conference Series 2012*

Others

1) *SGR J1822-1606: Constant Spin Period*
    Serim M. M., Baykal A., İnam S. Ç., *Astronomers Telegram 3543*

2) *A Re-analysis of Timing Parameters of SGR J1833-0832*
    Balman Ş., Baykal A., Serim M. M., *Astronomers Telegram 2763*